



Title	Effective spin model in momentum space : Toward a systematic understanding of multiple-Q instability by momentum-resolved anisotropic exchange interactions
Author(s)	Yambe, Ryota; Hayami, Satoru
Citation	Physical Review B, 106(17), 174437 https://doi.org/10.1103/PhysRevB.106.174437
Issue Date	2022-11-30
Doc URL	http://hdl.handle.net/2115/88845
Rights	©2023 American Physical Society
Type	article
File Information	PhysRevB.106.174437.pdf



[Instructions for use](#)

Effective spin model in momentum space: Toward a systematic understanding of multiple- Q instability by momentum-resolved anisotropic exchange interactions

Ryota Yambe^{1,*} and Satoru Hayami^{1,2,†}

¹*Department of Applied Physics, The University of Tokyo, Tokyo 113-8656, Japan*

²*Graduate School of Science, Hokkaido University, Sapporo 060-0810, Japan*



(Received 20 February 2022; revised 30 September 2022; accepted 7 November 2022; published 30 November 2022)

Multiple- Q magnetic states, such as a skyrmion crystal, become a source of unusual transport phenomena and dynamics. Recent theoretical and experimental studies clarified that such multiple- Q states ubiquitously appear under different crystal structures in metals and insulators. Toward a systematic understanding of the formation of the multiple- Q states in various crystal systems, in this theoretical study we present a low-energy effective spin model with anisotropic exchange interactions in momentum space. We summarize symmetry rules for nonzero symmetric and antisymmetric anisotropic exchange interactions in momentum space, which are regarded as an extension of Moriya's rule. According to the rules, we construct the effective spin model for tetragonal, hexagonal, and trigonal magnets with primitive-lattice and multisublattice structures based on the symmetry of the crystal and wave vector. Furthermore, we describe the microscopic origin of the effective anisotropic exchange interactions in itinerant magnets by perturbatively analyzing a multiband periodic Anderson model with the spin-orbit coupling. We apply the effective spin model to an itinerant magnet in a $P6/mmm$ crystal, and we find various multiple- Q states with a spin scalar chirality in the ground state. Our results provide a foundation of constructing effective phenomenological spin models for any crystal systems hosting the multiple- Q states, which will stimulate further exploration of exotic multiple- Q states in materials with the spin-orbit coupling.

DOI: [10.1103/PhysRevB.106.174437](https://doi.org/10.1103/PhysRevB.106.174437)

I. INTRODUCTION

Topological spin textures have attracted much attention as a source of unconventional physical phenomena and a candidate for robust information carriers against external stimuli [1–5]. Since the first discovery of a magnetic skyrmion [6–9] in a chiral magnet MnSi [10], active searches have revealed its existence in a variety of crystal systems irrespective of spatial inversion symmetry [11]: cubic [10,12], hexagonal [13–15], and tetragonal [16–19] crystal systems. The skyrmion spin structure is characterized by an integer topological number (skyrmion number), which gives rise to intriguing transport phenomena, such as the topological Hall and Nernst effects [14,20–25]. In addition, a variety of new topological spin textures beyond the skyrmions have also been extensively investigated [5], some of which have been observed in experiments, such as a hedgehog [26–28], biskyrmion [29,30], skyrmionium [31], ferrimagnetic skyrmion [32], and antiferromagnetic skyrmion [33].

In the crystal systems, such topological spin textures often appear in a periodic form, which are expressed as a superposition of multiple spin density waves termed a multiple- Q state [34–39]. The multiple- Q spin configuration consisting of n -tuple spin density waves with the ordering wave vectors

$\{\mathbf{Q}_1, \mathbf{Q}_2, \dots, \mathbf{Q}_n\}$ is given by

$$\mathbf{S}_i = \sum_{v=1}^n (e^{i\mathbf{Q}_v \cdot \mathbf{R}_i} \mathbf{S}_{\mathbf{Q}_v} + e^{-i\mathbf{Q}_v \cdot \mathbf{R}_i} \mathbf{S}_{-\mathbf{Q}_v}), \quad (1)$$

where \mathbf{S}_q is the Fourier transform of the spin at the wave vector \mathbf{q} . A variety of multiple- Q magnetic structures are realized depending on the type of constituent waves characterized by $\mathbf{S}_{\mathbf{Q}_v}$. For example, a triple- Q superposition of proper-screw (cycloidal) spiral waves leads to a Bloch-type (Néel-type) skyrmion crystal (SkX) with a skyrmion number of ± 1 , while that of the sinusoidal waves induces different types of the SkX with a skyrmion number of ± 2 . The multiple- Q spin configuration in Eq. (1) can describe other periodic topological spin textures, such as a hedgehog lattice [40–46], meron-antimeron crystal [47–55], and vortex crystal [56–62]. Furthermore, the sublattice-dependent multiple- Q states [63–67], such as the antiferromagnetic SkX, are described by taking into account the sublattice degrees of freedom in Eq. (1).

The emergence of multiple- Q states largely depends on the microscopic mechanisms, which have been extensively studied for various systems. The typical mechanisms are dipolar interactions [53,68,69], competing exchange interactions in frustrated magnets [45,66,70–72], a biquadratic spin interaction in itinerant magnets [73–77], and symmetric and antisymmetric magnetic anisotropy in systems with the spin-orbit coupling (SOC) [9,49,52,78–89].

In this paper, we focus on the role of symmetric and antisymmetric anisotropic exchange interactions originating from the SOC and dipolar interactions. The Dzyaloshinskii-Moriya

*yambe@g.ecc.u-tokyo.ac.jp

†hayami@phys.sci.hokudai.ac.jp

(DM) interaction is the most familiar anisotropic exchange interaction arising in noncentrosymmetric materials [90,91]. It favors the spiral spin density wave with a spiral plane perpendicular to the DM vector in the combination of the ferromagnetic exchange interaction, which results in multiple- Q spiral states in an external magnetic field [9,41]. As the DM vector is determined by crystal symmetry, which is the so-called Moriya's rule [91], one can expect the types of multiple- Q states that appear in the DM-based systems [7]. For example, the DM interaction in $P422$, $P4mm$, and $P\bar{4}m2$ crystals tends to favor the Bloch-type, Néel-type, and antitype SkXs, respectively.

In contrast to the early studies based on the antisymmetric DM interaction, recent discoveries of SkXs and hedgehog lattices in centrosymmetric magnets [14,15,18,28] open up the possibility that various multiple- Q states can emerge by symmetric anisotropic exchange interactions. In fact, some model calculations have clarified that such a symmetric anisotropic exchange interaction stabilizes the multiple- Q states including the SkXs in centrosymmetric crystals with the space group $P4/mmm$ [51–53,92,93], $P6/mmm$ [54,69,94–96], and $P\bar{3}m1$ [61,89,97]. However, there have been few studies focusing on the symmetric anisotropic exchange interactions in spite of various types of interactions depending on the crystal symmetry classified by the space group. To understand which types of anisotropic exchange interactions play an important role in inducing the multiple- Q states, it is highly desired to perform a systematic investigation for various space groups irrespective of the centrosymmetric and noncentrosymmetric lattice structures. Furthermore, it is important to clarify relevant microscopic model parameters for the emergence of the anisotropic exchange interactions beyond the symmetry argument.

To systematically investigate the multiple- Q instability induced by the anisotropic exchange interactions, we present how to construct an effective spin model in discrete lattice systems based on the magnetic representation [98] and perturbation analyses [73,77,99]. Our effective spin model can be applied to magnetic systems with both a short-range exchange interaction in insulators and a long-range one in metals irrespective of classical and quantum spins. Furthermore, our effective spin model can be used irrespective of whether the anisotropic form of the interaction originates from the SOC or dipolar interaction. First, we find general symmetry rules to specify both symmetric and antisymmetric exchange interactions in momentum space, which is an extension of Moriya's rule. The obtained rules provide a foundation of constructing the effective low-energy spin model with the momentum-resolved anisotropic exchange interactions based on the symmetry of the crystal and the wave vector, which are closely related to neutron and x-ray experiments. As an example, we demonstrate how to construct the effective spin model in tetragonal, hexagonal, and trigonal crystal systems by applying the rules to 24 space groups with primitive lattices. In addition, we show an extension of the symmetry rules to multisublattice systems, and we test our rules on the honeycomb and kagome systems as examples. Next, we show one of the microscopic origins of the long-range anisotropic exchange interactions by starting from the periodic Anderson model (PAM) incorporating the effect of the

SOC [61,100,101]. We present important microscopic model parameters for the anisotropic exchange interactions based on the perturbation analysis. The perturbation analysis beyond the symmetry argument gives us a way to quantitatively evaluate the anisotropic exchange interactions. Finally, we demonstrate that the anisotropic exchange interactions stabilize various multiple- Q states with a spin scalar chirality by considering a specific example in a $P6/mmm$ crystal and by performing simulated annealing for the effective spin model. The present results to construct the effective spin model with momentum-resolved interactions provide both symmetric and microscopic ways of investigating a plethora of multiple- Q instabilities in various crystal systems. In particular, the present effective spin model is useful to identify complicated spin configurations including the SkX in materials, such as Gd_2PdSi_3 [14], $\text{Gd}_3\text{Ru}_4\text{Al}_{12}$ [15,96], GdRu_2Si_2 [18,102,103], EuPtSi [104–108], and EuAl_4 [109–112].

This paper is organized as follows. In Sec. II, we show a way to obtain the momentum-resolved anisotropic exchange interactions under the crystal symmetry based on the magnetic representation analysis. In Secs. III and IV, we discuss the origin of momentum-resolved anisotropic exchange interactions in itinerant electron models and localized spin models, respectively. In particular, we show the relationship between the long-range anisotropic exchange interaction and microscopic model parameters by performing the perturbation calculation in the PAM in Sec. III. In Sec. V, we show how to construct and analyze the effective spin model by taking an example of the system belonging to the $P6/mmm$ space group. We summarize the obtained results and discuss a perspective in Sec. VI.

II. SYMMETRY ANALYSIS OF ANISOTROPIC EXCHANGE INTERACTIONS

In this section, we show the classification of an anisotropic exchange interaction in momentum space in crystal systems based on the symmetry argument. In Secs. II A 1 and II A 2, we present general rules to give nonzero momentum-resolved anisotropic exchange interactions in primitive-lattice systems and multisublattice systems, respectively. Then, we explicitly show the effective spin model in tetragonal, hexagonal, and trigonal crystal systems with the primitive lattice in Sec. II B 1. In addition, we show the effective spin model on the honeycomb (kagome) structure as an example of two-sublattice (three-sublattice) systems in Sec. II B 2. We also discuss a tendency of single- Q and multiple- Q modulations in the presence of the anisotropic exchange interactions in Sec. II C.

A. General symmetry rules

1. Primitive-lattice case

Let us start by considering a general form of the momentum-resolved exchange interaction with wave vector \mathbf{q} . We consider an arbitrary bilinear exchange coupling, which is given by

$$S_{\mathbf{q}}^T X_{\mathbf{q}} S_{-\mathbf{q}}, \quad (2)$$

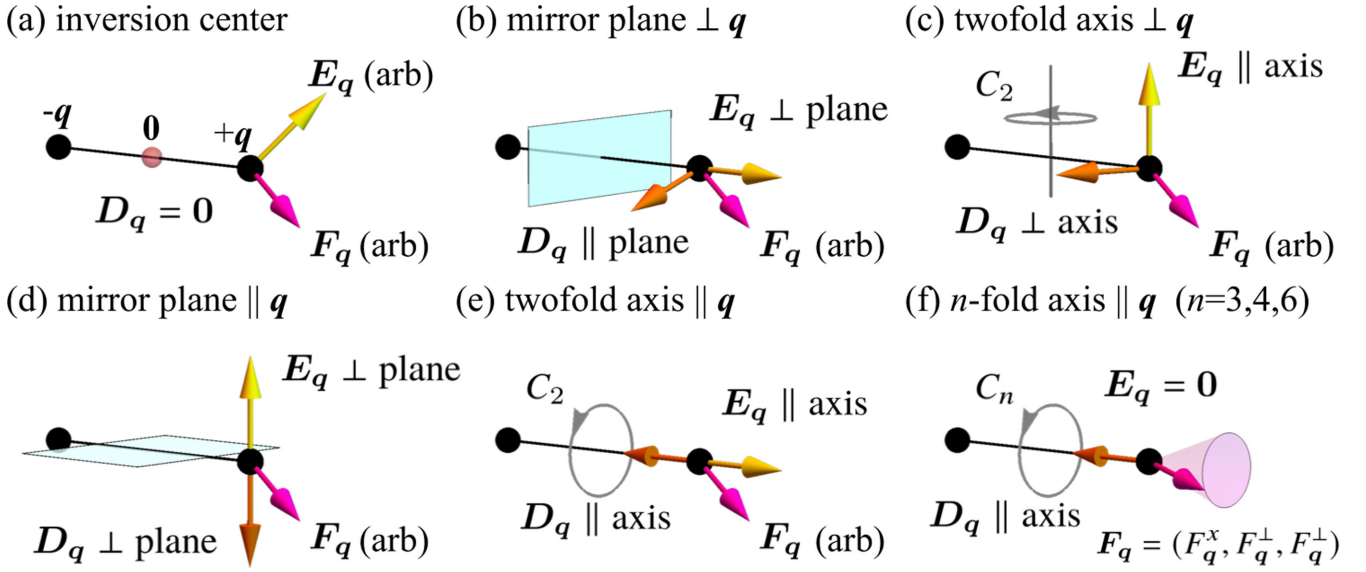


FIG. 1. Symmetry operations for wave vectors \mathbf{q} and $-\mathbf{q}$ in momentum space: (a) space inversion at the inversion center denoted as $\mathbf{0}$, (b) mirror perpendicular to \mathbf{q} , (c) twofold rotation perpendicular to \mathbf{q} , (d) mirror parallel to \mathbf{q} , (e) twofold rotation around \mathbf{q} , and (f) n -fold ($n = 3, 4, 6$) rotation around \mathbf{q} . The nonzero components of \mathbf{D}_q , \mathbf{E}_q , and \mathbf{F}_q are represented by the orange, yellow, and magenta arrows, respectively. \mathbf{E}_q in (a) and \mathbf{F}_q in (a)–(e) are arbitrary (arb).

with

$$X_q = \begin{pmatrix} F_q^{x_s} & E_q^{z_s} + iD_q^{z_s} & E_q^{y_s} - iD_q^{y_s} \\ E_q^{z_s} - iD_q^{z_s} & F_q^{y_s} & E_q^{x_s} + iD_q^{x_s} \\ E_q^{y_s} + iD_q^{y_s} & E_q^{x_s} - iD_q^{x_s} & F_q^{z_s} \end{pmatrix}. \quad (3)$$

In Eq. (2), $\mathbf{S}_q^T = (S_q^{x_s}, S_q^{y_s}, S_q^{z_s})$ is the Fourier transform of the spin, (x_s, y_s, z_s) are Cartesian spin coordinates, and T denotes the transpose of the vector. It is noted that the following results in this section are applicable to both classical spin and quantum spin operators; the expectation value of the spin is not necessarily fully polarized. In addition, we ignore the sub-lattice structure in the lattice system in Eq. (2) for simplicity; we also discuss the counterpart to the multisublattice systems [see Eqs. (7) and (8)] in Sec. II A 2. In Eq. (3), X_q stands for the general form of the interaction matrix with the real coupling constants $\mathbf{D}_q = (D_q^{x_s}, D_q^{y_s}, D_q^{z_s})$, $\mathbf{E}_q = (E_q^{x_s}, E_q^{y_s}, E_q^{z_s})$, and $\mathbf{F}_q = (F_q^{x_s}, F_q^{y_s}, F_q^{z_s})$; \mathbf{D}_q corresponds to the antisymmetric interaction in spin space, while \mathbf{E}_q and \mathbf{F}_q correspond to the symmetric off-diagonal and diagonal ones, respectively. For instance, the x_s components of \mathbf{D}_q , \mathbf{E}_q , and \mathbf{F}_q are expressed as

$$iD_q^{x_s}(S_q^{y_s}S_{-q}^{z_s} - S_q^{z_s}S_{-q}^{y_s}), \quad (4)$$

$$E_q^{x_s}(S_q^{y_s}S_{-q}^{z_s} + S_q^{z_s}S_{-q}^{y_s}), \quad (5)$$

$$F_q^{x_s}(S_q^{x_s}S_{-q}^{x_s}). \quad (6)$$

The momentum-resolved interactions \mathbf{D}_q , \mathbf{E}_q , and \mathbf{F}_q show a different transformation by reversing $\mathbf{q} \rightarrow -\mathbf{q}$ due to the time-reversal symmetry; $\mathbf{D}_q = -\mathbf{D}_{-q}$, $\mathbf{E}_q = \mathbf{E}_{-q}$, and $\mathbf{F}_q = \mathbf{F}_{-q}$. The nonzero components in X_q depend on the crystal symmetry. It is noted that, in general, X_q depends on both temperature and microscopic model parameters as discussed in Sec. III, although they do not affect the following results

based on the symmetry analysis. We find six rules to determine nonzero \mathbf{q} -resolved anisotropic exchange interactions. In the following, we consider the wave vector \mathbf{q} , which lies inside the Brillouin zone for simplicity; \mathbf{q} does not lie on the Brillouin zone boundary. Then, the six rules for \mathbf{D}_q , \mathbf{E}_q , and \mathbf{F}_q under the specific crystal (point group) symmetry are given by using the magnetic representation theory:

(a) The space inversion symmetry imposes $\mathbf{D}_q = \mathbf{0}$, while there is no constraint on \mathbf{E}_q and \mathbf{F}_q [Fig. 1(a)].

(b) The mirror symmetry with respect to the plane perpendicular to \mathbf{q} imposes $\mathbf{D}_q \parallel \text{plane}$ and $\mathbf{E}_q \perp \text{plane}$, while there is no constraint on \mathbf{F}_q [Fig. 1(b)].

(c) The twofold rotational symmetry around the axis perpendicular to \mathbf{q} imposes $\mathbf{D}_q \perp \text{axis}$ and $\mathbf{E}_q \parallel \text{axis}$, while there is no constraint on \mathbf{F}_q [Fig. 1(c)].

(d) The mirror symmetry with respect to the plane parallel to \mathbf{q} imposes $\mathbf{D}_q \perp \text{plane}$ and $\mathbf{E}_q \perp \text{plane}$, while there is no constraint on \mathbf{F}_q [Fig. 1(d)].

(e) The twofold rotational symmetry around the axis parallel to \mathbf{q} imposes $\mathbf{D}_q \parallel \text{axis}$ and $\mathbf{E}_q \parallel \text{axis}$, while there is no constraint on \mathbf{F}_q [Fig. 1(e)].

(f) The n -fold ($n = 3, 4, 6$) rotational symmetries around the axis parallel to \mathbf{q} imposes $\mathbf{D}_q \parallel \text{axis}$, $\mathbf{E}_q = \mathbf{0}$, and $\mathbf{F}_q = (F_q^{x_s}, F_q^\perp, F_q^\perp)$ [Fig. 1(f)].

Here, x_s is taken along the \mathbf{q} direction, and each operation leaves the origin $\mathbf{q} = (0, 0, 0)$ invariant. A detailed discussion is given in Appendix A. The rules do not change in the presence of the magnetic field due to the characteristic of the bilinear coupling of $\mathbf{S}_{\pm q}$.

The above rules indicate that nonzero components of \mathbf{D}_q and \mathbf{E}_q largely depend on the point-group symmetry, while there is only one constraint for \mathbf{F}_q . In particular, the rules for \mathbf{D}_q are the counterpart in momentum space of Moriya's rule in real space [91]. In addition, the condition for the symmetric off-diagonal interaction \mathbf{E}_q is also obtained, where

TABLE I. Symmetry constraint on $\mathcal{X}_{AB;q}$ when the point-group symmetry fixes the sublattices A and B. The point-group symmetries in momentum space in the left column correspond to those in Fig. 1.

Symmetry	Constraint on $\mathcal{X}_{AB;q}$
Inversion center	$\text{Im}(\mathcal{D}_{AB;q}) = \mathbf{0}, \text{Im}(\mathcal{E}_{AB;q}) = \mathbf{0}, \text{Im}(\mathcal{F}_{AB;q}) = \mathbf{0}$
Mirror plane $\perp \mathbf{q}$	$\text{Re}(\mathcal{D}_{AB;q}) \perp \text{plane}, \text{Im}(\mathcal{D}_{AB;q}) \parallel \text{plane}, \text{Re}(\mathcal{E}_{AB;q}) \perp \text{plane}, \text{Im}(\mathcal{E}_{AB;q}) \parallel \text{plane}, \text{Im}(\mathcal{F}_{AB;q}) = \mathbf{0}$
Twofold axis $\perp \mathbf{q}$	$\text{Re}(\mathcal{D}_{AB;q}) \parallel \text{axis}, \text{Im}(\mathcal{D}_{AB;q}) \perp \text{axis}, \text{Re}(\mathcal{E}_{AB;q}) \parallel \text{axis}, \text{Im}(\mathcal{E}_{AB;q}) \perp \text{axis}, \text{Im}(\mathcal{F}_{AB;q}) = \mathbf{0}$
Mirror plane $\parallel \mathbf{q}$	$\mathcal{D}_{AB;q} \perp \text{plane}, \mathcal{E}_{AB;q} \perp \text{plane}$
Twofold axis $\parallel \mathbf{q}$	$\mathcal{D}_{AB;q} \parallel \text{axis}, \mathcal{E}_{AB;q} \parallel \text{axis}$

the nonzero component of \mathbf{E}_q is different from (the same as) that of \mathbf{D}_q for the rules (a)–(c), and (f) [(d) and (e)]. Thus, the above rules are regarded as an extension of Moriya's rule to the momentum space and symmetric interactions.

2. Multisublattice case

Next, we extend the above results to multisublattice cases. The general expression of the momentum-resolved exchange interactions is described by

$$\sum_{\mu, \nu} S_{\mu q}^T \mathcal{X}_{\mu\nu;q} S_{\nu - q}, \quad (7)$$

with

$$\mathcal{X}_{\mu\nu;q} = \begin{pmatrix} \mathcal{F}_{\mu\nu;q}^{x_s} & \mathcal{E}_{\mu\nu;q}^{z_s} + \mathcal{D}_{\mu\nu;q}^{z_s} & \mathcal{E}_{\mu\nu;q}^{y_s} - \mathcal{D}_{\mu\nu;q}^{y_s} \\ \mathcal{E}_{\mu\nu;q}^{z_s} - \mathcal{D}_{\mu\nu;q}^{z_s} & \mathcal{F}_{\mu\nu;q}^{y_s} & \mathcal{E}_{\mu\nu;q}^{x_s} + \mathcal{D}_{\mu\nu;q}^{x_s} \\ \mathcal{E}_{\mu\nu;q}^{y_s} + \mathcal{D}_{\mu\nu;q}^{y_s} & \mathcal{E}_{\mu\nu;q}^{x_s} - \mathcal{D}_{\mu\nu;q}^{x_s} & \mathcal{F}_{\mu\nu;q}^{z_s} \end{pmatrix}. \quad (8)$$

$S_{\mu q}^T = (S_{\mu q}^{x_s}, S_{\mu q}^{y_s}, S_{\mu q}^{z_s})$ is the Fourier transform of the spin on the sublattice μ and $\mathcal{X}_{\mu\nu;q} = \mathcal{X}_{\nu\mu;q}^\dagger$. The interaction matrix $\mathcal{X}_{\mu\nu;q}$ is an extension of X_q in Eq. (3), which is composed of the complex coupling constants $\mathcal{D}_{\mu\nu;q} = (\mathcal{D}_{\mu\nu;q}^{x_s}, \mathcal{D}_{\mu\nu;q}^{y_s}, \mathcal{D}_{\mu\nu;q}^{z_s})$, $\mathcal{E}_{\mu\nu;q} = (\mathcal{E}_{\mu\nu;q}^{x_s}, \mathcal{E}_{\mu\nu;q}^{y_s}, \mathcal{E}_{\mu\nu;q}^{z_s})$, and $\mathcal{F}_{\mu\nu;q} = (\mathcal{F}_{\mu\nu;q}^{x_s}, \mathcal{F}_{\mu\nu;q}^{y_s}, \mathcal{F}_{\mu\nu;q}^{z_s})$. For $\mu = \nu$ ($\mu \neq \nu$), $\mathcal{X}_{\mu\nu;q}$ represents the intrasublattice (intersublattice) interaction; $\mathcal{X}_{\mu\mu;q}$ has nine independent components because $\text{Re}(\mathcal{D}_{\mu\mu;q}) = \text{Im}(\mathcal{E}_{\mu\mu;q}) = \text{Im}(\mathcal{F}_{\mu\mu;q}) = \mathbf{0}$ similar to X_q in Eq. (3), while $\mathcal{X}_{\mu\nu;q}$ for $\mu \neq \nu$ has 18 independent

components. Here, $\mathcal{D}_{\mu\nu;q}$ ($\mathcal{E}_{\mu\nu;q}$ and $\mathcal{F}_{\mu\nu;q}$) corresponds to the antisymmetric (symmetric) interactions in spin space; $\text{Re}(\mathcal{D}_{\mu\nu;q})$, $\text{Im}(\mathcal{E}_{\mu\nu;q})$, and $\text{Im}(\mathcal{F}_{\mu\nu;q})$ [$\text{Im}(\mathcal{D}_{\mu\nu;q})$, $\text{Re}(\mathcal{E}_{\mu\nu;q})$, and $\text{Re}(\mathcal{F}_{\mu\nu;q})$] correspond to the antisymmetric (symmetric) interactions for $\mu \leftrightarrow \nu$; $\text{Re}(\mathcal{D}_{\mu\nu;q})$, $\text{Re}(\mathcal{E}_{\mu\nu;q})$, and $\text{Re}(\mathcal{F}_{\mu\nu;q})$ [$\text{Im}(\mathcal{D}_{\mu\nu;q})$, $\text{Im}(\mathcal{E}_{\mu\nu;q})$, and $\text{Im}(\mathcal{F}_{\mu\nu;q})$] correspond to the symmetric (antisymmetric) interactions for $\mathbf{q} \rightarrow -\mathbf{q}$.

Similar to X_q in Sec. II A 1, the symmetry rules for $\mathcal{X}_{\mu\nu;q}$ are obtained by the magnetic representation analysis, as detailed in Appendix A. Since the interaction is defined in the momentum space as well as the primitive-lattice case, it is enough to consider the six point-group symmetries in Fig. 1 to obtain nonzero components of $\mathcal{X}_{\mu\nu;q}$. The different point from the primitive-lattice case is to take into account the permutation among the sublattices in each symmetry operation. In the following, we give the symmetry rules for $\mathcal{X}_{\mu\nu;q}$ in two and three sublattice systems as specific examples. As we list the general rules for the permutation among the sublattices, the following analyses are straightforwardly extended to more than three-sublattice systems. To simplify the rules, we consider the situation where the wave vector \mathbf{q} is inside the Brillouin zone and perpendicular to the principal axis, which means that there are no symmetry constraints by the n -fold ($n = 3, 4, 6$) rotational symmetry around \mathbf{q} in Fig. 1(f).

First, we consider the symmetry rules in terms of $\mathcal{X}_{AA;q}$, $\mathcal{X}_{BB;q}$, and $\mathcal{X}_{AB;q} (= \mathcal{X}_{BA;q}^\dagger)$ for the two-sublattice case, i.e., $\mu, \nu = A, B$ in Eq. (7). In contrast to the primitive-lattice case, the symmetry rules change depending on the permutation symmetry of the sublattices; we divide the cases where

TABLE II. Symmetry constraint between $\mathcal{X}_{AA;q}$ and $\mathcal{X}_{BB;q}$ when the point group symmetry interchanges the sublattices A and B. The point group symmetries in momentum space in the left column correspond to those in Fig. 1. The superscript $\parallel \#$ ($\perp \#$) represents the components parallel (perpendicular) to $\#$, where $\#$ denotes any of axis and plane.

Symmetry	Constraint on $\mathcal{X}_{AA;q}$ and $\mathcal{X}_{BB;q}$
Inversion center	$\text{Im}(\mathcal{D}_{AA;q}) = -\text{Im}(\mathcal{D}_{BB;q}), \text{Re}(\mathcal{E}_{AA;q}) = \text{Re}(\mathcal{E}_{BB;q}), \text{Re}(\mathcal{F}_{AA;q}) = \text{Re}(\mathcal{F}_{BB;q})$
Mirror plane $\perp \mathbf{q}$	$\text{Im}(\mathcal{D}_{AA;q}^{\parallel \text{plane}}) = \text{Im}(\mathcal{D}_{BB;q}^{\parallel \text{plane}}), \text{Im}(\mathcal{D}_{AA;q}^{\perp \text{plane}}) = -\text{Im}(\mathcal{D}_{BB;q}^{\perp \text{plane}}),$ $\text{Re}(\mathcal{E}_{AA;q}^{\parallel \text{plane}}) = -\text{Re}(\mathcal{E}_{BB;q}^{\parallel \text{plane}}), \text{Re}(\mathcal{E}_{AA;q}^{\perp \text{plane}}) = \text{Re}(\mathcal{E}_{BB;q}^{\perp \text{plane}}), \text{Re}(\mathcal{F}_{AA;q}) = \text{Re}(\mathcal{F}_{BB;q})$
Twofold axis $\perp \mathbf{q}$	$\text{Im}(\mathcal{D}_{AA;q}^{\perp \text{axis}}) = \text{Im}(\mathcal{D}_{BB;q}^{\perp \text{axis}}), \text{Im}(\mathcal{D}_{AA;q}^{\parallel \text{axis}}) = -\text{Im}(\mathcal{D}_{BB;q}^{\parallel \text{axis}}),$ $\text{Re}(\mathcal{E}_{AA;q}^{\perp \text{axis}}) = -\text{Re}(\mathcal{E}_{BB;q}^{\perp \text{axis}}), \text{Re}(\mathcal{E}_{AA;q}^{\parallel \text{axis}}) = \text{Re}(\mathcal{E}_{BB;q}^{\parallel \text{axis}}), \text{Re}(\mathcal{F}_{AA;q}) = \text{Re}(\mathcal{F}_{BB;q})$
Mirror plane $\parallel \mathbf{q}$	$\text{Im}(\mathcal{D}_{AA;q}^{\perp \text{plane}}) = \text{Im}(\mathcal{D}_{BB;q}^{\perp \text{plane}}), \text{Im}(\mathcal{D}_{AA;q}^{\parallel \text{plane}}) = -\text{Im}(\mathcal{D}_{BB;q}^{\parallel \text{plane}}),$ $\text{Re}(\mathcal{E}_{AA;q}^{\perp \text{plane}}) = \text{Re}(\mathcal{E}_{BB;q}^{\perp \text{plane}}), \text{Re}(\mathcal{E}_{AA;q}^{\parallel \text{plane}}) = -\text{Re}(\mathcal{E}_{BB;q}^{\parallel \text{plane}}), \text{Re}(\mathcal{F}_{AA;q}) = \text{Re}(\mathcal{F}_{BB;q})$
Twofold axis $\parallel \mathbf{q}$	$\text{Im}(\mathcal{D}_{AA;q}^{\perp \text{axis}}) = -\text{Im}(\mathcal{D}_{BB;q}^{\perp \text{axis}}), \text{Im}(\mathcal{D}_{AA;q}^{\parallel \text{axis}}) = \text{Im}(\mathcal{D}_{BB;q}^{\parallel \text{axis}}),$ $\text{Re}(\mathcal{E}_{AA;q}^{\perp \text{axis}}) = -\text{Re}(\mathcal{E}_{BB;q}^{\perp \text{axis}}), \text{Re}(\mathcal{E}_{AA;q}^{\parallel \text{axis}}) = \text{Re}(\mathcal{E}_{BB;q}^{\parallel \text{axis}}), \text{Re}(\mathcal{F}_{AA;q}) = \text{Re}(\mathcal{F}_{BB;q})$

TABLE III. Symmetry constraint on $\mathcal{X}_{AB;q}$ when the point-group symmetry interchanges the sublattices A and B. The point-group symmetries in momentum space in the left column correspond to those in Fig. 1.

Symmetry	Constraint on $\mathcal{X}_{AB;q}$
Inversion center	$\mathcal{D}_{AB;q} = 0$
Mirror plane $\perp \mathbf{q}$	$\mathcal{D}_{AB;q} \parallel \text{plane}, \mathcal{E}_{AB;q} \perp \text{plane}$
Twofold axis $\perp \mathbf{q}$	$\mathcal{D}_{AB;q} \perp \text{axis}, \mathcal{E}_{AB;q} \parallel \text{axis}$
Mirror plane $\parallel \mathbf{q}$	$\text{Re}(\mathcal{D}_{AB;q}) \parallel \text{plane}, \text{Im}(\mathcal{D}_{AB;q}) \perp \text{plane}, \text{Re}(\mathcal{E}_{AB;q}) \perp \text{plane}, \text{Im}(\mathcal{E}_{AB;q}) \parallel \text{plane}, \text{Im}(\mathcal{F}_{AB;q}) = 0$
Twofold axis $\parallel \mathbf{q}$	$\text{Re}(\mathcal{D}_{AB;q}) \perp \text{axis}, \text{Im}(\mathcal{D}_{AB;q}) \parallel \text{axis}, \text{Re}(\mathcal{E}_{AB;q}) \parallel \text{axis}, \text{Im}(\mathcal{E}_{AB;q}) \perp \text{axis}, \text{Im}(\mathcal{F}_{AB;q}) = 0$

the point-group symmetry (i) fixes or (ii) interchanges the sublattices A and B. In the case (i), the symmetry constraint on $\mathcal{X}_{AA;q}$ ($\mathcal{X}_{BB;q}$) is the same as that for X_q shown in Figs. 1(a)–1(e), while the symmetry rules for $\mathcal{X}_{AB;q}$ are summarized in Table I. In this case, there is no constraint between $\mathcal{X}_{AA;q}$ and $\mathcal{X}_{BB;q}$. In the case (ii), the point-group symmetry imposes constraints between $\mathcal{X}_{AA;q}$ and $\mathcal{X}_{BB;q}$ and those on $\mathcal{X}_{AB;q}$, as summarized in Tables II and III, respectively.

Next, we present the symmetry rules for the three-sublattice case, i.e., $\mu, \nu = A, B, C$. There are three cases according to the permutation symmetry: The point-group symmetry (i) fixes the sublattices A, B, and C, (ii) interchanges the sublattices A and B but fixes the sublattice C, and (iii) cyclically interchanges the sublattices A, B, and C. Here, we only consider the cases (i) and (ii) since the case (iii) is rare for \mathbf{q} perpendicular to the principal axis. In the case (i), the symmetry constraint on $\mathcal{X}_{AA;q}$, $\mathcal{X}_{BB;q}$, and $\mathcal{X}_{CC;q}$ is the same as that for X_q shown in Figs. 1(a)–1(e). Besides, the symmetry rules for $\mathcal{X}_{AB;q}$, $\mathcal{X}_{BC;q}$, and $\mathcal{X}_{CA;q}$ are the same as those for $\mathcal{X}_{AB;q}$ shown in Table I. In the case (ii), the symmetry constraints between $\mathcal{X}_{BC;q}$ and $\mathcal{X}_{CA;q}$ are qualitatively different from the two-sublattice case, which are summarized in Table IV. Meanwhile, the symmetry rules for the other interaction matrices are obtained by using the above results; the symmetry constraint on $\mathcal{X}_{CC;q}$ is the same as that for X_q shown in Figs. 1(a)–1(e), and the symmetry constraint on $\mathcal{X}_{AA;q}$, $\mathcal{X}_{BB;q}$, and $\mathcal{X}_{AB;q}$ is the same as that shown in Tables II and III.

TABLE IV. Symmetry constraint between $\mathcal{X}_{CA;q}$ and $\mathcal{X}_{BC;q}$ when the point-group symmetry interchanges the sublattices A and B but fixes the sublattice C. The point-group symmetries in momentum space in the left column correspond to those in Fig. 1. The superscript $\parallel \#$ ($\perp \#$) represents the components parallel (perpendicular) to $\#$, where $\#$ denotes any axis and plane.

Symmetry	Constraint on $\mathcal{X}_{CA;q}$ and $\mathcal{X}_{BC;q}$
Inversion center	$\mathcal{D}_{CA;q} = -\mathcal{D}_{BC;q}, \mathcal{E}_{CA;q} = \mathcal{E}_{BC;q}, \mathcal{F}_{CA;q} = \mathcal{F}_{BC;q}$
Mirror plane $\perp \mathbf{q}$	$\mathcal{D}_{CA;q}^{\parallel \text{plane}} = \mathcal{D}_{BC;q}^{\parallel \text{plane}}, \mathcal{D}_{CA;q}^{\perp \text{plane}} = -\mathcal{D}_{BC;q}^{\perp \text{plane}}, \mathcal{E}_{CA;q}^{\parallel \text{plane}} = -\mathcal{E}_{BC;q}^{\parallel \text{plane}}, \mathcal{E}_{CA;q}^{\perp \text{plane}} = \mathcal{E}_{BC;q}^{\perp \text{plane}}, \mathcal{F}_{CA;q} = \mathcal{F}_{BC;q}$
Twofold axis $\perp \mathbf{q}$	$\mathcal{D}_{CA;q}^{\perp \text{axis}} = \mathcal{D}_{BC;q}^{\perp \text{axis}}, \mathcal{D}_{CA;q}^{\parallel \text{axis}} = -\mathcal{D}_{BC;q}^{\parallel \text{axis}}, \mathcal{E}_{CA;q}^{\perp \text{axis}} = -\mathcal{E}_{BC;q}^{\perp \text{axis}}, \mathcal{E}_{CA;q}^{\parallel \text{axis}} = \mathcal{E}_{BC;q}^{\parallel \text{axis}}, \mathcal{F}_{CA;q} = \mathcal{F}_{BC;q}$
Mirror plane $\parallel \mathbf{q}$	$\text{Re}(\mathcal{D}_{CA;q}^{\parallel \text{plane}}) = -\text{Re}(\mathcal{D}_{BC;q}^{\parallel \text{plane}}), \text{Re}(\mathcal{D}_{CA;q}^{\perp \text{plane}}) = \text{Re}(\mathcal{D}_{BC;q}^{\perp \text{plane}}), \text{Im}(\mathcal{D}_{CA;q}^{\parallel \text{plane}}) = \text{Im}(\mathcal{D}_{BC;q}^{\parallel \text{plane}}),$ $\text{Im}(\mathcal{D}_{CA;q}^{\perp \text{plane}}) = -\text{Im}(\mathcal{D}_{BC;q}^{\perp \text{plane}}), \text{Re}(\mathcal{E}_{CA;q}^{\parallel \text{plane}}) = \text{Re}(\mathcal{E}_{BC;q}^{\parallel \text{plane}}), \text{Re}(\mathcal{E}_{CA;q}^{\perp \text{plane}}) = -\text{Re}(\mathcal{E}_{BC;q}^{\perp \text{plane}}),$ $\text{Im}(\mathcal{E}_{CA;q}^{\parallel \text{plane}}) = -\text{Im}(\mathcal{E}_{BC;q}^{\parallel \text{plane}}), \text{Im}(\mathcal{E}_{CA;q}^{\perp \text{plane}}) = \text{Im}(\mathcal{E}_{BC;q}^{\perp \text{plane}}), \text{Re}(\mathcal{F}_{CA;q}) = \text{Re}(\mathcal{F}_{BC;q}), \text{Im}(\mathcal{F}_{CA;q}) = -\text{Im}(\mathcal{F}_{BC;q})$
Twofold axis $\parallel \mathbf{q}$	$\text{Re}(\mathcal{D}_{CA;q}^{\perp \text{axis}}) = \text{Re}(\mathcal{D}_{BC;q}^{\perp \text{axis}}), \text{Re}(\mathcal{D}_{CA;q}^{\parallel \text{axis}}) = -\text{Re}(\mathcal{D}_{BC;q}^{\parallel \text{axis}}), \text{Im}(\mathcal{D}_{CA;q}^{\perp \text{axis}}) = -\text{Im}(\mathcal{D}_{BC;q}^{\perp \text{axis}}), \text{Im}(\mathcal{D}_{CA;q}^{\parallel \text{axis}}) = \text{Im}(\mathcal{D}_{BC;q}^{\parallel \text{axis}}),$ $\text{Re}(\mathcal{E}_{CA;q}^{\perp \text{axis}}) = -\text{Re}(\mathcal{E}_{BC;q}^{\perp \text{axis}}), \text{Re}(\mathcal{E}_{CA;q}^{\parallel \text{axis}}) = \text{Re}(\mathcal{E}_{BC;q}^{\parallel \text{axis}}), \text{Im}(\mathcal{E}_{CA;q}^{\perp \text{axis}}) = \text{Im}(\mathcal{E}_{BC;q}^{\perp \text{axis}}), \text{Im}(\mathcal{E}_{CA;q}^{\parallel \text{axis}}) = -\text{Im}(\mathcal{E}_{BC;q}^{\parallel \text{axis}}),$ $\text{Re}(\mathcal{F}_{CA;q}) = \text{Re}(\mathcal{F}_{BC;q}), \text{Im}(\mathcal{F}_{CA;q}) = -\text{Im}(\mathcal{F}_{BC;q})$

B. Effective spin model under space groups

1. Primitive-lattice case

The above symmetry argument in Sec. II A 1 gives a general form of the spin Hamiltonian in any primitive-lattice systems, which is obtained by summing the contribution from the entire \mathbf{q} in the first Brillouin zone as

$$\mathcal{H} = - \sum_{\mathbf{q}} S_{\mathbf{q}}^T X_{\mathbf{q}} S_{-\mathbf{q}}, \quad (9)$$

where the minus sign is added for later convenience [see Eq. (38) in Sec. III C]. As a demonstration, we discuss here a specific form of $X_{\mathbf{q}}$ for 24 gray symmorphic space groups belonging to the tetragonal, hexagonal, and trigonal crystal systems shown in Tables V–VII. The gray symmorphic space group \mathbf{M} defined as $\mathbf{M} = \mathbf{H} + \theta \mathbf{H}$ with the symmorphic space group \mathbf{H} and the time-reversal operation θ [113]. In the model in Eq. (9), we take the spin coordinates x_s, y_s , and z_s along the x, y , and z directions, respectively, shown in Fig. 2(a).

Let us start by constructing an effective model (mean-field Hamiltonian) consisting of the interactions at specific wave vectors rather than all the wave vectors in the Brillouin zone, which is given by

$$\mathcal{H}^{\text{eff}} = - \sum_{\mathbf{q} \in \{\mathcal{Q}\}} S_{\mathbf{q}}^T X_{\mathbf{q}} S_{-\mathbf{q}}, \quad (10)$$

where $\{\mathcal{Q}\}$ represents a set of the symmetry-related wave vectors. For example, in the tetragonal crystal system, there are at least four symmetry-related wave vectors connected by the

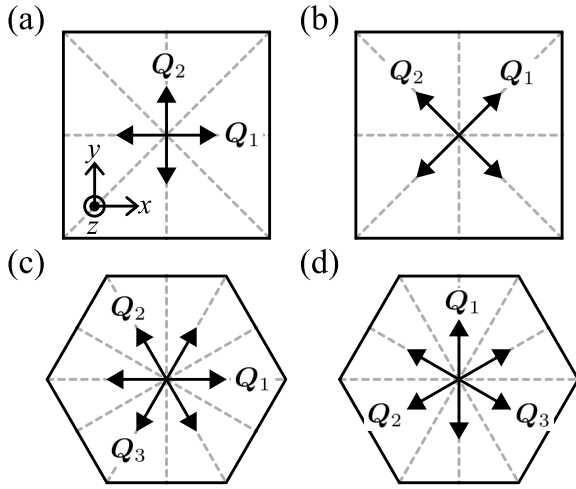


FIG. 2. A set of $\{\mathbf{Q}\}$ along the different high-symmetry lines inside the first Brillouin zone in (a),(b) tetragonal crystal systems and (c),(d) hexagonal and trigonal crystal systems. In (a) and (b), \mathbf{Q}_1 and \mathbf{Q}_2 are connected by the fourfold rotation around the z axis, while in (c) and (d), \mathbf{Q}_1 , \mathbf{Q}_2 , and \mathbf{Q}_3 are connected by the threefold rotation. The wave vectors in $\{\mathbf{Q}\}$ lie on the xy plane.

fourfold rotation, $\{\mathbf{Q}\} = \pm\mathbf{Q}_1, \pm\mathbf{Q}_2$, whereas there are at least six (three) symmetry-related wave vectors connected by the sixfold (threefold) rotation, $\{\mathbf{Q}\} = \pm\mathbf{Q}_1, \pm\mathbf{Q}_2, \pm\mathbf{Q}_3$ ($\{\mathbf{Q}\} = \mathbf{Q}_1, \mathbf{Q}_2, \mathbf{Q}_3$), in the hexagonal (trigonal) crystal system.

Once $\{\mathbf{Q}\}$ and the space group in the model in Eq. (10) are determined, we can write down nonzero components of X_q following the rules in Sec. II A 1. We present the results of X_q in the tetragonal, hexagonal, and trigonal crystal systems, where the wave vectors lie along the high-symmetry lines; \mathbf{Q}_1 is taken along the x [Fig. 2(a)] and $[110]$ [Fig. 2(b)] axes in the tetragonal crystal system, while \mathbf{Q}_1 is taken along the x [Fig. 2(c)] and y [Fig. 2(d)] axes in the hexagonal and trigonal crystal systems. The specific form of $X_{\mathbf{Q}_1}$ is summarized in Table V for the tetragonal crystal systems ($P4/mmm$, $P422$, $P\bar{4}2m$, $P\bar{4}m2$, $P4mm$, $P4/m$, $P4$, and $P\bar{4}$), Table VI for the hexagonal crystal systems ($P6/mmm$, $P622$, $P\bar{6}m2$, $P\bar{6}2m$, $P6mm$, $P6/m$, $P\bar{6}$, and $P6$), and Table VII for the trigonal crystal systems ($P\bar{3}m1$, $P\bar{3}1m$, $P321$, $P312$, $P3m1$, $P\bar{3}$, and $P3$). In Tables V–VII, N_c stands for the number of independent components of $X_{\mathbf{Q}_1}$. X_q for the low-symmetric $\{\mathbf{Q}\}$ is also obtained by using the same rules, as shown in Appendix B.

TABLE V. Interaction matrix $X_{\mathbf{Q}_1}$ and the number of independent components N_c in the tetragonal crystal systems for the high-symmetric wave vector \mathbf{Q}_1 shown in Figs. 2(a) and 2(b). The spin coordinates x_s , y_s , and z_s are taken along the x , y , and z directions in Fig. 2(a), respectively.

Space group \mathbf{H}	$\mathbf{Q}_1 \parallel \hat{x}$		$\mathbf{Q}_1 \parallel [110]$	
	$X_{\mathbf{Q}_1}$	N_c	$X_{\mathbf{Q}_1}$	N_c
$P4/mmm$	$\begin{pmatrix} F_{\mathbf{Q}_1}^x & 0 & 0 \\ 0 & F_{\mathbf{Q}_1}^y & 0 \\ 0 & 0 & F_{\mathbf{Q}_1}^z \end{pmatrix}$	3	$\begin{pmatrix} F_{\mathbf{Q}_1}^x & E_{\mathbf{Q}_1}^z & 0 \\ E_{\mathbf{Q}_1}^z & F_{\mathbf{Q}_1}^x & 0 \\ 0 & 0 & F_{\mathbf{Q}_1}^z \end{pmatrix}$	3
$P422$	$\begin{pmatrix} F_{\mathbf{Q}_1}^x & 0 & 0 \\ 0 & F_{\mathbf{Q}_1}^y & iD_{\mathbf{Q}_1}^x \\ 0 & -iD_{\mathbf{Q}_1}^x & F_{\mathbf{Q}_1}^z \end{pmatrix}$	4	$\begin{pmatrix} F_{\mathbf{Q}_1}^x & E_{\mathbf{Q}_1}^z & -iD_{\mathbf{Q}_1}^x \\ E_{\mathbf{Q}_1}^z & F_{\mathbf{Q}_1}^x & iD_{\mathbf{Q}_1}^x \\ iD_{\mathbf{Q}_1}^x & -iD_{\mathbf{Q}_1}^x & F_{\mathbf{Q}_1}^z \end{pmatrix}$	4
$P\bar{4}2m$	$\begin{pmatrix} F_{\mathbf{Q}_1}^x & 0 & 0 \\ 0 & F_{\mathbf{Q}_1}^y & iD_{\mathbf{Q}_1}^x \\ 0 & -iD_{\mathbf{Q}_1}^x & F_{\mathbf{Q}_1}^z \end{pmatrix}$	4	$\begin{pmatrix} F_{\mathbf{Q}_1}^x & E_{\mathbf{Q}_1}^z & iD_{\mathbf{Q}_1}^x \\ E_{\mathbf{Q}_1}^z & F_{\mathbf{Q}_1}^x & iD_{\mathbf{Q}_1}^x \\ -iD_{\mathbf{Q}_1}^x & -iD_{\mathbf{Q}_1}^x & F_{\mathbf{Q}_1}^z \end{pmatrix}$	4
$P\bar{4}m2$	$\begin{pmatrix} F_{\mathbf{Q}_1}^x & 0 & -iD_{\mathbf{Q}_1}^y \\ 0 & F_{\mathbf{Q}_1}^y & 0 \\ iD_{\mathbf{Q}_1}^y & 0 & F_{\mathbf{Q}_1}^z \end{pmatrix}$	4	$\begin{pmatrix} F_{\mathbf{Q}_1}^x & E_{\mathbf{Q}_1}^z & -iD_{\mathbf{Q}_1}^y \\ E_{\mathbf{Q}_1}^z & F_{\mathbf{Q}_1}^x & iD_{\mathbf{Q}_1}^y \\ iD_{\mathbf{Q}_1}^y & -iD_{\mathbf{Q}_1}^y & F_{\mathbf{Q}_1}^z \end{pmatrix}$	4
$P4mm$	$\begin{pmatrix} F_{\mathbf{Q}_1}^x & 0 & -iD_{\mathbf{Q}_1}^y \\ 0 & F_{\mathbf{Q}_1}^y & 0 \\ iD_{\mathbf{Q}_1}^y & 0 & F_{\mathbf{Q}_1}^z \end{pmatrix}$	4	$\begin{pmatrix} F_{\mathbf{Q}_1}^x & E_{\mathbf{Q}_1}^z & iD_{\mathbf{Q}_1}^y \\ E_{\mathbf{Q}_1}^z & F_{\mathbf{Q}_1}^x & iD_{\mathbf{Q}_1}^y \\ -iD_{\mathbf{Q}_1}^y & -iD_{\mathbf{Q}_1}^y & F_{\mathbf{Q}_1}^z \end{pmatrix}$	4
$P4/m$	$\begin{pmatrix} F_{\mathbf{Q}_1}^x & E_{\mathbf{Q}_1}^z & 0 \\ E_{\mathbf{Q}_1}^z & F_{\mathbf{Q}_1}^x & 0 \\ 0 & 0 & F_{\mathbf{Q}_1}^z \end{pmatrix}$	4	$\begin{pmatrix} F_{\mathbf{Q}_1}^x & E_{\mathbf{Q}_1}^z & 0 \\ E_{\mathbf{Q}_1}^z & F_{\mathbf{Q}_1}^x & 0 \\ 0 & 0 & F_{\mathbf{Q}_1}^z \end{pmatrix}$	4
$P4$	$\begin{pmatrix} F_{\mathbf{Q}_1}^x & E_{\mathbf{Q}_1}^z & -iD_{\mathbf{Q}_1}^y \\ E_{\mathbf{Q}_1}^z & F_{\mathbf{Q}_1}^x & iD_{\mathbf{Q}_1}^y \\ iD_{\mathbf{Q}_1}^y & -iD_{\mathbf{Q}_1}^y & F_{\mathbf{Q}_1}^z \end{pmatrix}$	6	$\begin{pmatrix} F_{\mathbf{Q}_1}^x & E_{\mathbf{Q}_1}^z & -iD_{\mathbf{Q}_1}^y \\ E_{\mathbf{Q}_1}^z & F_{\mathbf{Q}_1}^x & iD_{\mathbf{Q}_1}^y \\ iD_{\mathbf{Q}_1}^y & -iD_{\mathbf{Q}_1}^y & F_{\mathbf{Q}_1}^z \end{pmatrix}$	6
$P\bar{4}$	$\begin{pmatrix} F_{\mathbf{Q}_1}^x & E_{\mathbf{Q}_1}^z & -iD_{\mathbf{Q}_1}^y \\ E_{\mathbf{Q}_1}^z & F_{\mathbf{Q}_1}^x & iD_{\mathbf{Q}_1}^y \\ iD_{\mathbf{Q}_1}^y & -iD_{\mathbf{Q}_1}^y & F_{\mathbf{Q}_1}^z \end{pmatrix}$	6	$\begin{pmatrix} F_{\mathbf{Q}_1}^x & E_{\mathbf{Q}_1}^z & -iD_{\mathbf{Q}_1}^y \\ E_{\mathbf{Q}_1}^z & F_{\mathbf{Q}_1}^x & iD_{\mathbf{Q}_1}^y \\ iD_{\mathbf{Q}_1}^y & -iD_{\mathbf{Q}_1}^y & F_{\mathbf{Q}_1}^z \end{pmatrix}$	6

TABLE VI. Interaction matrix $X_{\mathbf{Q}_1}$ and the number of independent components N_c in the hexagonal crystal systems for the high-symmetric wave vector \mathbf{Q}_1 shown in Figs. 2(c) and 2(d). The spin coordinates x_s , y_s , and z_s are taken along the x , y , and z directions in Fig. 2(a), respectively.

Space group \mathbf{H}	$\mathbf{Q}_1 \parallel \hat{x}$		$\mathbf{Q}_1 \parallel \hat{y}$	
	$X_{\mathbf{Q}_1}$	N_c	$X_{\mathbf{Q}_1}$	N_c
$P6/mmm$	$\begin{pmatrix} F_{\mathbf{Q}_1}^x & 0 & 0 \\ 0 & F_{\mathbf{Q}_1}^y & 0 \\ 0 & 0 & F_{\mathbf{Q}_1}^z \end{pmatrix}$	3	$\begin{pmatrix} F_{\mathbf{Q}_1}^x & 0 & 0 \\ 0 & F_{\mathbf{Q}_1}^y & 0 \\ 0 & 0 & F_{\mathbf{Q}_1}^z \end{pmatrix}$	3
$P622$	$\begin{pmatrix} F_{\mathbf{Q}_1}^x & 0 & 0 \\ 0 & F_{\mathbf{Q}_1}^y & iD_{\mathbf{Q}_1}^x \\ 0 & -iD_{\mathbf{Q}_1}^y & F_{\mathbf{Q}_1}^z \end{pmatrix}$	4	$\begin{pmatrix} F_{\mathbf{Q}_1}^x & 0 & -iD_{\mathbf{Q}_1}^y \\ 0 & F_{\mathbf{Q}_1}^y & 0 \\ iD_{\mathbf{Q}_1}^x & 0 & F_{\mathbf{Q}_1}^z \end{pmatrix}$	4
$P\bar{6}m2$	$\begin{pmatrix} F_{\mathbf{Q}_1}^x & iD_{\mathbf{Q}_1}^x & 0 \\ -iD_{\mathbf{Q}_1}^y & F_{\mathbf{Q}_1}^y & 0 \\ 0 & 0 & F_{\mathbf{Q}_1}^z \end{pmatrix}$	4	$\begin{pmatrix} F_{\mathbf{Q}_1}^x & 0 & 0 \\ 0 & F_{\mathbf{Q}_1}^y & 0 \\ 0 & 0 & F_{\mathbf{Q}_1}^z \end{pmatrix}$	3
$P\bar{6}2m$	$\begin{pmatrix} F_{\mathbf{Q}_1}^x & 0 & 0 \\ 0 & F_{\mathbf{Q}_1}^y & 0 \\ 0 & 0 & F_{\mathbf{Q}_1}^z \end{pmatrix}$	3	$\begin{pmatrix} F_{\mathbf{Q}_1}^x & iD_{\mathbf{Q}_1}^z & 0 \\ -iD_{\mathbf{Q}_1}^y & F_{\mathbf{Q}_1}^y & 0 \\ 0 & 0 & F_{\mathbf{Q}_1}^z \end{pmatrix}$	4
$P6mm$	$\begin{pmatrix} F_{\mathbf{Q}_1}^x & 0 & -iD_{\mathbf{Q}_1}^y \\ 0 & F_{\mathbf{Q}_1}^y & 0 \\ iD_{\mathbf{Q}_1}^x & 0 & F_{\mathbf{Q}_1}^z \end{pmatrix}$	4	$\begin{pmatrix} F_{\mathbf{Q}_1}^x & 0 & 0 \\ 0 & F_{\mathbf{Q}_1}^y & iD_{\mathbf{Q}_1}^x \\ 0 & -iD_{\mathbf{Q}_1}^y & F_{\mathbf{Q}_1}^z \end{pmatrix}$	4
$P6/m$	$\begin{pmatrix} F_{\mathbf{Q}_1}^x & E_{\mathbf{Q}_1}^z & 0 \\ E_{\mathbf{Q}_1}^z & F_{\mathbf{Q}_1}^y & 0 \\ 0 & 0 & F_{\mathbf{Q}_1}^z \end{pmatrix}$	4	$\begin{pmatrix} F_{\mathbf{Q}_1}^x & E_{\mathbf{Q}_1}^z & 0 \\ E_{\mathbf{Q}_1}^z & F_{\mathbf{Q}_1}^y & 0 \\ 0 & 0 & F_{\mathbf{Q}_1}^z \end{pmatrix}$	4
$P\bar{6}$	$\begin{pmatrix} F_{\mathbf{Q}_1}^x & E_{\mathbf{Q}_1}^z + iD_{\mathbf{Q}_1}^x & 0 \\ E_{\mathbf{Q}_1}^z - iD_{\mathbf{Q}_1}^y & F_{\mathbf{Q}_1}^y & 0 \\ 0 & 0 & F_{\mathbf{Q}_1}^z \end{pmatrix}$	5	$\begin{pmatrix} F_{\mathbf{Q}_1}^x & E_{\mathbf{Q}_1}^z + iD_{\mathbf{Q}_1}^x & 0 \\ E_{\mathbf{Q}_1}^z - iD_{\mathbf{Q}_1}^y & F_{\mathbf{Q}_1}^y & 0 \\ 0 & 0 & F_{\mathbf{Q}_1}^z \end{pmatrix}$	5
$P6$	$\begin{pmatrix} F_{\mathbf{Q}_1}^x & E_{\mathbf{Q}_1}^z & -iD_{\mathbf{Q}_1}^y \\ E_{\mathbf{Q}_1}^z & F_{\mathbf{Q}_1}^y & iD_{\mathbf{Q}_1}^x \\ iD_{\mathbf{Q}_1}^y & -iD_{\mathbf{Q}_1}^x & F_{\mathbf{Q}_1}^z \end{pmatrix}$	6	$\begin{pmatrix} F_{\mathbf{Q}_1}^x & E_{\mathbf{Q}_1}^z & -iD_{\mathbf{Q}_1}^y \\ E_{\mathbf{Q}_1}^z & F_{\mathbf{Q}_1}^y & iD_{\mathbf{Q}_1}^x \\ iD_{\mathbf{Q}_1}^y & -iD_{\mathbf{Q}_1}^x & F_{\mathbf{Q}_1}^z \end{pmatrix}$	6

From Tables V–VII, one finds two features irrelevant to the details of the space group. First, there are at least three independent components ($N_c \geq 3$) in all cases. Among them, one component corresponds to the isotropic contribution, $F_q^{\text{iso}} = (F_q^x + F_q^y + F_q^z)/3$. Second, the antisymmetric interaction \mathbf{D}_q only appears in the absence of the spatial inversion symmetry, while the symmetric ones \mathbf{E}_q and \mathbf{F}_q appear irrespective of the inversion symmetry, as shown in rule (a) in Sec. II A 1.

In addition, there are three characteristics in Tables V–VII. The first is that the interaction matrix depends on not only the space group but also the direction of \mathbf{Q}_1 , which reflects the different symmetry of the wave vectors. In particular, $X_{\mathbf{Q}_1 \parallel \hat{x}}$ and $X_{\mathbf{Q}_1 \parallel \hat{y}}$ in $P\bar{6}m2$, $P\bar{6}2m$, $P321$, $P312$, $P3m1$, and $P31m$ crystals have a different number of independent components. The second is that the diagonal components of the interactions are different for all the space groups except for $\mathbf{Q}_1 \parallel [110]$ in $P4/mmm$, $P422$, $P\bar{4}2m$, $P4m2$, $P4mm$, and $P4/m$ crystal systems, i.e., $F_{\mathbf{Q}_1}^x \neq F_{\mathbf{Q}_1}^y \neq F_{\mathbf{Q}_1}^z$; the difference between $F_{\mathbf{Q}_1}^x$ and $F_{\mathbf{Q}_1}^z$ ($F_{\mathbf{Q}_1}^y$ and $F_{\mathbf{Q}_1}^z$) is due to an inequivalence between the in-plane and z directions, while that between $F_{\mathbf{Q}_1}^x$ and $F_{\mathbf{Q}_1}^y$ is due to the discrete rotational symmetry around the principal axis. It is noted that in the case of $\mathbf{Q}_1 \parallel [110]$ in $P4/mmm$, $P422$, $P\bar{4}2m$, $P\bar{4}m2$, $P4mm$, and $P4/m$ crystal systems, all the space groups allow nonzero $E_{\mathbf{Q}_1}^z$ instead of

different $F_{\mathbf{Q}_1}^x$ and $F_{\mathbf{Q}_1}^y$. The third is that the symmetric off-diagonal components, $E_{\mathbf{Q}_1}^x$ and $E_{\mathbf{Q}_1}^y$, only appear in the trigonal crystal systems, which do not have the twofold axis along the z direction and the horizontal mirror plane [see rules (c) and (d)]. Thus, a qualitatively different multiple- \mathbf{Q} state is expected under $E_{\mathbf{Q}_1}^x$ and $E_{\mathbf{Q}_1}^y$ in the trigonal crystal systems from that in the tetragonal and hexagonal crystal systems, as discussed in Sec. II C.

The other relevant interactions at the symmetry-related wave vectors in $\{\mathbf{Q}\}$ are obtained by rotating the interaction matrix $X_{\mathbf{Q}_1}$ by the angle ϕ , which is represented by

$$X_{\mathbf{Q}_\eta} = \Gamma(\phi) X_{\mathbf{Q}_1} \Gamma^{-1}(\phi), \quad (11)$$

where

$$\Gamma(\phi) = \begin{pmatrix} \sigma \cos \phi & -\sigma \sin \phi & 0 \\ \sigma \sin \phi & \sigma \cos \phi & 0 \\ 0 & 0 & 1 \end{pmatrix} \quad (12)$$

with $\sigma = 1$ ($\sigma = -1$) for the rotation (improper rotation) and $\eta = 2, 3$. Specifically, $X_{\mathbf{Q}_2}$ for $P4/mmm$, $P422$, $P4mm$, $P4/m$, and $P4$ ($P\bar{4}2m$, $P\bar{4}m2$, and $P\bar{4}$) are obtained by using Eqs. (11) and (12) with $\phi = \pi/2$ and $\sigma = 1$ ($\sigma = -1$), and $X_{\mathbf{Q}_2}$ ($X_{\mathbf{Q}_3}$) in the hexagonal and trigonal systems are obtained with

TABLE VII. Interaction matrix $X_{\mathbf{Q}_1}$ and the number of independent components N_c in the trigonal crystal systems for the high-symmetric wave vector \mathbf{Q}_1 shown in Figs. 2(c) and 2(d). The spin coordinates x_s , y_s , and z_s are taken along the x , y , and z directions in Fig. 2(a), respectively.

Space group \mathbf{H}	$\mathbf{Q}_1 \parallel \hat{x}$		$\mathbf{Q}_1 \parallel \hat{y}$	
	$X_{\mathbf{Q}_1}$	N_c	$X_{\mathbf{Q}_1}$	N_c
$P\bar{3}m1$	$\begin{pmatrix} F_{\mathbf{Q}_1}^x & 0 & 0 \\ 0 & F_{\mathbf{Q}_1}^y & E_{\mathbf{Q}_1}^x \\ 0 & E_{\mathbf{Q}_1}^x & F_{\mathbf{Q}_1}^z \end{pmatrix}$	4	$\begin{pmatrix} F_{\mathbf{Q}_1}^x & 0 & 0 \\ 0 & F_{\mathbf{Q}_1}^y & E_{\mathbf{Q}_1}^x \\ 0 & E_{\mathbf{Q}_1}^x & F_{\mathbf{Q}_1}^z \end{pmatrix}$	4
$P\bar{3}1m$	$\begin{pmatrix} F_{\mathbf{Q}_1}^x & 0 & E_{\mathbf{Q}_1}^y \\ 0 & F_{\mathbf{Q}_1}^y & 0 \\ E_{\mathbf{Q}_1}^y & 0 & F_{\mathbf{Q}_1}^z \end{pmatrix}$	4	$\begin{pmatrix} F_{\mathbf{Q}_1}^x & 0 & E_{\mathbf{Q}_1}^y \\ 0 & F_{\mathbf{Q}_1}^y & 0 \\ E_{\mathbf{Q}_1}^y & 0 & F_{\mathbf{Q}_1}^z \end{pmatrix}$	4
$P321$	$\begin{pmatrix} F_{\mathbf{Q}_1}^x & 0 & 0 \\ 0 & F_{\mathbf{Q}_1}^y & E_{\mathbf{Q}_1}^x + iD_{\mathbf{Q}_1}^x \\ 0 & E_{\mathbf{Q}_1}^x - iD_{\mathbf{Q}_1}^x & F_{\mathbf{Q}_1}^z \end{pmatrix}$	5	$\begin{pmatrix} F_{\mathbf{Q}_1}^x & iD_{\mathbf{Q}_1}^z & -iD_{\mathbf{Q}_1}^y \\ -iD_{\mathbf{Q}_1}^z & F_{\mathbf{Q}_1}^y & E_{\mathbf{Q}_1}^x \\ iD_{\mathbf{Q}_1}^z & E_{\mathbf{Q}_1}^x & F_{\mathbf{Q}_1}^z \end{pmatrix}$	6
$P312$	$\begin{pmatrix} F_{\mathbf{Q}_1}^x & iD_{\mathbf{Q}_1}^z & E_{\mathbf{Q}_1}^y \\ -iD_{\mathbf{Q}_1}^z & F_{\mathbf{Q}_1}^y & iD_{\mathbf{Q}_1}^x \\ E_{\mathbf{Q}_1}^y & -iD_{\mathbf{Q}_1}^x & F_{\mathbf{Q}_1}^z \end{pmatrix}$	6	$\begin{pmatrix} F_{\mathbf{Q}_1}^x & 0 & E_{\mathbf{Q}_1}^y - iD_{\mathbf{Q}_1}^x \\ 0 & F_{\mathbf{Q}_1}^y & 0 \\ E_{\mathbf{Q}_1}^y + iD_{\mathbf{Q}_1}^x & 0 & F_{\mathbf{Q}_1}^z \end{pmatrix}$	5
$P3m1$	$\begin{pmatrix} F_{\mathbf{Q}_1}^x & iD_{\mathbf{Q}_1}^z & -iD_{\mathbf{Q}_1}^y \\ -iD_{\mathbf{Q}_1}^z & F_{\mathbf{Q}_1}^y & E_{\mathbf{Q}_1}^x \\ iD_{\mathbf{Q}_1}^z & E_{\mathbf{Q}_1}^x & F_{\mathbf{Q}_1}^z \end{pmatrix}$	6	$\begin{pmatrix} F_{\mathbf{Q}_1}^x & 0 & 0 \\ 0 & F_{\mathbf{Q}_1}^y & E_{\mathbf{Q}_1}^x + iD_{\mathbf{Q}_1}^x \\ 0 & E_{\mathbf{Q}_1}^x - iD_{\mathbf{Q}_1}^x & F_{\mathbf{Q}_1}^z \end{pmatrix}$	5
$P31m$	$\begin{pmatrix} F_{\mathbf{Q}_1}^x & 0 & E_{\mathbf{Q}_1}^y - iD_{\mathbf{Q}_1}^x \\ 0 & F_{\mathbf{Q}_1}^y & 0 \\ E_{\mathbf{Q}_1}^y + iD_{\mathbf{Q}_1}^x & 0 & F_{\mathbf{Q}_1}^z \end{pmatrix}$	5	$\begin{pmatrix} F_{\mathbf{Q}_1}^x & iD_{\mathbf{Q}_1}^z & E_{\mathbf{Q}_1}^y \\ -iD_{\mathbf{Q}_1}^z & F_{\mathbf{Q}_1}^y & iD_{\mathbf{Q}_1}^x \\ E_{\mathbf{Q}_1}^y & -iD_{\mathbf{Q}_1}^x & F_{\mathbf{Q}_1}^z \end{pmatrix}$	6
$P\bar{3}$	$\begin{pmatrix} F_{\mathbf{Q}_1}^x & E_{\mathbf{Q}_1}^z & E_{\mathbf{Q}_1}^y \\ E_{\mathbf{Q}_1}^z & F_{\mathbf{Q}_1}^y & E_{\mathbf{Q}_1}^x \\ E_{\mathbf{Q}_1}^y & E_{\mathbf{Q}_1}^x & F_{\mathbf{Q}_1}^z \end{pmatrix}$	6	$\begin{pmatrix} F_{\mathbf{Q}_1}^x & E_{\mathbf{Q}_1}^z & E_{\mathbf{Q}_1}^y \\ E_{\mathbf{Q}_1}^z & F_{\mathbf{Q}_1}^y & E_{\mathbf{Q}_1}^x \\ E_{\mathbf{Q}_1}^y & E_{\mathbf{Q}_1}^x & F_{\mathbf{Q}_1}^z \end{pmatrix}$	6
$P3$	$\begin{pmatrix} F_{\mathbf{Q}_1}^x & E_{\mathbf{Q}_1}^z + iD_{\mathbf{Q}_1}^y & E_{\mathbf{Q}_1}^y - iD_{\mathbf{Q}_1}^x \\ E_{\mathbf{Q}_1}^z - iD_{\mathbf{Q}_1}^y & F_{\mathbf{Q}_1}^y & E_{\mathbf{Q}_1}^x + iD_{\mathbf{Q}_1}^x \\ E_{\mathbf{Q}_1}^y + iD_{\mathbf{Q}_1}^x & E_{\mathbf{Q}_1}^x - iD_{\mathbf{Q}_1}^x & F_{\mathbf{Q}_1}^z \end{pmatrix}$	9	$\begin{pmatrix} F_{\mathbf{Q}_1}^x & E_{\mathbf{Q}_1}^z + iD_{\mathbf{Q}_1}^y & E_{\mathbf{Q}_1}^y - iD_{\mathbf{Q}_1}^x \\ E_{\mathbf{Q}_1}^z - iD_{\mathbf{Q}_1}^y & F_{\mathbf{Q}_1}^y & E_{\mathbf{Q}_1}^x + iD_{\mathbf{Q}_1}^x \\ E_{\mathbf{Q}_1}^y + iD_{\mathbf{Q}_1}^x & E_{\mathbf{Q}_1}^x - iD_{\mathbf{Q}_1}^x & F_{\mathbf{Q}_1}^z \end{pmatrix}$	9

$\phi = 2\pi/3$ ($\phi = 4\pi/3$) and $\sigma = 1$. $X_{-\mathbf{Q}}$ is obtained from $X_{-\mathbf{Q}} = X_{\mathbf{Q}}^*$ by the time-reversal symmetry.

Tables V–VII are useful to construct the model not only with $\{\mathbf{Q}\}$ shown in Fig. 2 but also with other $\{\mathbf{Q}\}$. For example, the model with $\{\mathbf{Q}\} = \{\pm\mathbf{Q}_1 \parallel \hat{x}, \pm\mathbf{Q}_2 \parallel \hat{y}, \mathbf{Q}_1 \pm \mathbf{Q}_2, -\mathbf{Q}_1 \pm \mathbf{Q}_2\}$ in $P4/mmm$ crystal is constructed from $X_{\mathbf{Q}_1 \parallel \hat{x}}$ and $X_{(\mathbf{Q}_1 + \mathbf{Q}_2) \parallel [110]}$, which are given in Table V. Then, the number of independent interactions in the model is six. Furthermore, the general model in Eq. (9) with the interactions at the two-dimensional wave vectors can be constructed from Tables V–VII and Appendix B, which will give an insight into the stability of the two-dimensional multiple- \mathbf{Q} states, such as the SkX. Similar to the case with two-dimensional wave vectors, one can construct the spin model with the interactions at three-dimensional wave vectors based on the rules (a)–(f), which leads to a minimal effective spin model to investigate an instability toward three-dimensional multiple- \mathbf{Q} states [42,46,108,114], such as the hedgehog lattice.

Although one can start from the general model in Eq. (9) and obtain the optimal spin configurations by performing unbiased numerical simulations, such as Monte Carlo simulations, one notices that the effective spin model in Eq. (10) is enough to discuss the magnetic instability in specific temperature regions. For example, in the case of the isotropic classical spin model, which corresponds to $F_q^x = F_q^y = F_q^z$ and

$\mathbf{D}_q = \mathbf{E}_q = 0$, the ground state becomes the spiral ordering with the wave vector \mathbf{q}^* that gives the largest value of $X_{\mathbf{q}}$. In this case, the interactions with other $\mathbf{q} (\neq \mathbf{q}^*)$ do not contribute to the energy, which can be neglected. Meanwhile, in the case of the anisotropic spin model originating from the SOC, the instability toward a multiple- \mathbf{Q} state, which is a superposition of spin density waves at different \mathbf{q} , can occur. In such a situation, the superposition between the wave vectors connected by the point-group operations tends to be favored, since they give the same largest eigenvalue of $X_{\mathbf{q}}$ so as to satisfy the lattice symmetry. Then, it is natural to use the effective spin model in Eq. (10) rather than the general model in Eq. (9) to examine the low-temperature spin configuration. The use of the effective spin model enables us to reduce the computational cost. Furthermore, the effective spin model is useful to discuss the instability toward the multiple- \mathbf{Q} states in the model with the dipolar interaction at high temperatures [53,69].

The momentum-space effective spin model in Eqs. (9) and (10) can be applied to both metals with long-range interactions and insulators with short-range interactions. Especially, when considering the low-temperature spin configuration in metals, the effective spin model in momentum space in Eq. (10) enables us to search for multiple- \mathbf{Q} states more efficiently compared to the original itinerant electron model in real space. In the momentum-space effective spin model, there are only

three to nine model parameters depending on the wave vector. Meanwhile, when we construct an effective spin model with the real-space interactions for the itinerant electron model, the consideration up to the further-neighbor interactions including the sign change is required. Besides, too many model parameters make it difficult to obtain the optimal spin configurations with the lowest energy, since there are a lot of local minima due to the competing interactions in real space. Thus, our effective spin model in Eq. (10) gives an efficient guideline to understand the instability toward the multiple- Q states.

We comment that the effective spin models in the primitive-lattice system in Eq. (10) can be used as the effective spin model in the multisublattice systems when the ordering vectors in each sublattice are common to each other. Indeed, the effective spin models based on such an approximation have accounted for the appearance of the SkX [96,103,108,111], hedgehog-lattice [42], and vortex-crystal [95] phases in real materials where there are multiple magnetic ions in the unit cell. Meanwhile, in order to examine the magnetic structures within the unit cell, we need to extend the effective spin models so as to include the sublattice degree of freedom, as discussed in the next section.

Finally, we briefly discuss how to construct the model from the experimental data, where we focus on GdRu_2Si_2 [18,103]. GdRu_2Si_2 has a $I4/mmm$ crystal structure with the alternative stacking of the Gd square lattice and hosts the incommensurate order below a Néel temperature with the ordering vector $\mathbf{Q} \parallel [100]$. By applying the magnetic field along the $[001]$ direction, the double- Q SkX with ordering vectors $\mathbf{Q}_1 = (Q, 0, 0)$ and $\mathbf{Q}_2 = (0, Q, 0)$ appears in the ground state, where \mathbf{Q}_1 and \mathbf{Q}_2 are connected by the fourfold rotation along $[001]$. Thus, we approximate the $I4/mmm$ crystal structure by the Gd square lattice with $P4/mmm$ symmetry and take into account the interactions only at $\pm\mathbf{Q}_1$ and $\pm\mathbf{Q}_2$. Such a situation is described by the model in Eq. (10) with $P4/mmm$ symmetry and $\{\mathbf{Q}\} = \{\pm\mathbf{Q}_1, \pm\mathbf{Q}_2\}$, which is constructed from Table V and Eqs. (11) and (12): $X_{\mathbf{Q}_1 \parallel \hat{x}}$ is shown in the first row of Table V, and $X_{\mathbf{Q}_2}$ are obtained by using Eq. (12) with $\sigma = 1$ and $\phi = \pi/2$. Indeed, this model reproduces not only the observed SkX phase but also the other double- Q phases appearing at low temperatures by additionally considering the magnetic field and biquadratic interaction [103]. In this way, one can construct the effective spin model for other materials once the space-group symmetry and relevant $\{\mathbf{Q}\}$ are determined from the x-ray and neutron experiments.

2. Multisublattice case

Based on the symmetry argument in Sec. II A 2, one can directly construct the effective spin model in two and three sublattice systems. The effective spin Hamiltonian is given by

$$\mathcal{H}^{\text{eff}} = - \sum_{\mathbf{q} \in \{\mathbf{Q}\}} \sum_{\mu, \nu} \mathbf{S}_{\mu\mathbf{q}}^T \mathcal{X}_{\mu\nu;\mathbf{q}} \mathbf{S}_{\nu-\mathbf{q}}, \quad (13)$$

where $\{\mathbf{Q}\}$ is a set of the wave vector. As in the primitive-lattice case, we can write down nonzero components of the interaction matrix once $\{\mathbf{Q}\}$ and the space group are given. As specific examples, we present the interaction matrix at $\mathbf{Q}_1 \parallel \hat{x}$ in the honeycomb and kagome structures with the hexagonal space group $P6/mmm$ shown in Fig. 3; the Brillouin zone

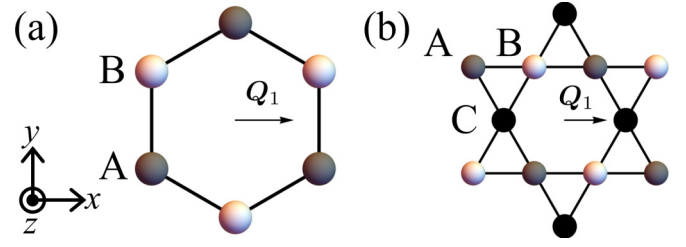


FIG. 3. (a) Honeycomb and (b) kagome structures with $P6/mmm$ symmetry. Gray, white, and black spheres represent sublattices A, B, and C, respectively. The wave vector \mathbf{Q}_1 parallel to the x direction is denoted in the figure.

is the same as that in Fig. 2(c). When focusing on the \mathbf{Q}_1 component, there are seven symmetry constraints in both honeycomb and kagome lattices similar to the primitive triangular lattice as follows: the inversion center (I); the mirror planes perpendicular to \hat{x} (m_x), \hat{y} (m_y), and \hat{z} (m_z); and the twofold axis parallel to \hat{x} (C_x), \hat{y} (C_y), and \hat{z} (C_z). Depending on the sublattice configurations, these constraints give different interaction matrices, as detailed below.

In the two-sublattice honeycomb-structure case in Fig. 3(a), m_z , m_x , and C_y (I , m_y , C_x , and C_z) fix (interchange) the sublattices A and B. The symmetry constraints by m_z , m_x , and C_y (I , m_y , C_x , and C_z) are given in Fig. 1 and Table I (Tables II and III). Consequently, the interaction matrices are expressed as

$$\mathcal{X}_{AA;\mathbf{Q}_1} = \begin{pmatrix} \text{Re}(\mathcal{F}_{AA;\mathbf{Q}_1}^x) & i\text{Im}(\mathcal{D}_{AA;\mathbf{Q}_1}^z) & 0 \\ -i\text{Im}(\mathcal{D}_{AA;\mathbf{Q}_1}^z) & \text{Re}(\mathcal{F}_{AA;\mathbf{Q}_1}^y) & 0 \\ 0 & 0 & \text{Re}(\mathcal{F}_{AA;\mathbf{Q}_1}^z) \end{pmatrix}, \quad (14)$$

$$\mathcal{X}_{BB;\mathbf{Q}_1} = \begin{pmatrix} \text{Re}(\mathcal{F}_{AA;\mathbf{Q}_1}^x) & -i\text{Im}(\mathcal{D}_{AA;\mathbf{Q}_1}^z) & 0 \\ i\text{Im}(\mathcal{D}_{AA;\mathbf{Q}_1}^z) & \text{Re}(\mathcal{F}_{AA;\mathbf{Q}_1}^y) & 0 \\ 0 & 0 & \text{Re}(\mathcal{F}_{AA;\mathbf{Q}_1}^z) \end{pmatrix}, \quad (15)$$

$$\mathcal{X}_{AB;\mathbf{Q}_1} = \begin{pmatrix} \text{Re}(\mathcal{F}_{AB;\mathbf{Q}_1}^x) & i\text{Im}(\mathcal{E}_{AB;\mathbf{Q}_1}^z) & 0 \\ i\text{Im}(\mathcal{E}_{AB;\mathbf{Q}_1}^z) & \text{Re}(\mathcal{F}_{AB;\mathbf{Q}_1}^y) & 0 \\ 0 & 0 & \text{Re}(\mathcal{F}_{AB;\mathbf{Q}_1}^z) \end{pmatrix}. \quad (16)$$

Here, $\mathcal{X}_{BB;\mathbf{Q}_1}$ is related to $\mathcal{X}_{AA;\mathbf{Q}_1}$ through I , m_y , C_x , and C_z . Compared to $\mathcal{X}_{\mathbf{Q}_1 \parallel \hat{x}}$ on $P6/mmm$ triangular lattice shown in Table VI, the main difference is seen in the off-diagonal components in $\mathcal{X}_{AA;\mathbf{Q}_1}$ and $\mathcal{X}_{BB;\mathbf{Q}_1}$; the intrasublattice DM interaction $\text{Im}(\mathcal{D}_{AA;\mathbf{Q}_1}^z)$ arises in the honeycomb structure due to the lack of the local inversion symmetry at each sublattice. Meanwhile, the intersublattice interaction $\mathcal{X}_{AB;\mathbf{Q}_1}$ has a symmetric anisotropic exchange interaction $\text{Im}(\mathcal{E}_{AB;\mathbf{Q}_1}^z)$ rather than the DM interaction. The interaction matrices at the other \mathbf{Q}_η are easily obtained from a similar relation in Eq. (11).

In the three-sublattice kagome-structure case in Fig. 3(b), I , m_z , and C_z fix the sublattices A, B, and C, while m_x , m_y , C_x , and C_y interchange the sublattices A and B but fix C. Thus, the symmetry constraints by the former (latter) symmetries are given in Fig. 1 and Table I (Fig. 1 and Tables II–IV). As a

result, the interaction matrices are given by

$$\mathcal{X}_{AA;\mathbf{Q}_1} = \begin{pmatrix} \text{Re}(\mathcal{F}_{AA;\mathbf{Q}_1}^x) & \text{Re}(\mathcal{E}_{AA;\mathbf{Q}_1}^z) & 0 \\ \text{Re}(\mathcal{E}_{AA;\mathbf{Q}_1}^z) & \text{Re}(\mathcal{F}_{AA;\mathbf{Q}_1}^y) & 0 \\ 0 & 0 & \text{Re}(\mathcal{F}_{AA;\mathbf{Q}_1}^z) \end{pmatrix}, \quad \mathcal{X}_{BB;\mathbf{Q}_1} = \begin{pmatrix} \text{Re}(\mathcal{F}_{AA;\mathbf{Q}_1}^x) & -\text{Re}(\mathcal{E}_{AA;\mathbf{Q}_1}^z) & 0 \\ -\text{Re}(\mathcal{E}_{AA;\mathbf{Q}_1}^z) & \text{Re}(\mathcal{F}_{AA;\mathbf{Q}_1}^y) & 0 \\ 0 & 0 & \text{Re}(\mathcal{F}_{AA;\mathbf{Q}_1}^z) \end{pmatrix}, \quad (17)$$

$$\mathcal{X}_{CC;\mathbf{Q}_1} = \begin{pmatrix} \text{Re}(\mathcal{F}_{CC;\mathbf{Q}_1}^x) & 0 & 0 \\ 0 & \text{Re}(\mathcal{F}_{CC;\mathbf{Q}_1}^y) & 0 \\ 0 & 0 & \text{Re}(\mathcal{F}_{CC;\mathbf{Q}_1}^z) \end{pmatrix}, \quad \mathcal{X}_{AB;\mathbf{Q}_1} = \begin{pmatrix} \text{Re}(\mathcal{F}_{AB;\mathbf{Q}_1}^x) & \text{Re}(\mathcal{D}_{AB;\mathbf{Q}_1}^z) & 0 \\ -\text{Re}(\mathcal{D}_{AB;\mathbf{Q}_1}^z) & \text{Re}(\mathcal{F}_{AB;\mathbf{Q}_1}^y) & 0 \\ 0 & 0 & \text{Re}(\mathcal{F}_{AB;\mathbf{Q}_1}^z) \end{pmatrix}, \quad (18)$$

$$\mathcal{X}_{BC;\mathbf{Q}_1} = \begin{pmatrix} \text{Re}(\mathcal{F}_{BC;\mathbf{Q}_1}^x) & \text{Re}(\mathcal{E}_{BC;\mathbf{Q}_1}^z) + \text{Re}(\mathcal{D}_{BC;\mathbf{Q}_1}^z) & 0 \\ \text{Re}(\mathcal{E}_{BC;\mathbf{Q}_1}^z) - \text{Re}(\mathcal{D}_{BC;\mathbf{Q}_1}^z) & \text{Re}(\mathcal{F}_{BC;\mathbf{Q}_1}^y) & 0 \\ 0 & 0 & \text{Re}(\mathcal{F}_{BC;\mathbf{Q}_1}^z) \end{pmatrix}, \quad (19)$$

$$\mathcal{X}_{CA;\mathbf{Q}_1} = \begin{pmatrix} \text{Re}(\mathcal{F}_{BC;\mathbf{Q}_1}^x) & -\text{Re}(\mathcal{E}_{BC;\mathbf{Q}_1}^z) + \text{Re}(\mathcal{D}_{BC;\mathbf{Q}_1}^z) & 0 \\ -\text{Re}(\mathcal{E}_{BC;\mathbf{Q}_1}^z) - \text{Re}(\mathcal{D}_{BC;\mathbf{Q}_1}^z) & \text{Re}(\mathcal{F}_{BC;\mathbf{Q}_1}^y) & 0 \\ 0 & 0 & \text{Re}(\mathcal{F}_{BC;\mathbf{Q}_1}^z) \end{pmatrix}. \quad (20)$$

Since the sublattice C is fixed by all the point-group symmetries, $\mathcal{X}_{AA;\mathbf{Q}_1}$ and $\mathcal{X}_{BB;\mathbf{Q}_1}$ ($\mathcal{X}_{BC;\mathbf{Q}_1}$ and $\mathcal{X}_{CA;\mathbf{Q}_1}$) depend on each other, while $\mathcal{X}_{CC;\mathbf{Q}_1}$ ($\mathcal{X}_{AB;\mathbf{Q}_1}$) is independent. Similar to the honeycomb-structure case, the DM interaction arises in the kagome-structure case, although their natures are different from each other due to the different sublattice configurations: The DM interaction appears in the intersublattice interaction $\mathcal{X}_{\mu\nu;\mathbf{Q}_1}$ in the kagome-structure case, while it appears in the intrasublattice interaction $\mathcal{X}_{\mu\mu;\mathbf{Q}_1}$ in the honeycomb-structure case. The interaction matrices at the other \mathbf{Q}_η are also obtained from a similar relation in Eq. (11).

The effective spin model in Eq. (13) becomes a reference to search for sublattice-dependent multiple- Q states, such as the antiferromagnetic SkX [63–65] and multisublattice SkX [66]. As $\text{Re}(\mathcal{D}_{\mu\mu;\mathbf{q}})$, $\text{Im}(\mathcal{E}_{\mu\mu;\mathbf{q}})$, $\text{Im}(\mathcal{F}_{\mu\mu;\mathbf{q}})$ in the intrasublattice interaction matrix $\mathcal{X}_{\mu\mu;\mathbf{Q}_1}$, and $\mathcal{D}_{\mu\nu;\mathbf{q}}$, $\mathcal{E}_{\mu\nu;\mathbf{q}}$, and $\mathcal{F}_{\mu\nu;\mathbf{q}}$ in the intersublattice interaction matrix $\mathcal{X}_{\mu\nu;\mathbf{Q}_1}$ ($\mu \neq \nu$) additionally emerge according to the multisublattice configurations, they can become different sources to induce the multiple- Q states in the multisublattice system. Besides, the model in Eq. (13) is useful to provide insight into the microscopic origin of the sublattice-dependent topological spin textures observed in experiments, such as the fractional antiferromagnetic SkX in MnSc_2S_4 [115,116].

C. Tendency of spin configurations under the anisotropic interactions

In Secs. II A and II B, we show that a variety of anisotropic exchange interactions appear depending on the space group, wave vector, and sublattice structure. To intuitively understand the relationship between the momentum-resolved anisotropic exchange interactions and the multiple- Q states, we present plausible spin configurations in the presence of each $\mathbf{D}_{\mathbf{Q}_\eta}$, $\mathbf{E}_{\mathbf{Q}_\eta}$, and $\mathbf{F}_{\mathbf{Q}_\eta}$ in the primitive triangular-lattice case under the hexagonal and trigonal space groups. Figure 4 shows the expected single- Q and triple- Q modulations under the strong anisotropic interactions, as detailed in Secs. II C 1 and II C 2, respectively. Although we present here the spin configurations for the variable spin length due to quantum and thermal fluctuations for better visibility, similar single- Q and

triple- Q spin configurations are also obtained as the ground state even in the classical spin model by taking into account the anisotropic exchange interaction.

1. Single- Q case

We discuss the tendency of single- Q instabilities under the momentum-resolved interaction at the wave vector $\mathbf{Q}_1 \parallel \hat{x}$. In the case of the isotropic interaction, the spiral state with a wave vector $\mathbf{q}^* = \mathbf{Q}_1$ has the lowest energy, as described above, where the spiral plane is arbitrary. When additionally considering the anisotropic interactions, the spiral wave is modulated depending on the type of interaction. For example, $\mathbf{D}_{\mathbf{Q}_1}$ fixes the spiral plane perpendicular to $\mathbf{D}_{\mathbf{Q}_1}$: The proper-screw (out-of-plane cycloidal) spiral wave is favored in the space group $P622$ ($P6mm$) with nonzero $D_{\mathbf{Q}_1}^x$ ($D_{\mathbf{Q}_1}^y$), and the in-plane cycloidal spiral wave is favored in the space group $P\bar{6}m2$ with nonzero $D_{\mathbf{Q}_1}^z$. The proper-screw, out-of-plane cycloidal, and in-plane cycloidal spiral waves are shown in the upper panels of Figs. 4(a)–4(c), respectively. Meanwhile, when considering the effect of $\mathbf{E}_{\mathbf{Q}_1}$ instead of $\mathbf{D}_{\mathbf{Q}_1}$, the spiral plane by the isotropic interaction is elliptically modulated so as to have a more perpendicular spin component to $\mathbf{E}_{\mathbf{Q}_1}$. In other words, $\mathbf{E}_{\mathbf{Q}_1}$ favors the sinusoidal wave oscillating in one direction. For example, $E_{\mathbf{Q}_1}^x$, $E_{\mathbf{Q}_1}^y$, and $E_{\mathbf{Q}_1}^z$ favor the sinusoidal wave with the spin oscillation along the $[011]$, $[101]$, and $[110]$ directions in spin space, respectively, which are shown in the upper panels of Figs. 4(d)–4(f). It is noted that a similar sinusoidal spin configuration with a constant $|S_i|$ is expected to appear in the classical spin model. Such a sinusoidal modulation by $E_{\mathbf{Q}_1}^x$, $E_{\mathbf{Q}_1}^y$, and $E_{\mathbf{Q}_1}^z$ is expected in the space groups $P\bar{3}m1$, $P\bar{3}1m$, and $P6/m$, respectively. Moreover, $\mathbf{F}_{\mathbf{Q}_1}$ also modulates the spiral wave into the sinusoidal wave. For example, in the case of $F_{\mathbf{Q}_1}^x$, $F_{\mathbf{Q}_1}^y$, and $F_{\mathbf{Q}_1}^z$, the sinusoidal wave with the spin oscillation along the $[100]$, $[010]$, and $[001]$ directions in spin space is favored, respectively, as shown in the upper panel of Figs. 4(g)–4(i).

2. Triple- Q case

Similar to the single- Q case, one can expect a tendency of the multiple- Q spin configuration under the strong anisotropic

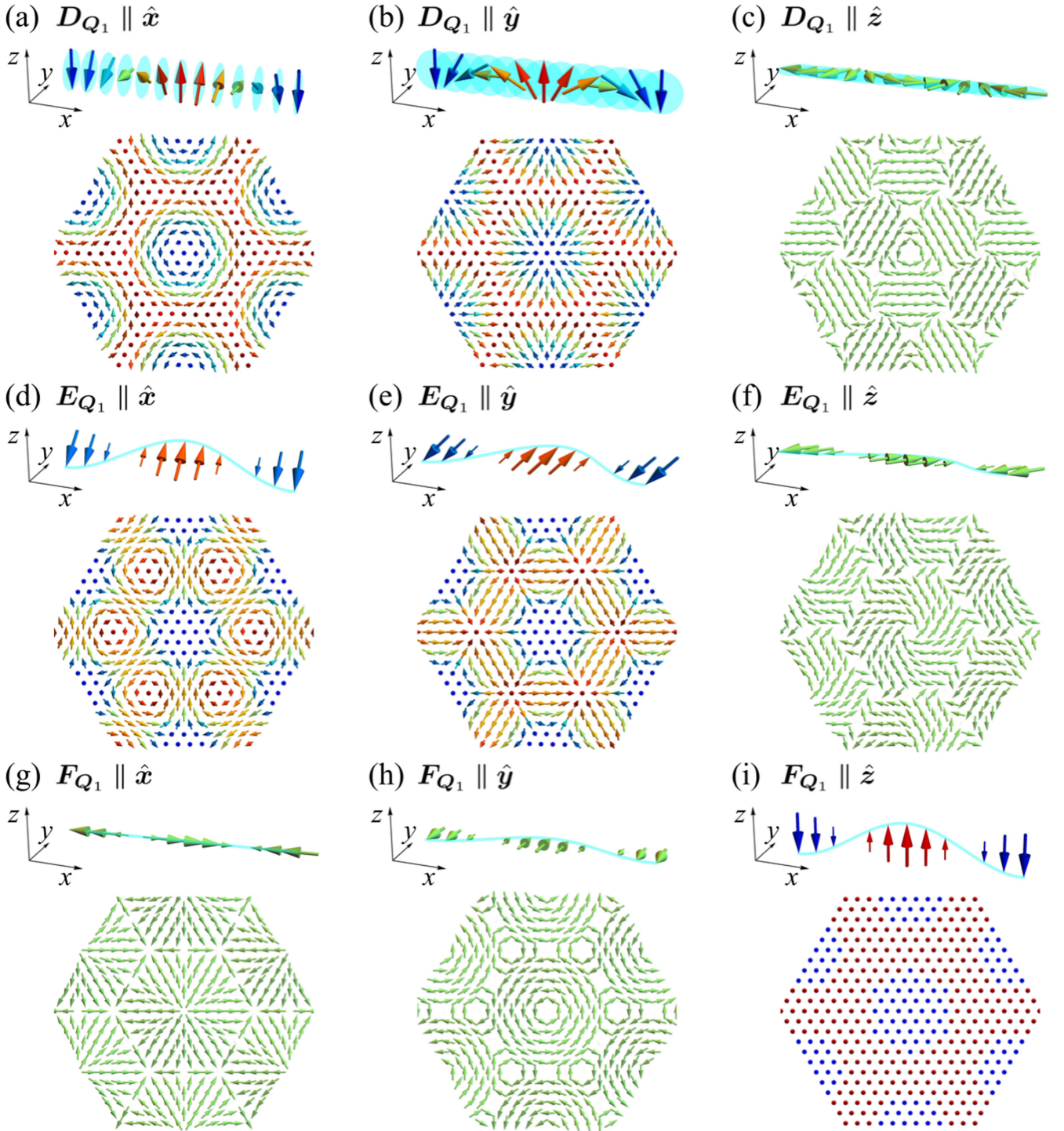


FIG. 4. Spin configurations in the presence of the anisotropic interactions: (a) $D_{Q_1} \parallel \hat{x}$, (b) $D_{Q_1} \parallel \hat{y}$, (c) $D_{Q_1} \parallel \hat{z}$, (d) $E_{Q_1} \parallel \hat{x}$, (e) $E_{Q_1} \parallel \hat{y}$, (f) $E_{Q_1} \parallel \hat{z}$, (g) $F_{Q_1} \parallel \hat{x}$, (h) $F_{Q_1} \parallel \hat{y}$, and (i) $F_{Q_1} \parallel \hat{z}$. Upper panel: Single- Q spin structures with the ordering vector $Q_1 \parallel \hat{x}$ of (a)–(c) spiral waves and (d)–(i) sinusoidal waves. In (a)–(c), the spiral planes in the spiral wave are (a) yz , (b) zx , and (c) xy planes. In (d)–(i), the oscillating directions in the sinusoidal wave are (d) $[011]$, (e) $[101]$, (f) $[110]$, (g) $[100]$, (h) $[010]$, and (i) $[001]$ directions. Lower panel: Triple- Q structures consisting of the three single- Q waves in the upper panel at Q_1 , Q_2 , and Q_3 in Fig. 2(c). The colors of the arrows represent the z spin component, where red, blue, and green denote positive, negative, and zero values. When the spin length at each site is fixed, these spin configurations are modulated by the constraint in terms of the spin norm.

interactions. We discuss here the relationship between the anisotropic interactions and the triple- Q spin configuration by superposing the three spirals with the same intensity on the triangular lattice belonging to the hexagonal and trigonal

space groups, where we consider the superposition of the spin density waves at Q_1 , Q_2 , and Q_3 in Fig. 2(c) and neglect the phase degree of freedom of the spin density wave for simplicity [62,117,118].

In the case of $\mathbf{D}_{Q_1} \parallel \hat{x}$, i.e., $\mathbf{D}_{Q_1} \parallel \mathbf{Q}_1$, the threefold rotational symmetry imposes $\mathbf{D}_{Q_2} \parallel \mathbf{Q}_2$ and $\mathbf{D}_{Q_3} \parallel \mathbf{Q}_3$. Then, $\mathbf{D}_{Q_1} \parallel \hat{x}$ favors the triple- Q proper-screw spiral wave expressed as the superposition of the three proper-screw spirals in the lower panel of Fig. 4(a), which corresponds to the Bloch SkX with $N_{\text{sk}} = -1$ per magnetic unit cell [see Eq. (57) for the definition of the skyrmion number N_{sk} in Sec. V C]. Similarly, $\mathbf{D}_{Q_1} \parallel \hat{y}$ and $\mathbf{D}_{Q_1} \parallel \hat{z}$ favor the triple- Q out-of-plane cycloidal spiral wave corresponding to the Néel SkX with $N_{\text{sk}} = -1$ and the triple- Q in-plane spiral wave, as shown in the lower panel of Figs. 4(b) and 4(c), respectively. As shown in Figs. 4(a) and 4(b) [Fig. 4(c)], the superposition of spirals in different spiral planes (the same spiral plane) leads to the noncoplanar (coplanar) structure.

Meanwhile, \mathbf{E}_{Q_1} and \mathbf{F}_{Q_1} tend to favor triple- Q sinusoidal waves, as shown in the lower panel of Figs. 4(d)–4(i). Among them, $\mathbf{E}_{Q_1} \parallel \hat{x}$ and $\mathbf{E}_{Q_1} \parallel \hat{y}$ tend to favor the noncoplanar triple- Q sinusoidal waves since they consist of the three sinusoidal waves oscillating in different out-of-plane directions, as shown in the lower panel of Figs. 4(d) and 4(e). These noncoplanar triple- Q sinusoidal states correspond to the SkXs with $N_{\text{sk}} = +2$. The cases for $\mathbf{E}_{Q_1} \parallel \hat{z}$, $\mathbf{F}_{Q_1} \parallel \hat{x}$, and $\mathbf{F}_{Q_1} \parallel \hat{y}$ favor the coplanar triple- Q sinusoidal waves consisting of the three sinusoidal waves oscillating in different in-plane directions, as shown in the lower panel of Figs. 4(f)–4(h). The remaining $\mathbf{F}_{Q_1} \parallel \hat{z}$ favors the collinear triple- Q sinusoidal wave consisting of the three sinusoidal waves oscillating in the same direction [the lower panel of Fig. 4(i)], which is the so-called magnetic bubble.

The above intuitive analysis provides two important pieces of information about the SkXs. The first is that the anisotropic interactions in all the hexagonal and trigonal crystal systems do not tend to favor the antitype SkXs with $N_{\text{sk}} = +1$ without the threefold rotational symmetry, since the anisotropic exchange interactions connected by the threefold rotation [see Eq. (11)] lead to the energy loss to form such SkXs free from threefold symmetry. Meanwhile, there is no preference between the SkXs and antitype SkXs in terms of the symmetric anisotropic exchange interactions in the tetragonal crystal systems. The second is that there is an instability tendency toward the SkXs with $|N_{\text{sk}}| = 2$ only in the trigonal crystal systems with $\mathbf{E}_{Q_1}^x$ and $\mathbf{E}_{Q_1}^y$ within the bilinear exchange interactions.

Such an argument in terms of the spin modulations under the anisotropic exchange interactions is consistent with the previous studies for the effective spin model with the classical spin, where unbiased numerical simulations have been performed at low temperatures close to the zero temperature under the space groups $P4/mmm$ [51,92], $P4mm$ [49], $P4/m$ [119], $P6/mmm$ [54,94], $P6mm$ [55], $P6m2$ [120], and $P\bar{3}m1$ [61]. For example, the $P\bar{3}m1$ system with nonzero $\mathbf{E}_{Q_1}^x$ in addition to the isotropic exchange interaction exhibits the instability toward the SkX with $|N_{\text{sk}}| = 2$ in Fig. 4(d). According to the simulation, the plausible multiple- Q state can be energetically stable even by small magnetic anisotropy; the SkX with $|N_{\text{sk}}| = 2$ in Fig. 4(d) is stabilized by $\mathbf{E}_{Q_1}^x$, whose magnitude is 10 times smaller than that of the isotropic interaction [61]. For another example, the $P6/mmm$ system with nonzero $\mathbf{F}_{Q_1}^x$ ($\mathbf{F}_{Q_1}^y$) in addition to the isotropic exchange interaction and Zeeman coupling to an external magnetic field

leads to the SkX with $N_{\text{sk}} = -1$, whose spin configuration is similar to that in Fig. 4(b) [4(a)]. Furthermore, the skyrmion texture of the quantum spin has been studied in the quantum spin state, where the Néel-type skyrmion appears by $\mathbf{D}_{Q_1} \parallel \hat{y}$ even under quantum fluctuations [121–123].

III. ORIGIN OF THE ANISOTROPIC EXCHANGE INTERACTIONS: CASE OF ITINERANT ELECTRON MODELS

We discuss how to derive the momentum-resolved anisotropic exchange interaction in Eq. (9) based on a microscopic Hamiltonian for itinerant magnets. Starting from the multiband anisotropic PAM with the SOC in Sec. III A, we present the important parameters for nonzero anisotropic interactions. For that purpose, we perform the Schrieffer-Wolff transformation [99] to derive the Kondo lattice model with the anisotropic exchange coupling between itinerant electron spins and localized spins in Sec. III B. Then, we trace out the itinerant electron degree of freedom to derive the effective spin model by supposing the weak exchange coupling in Sec. III C.

A. Anisotropic periodic Anderson model

We consider the multiband anisotropic PAM incorporating the effect of the SOC [61,101,124,125], which is represented by

$$\mathcal{H}^{\text{PAM}} = \mathcal{H}^c + \mathcal{H}^f + \mathcal{H}^{cf}, \quad (21)$$

where

$$\mathcal{H}^c = \sum_{m,\mathbf{k},\sigma} (\varepsilon_{m\mathbf{k}} - \mu) c_{m\mathbf{k}\sigma}^\dagger c_{m\mathbf{k}\sigma}, \quad (22)$$

$$\mathcal{H}^f = (E_f - \mu) \sum_{i,\sigma} n_{i\sigma} + U \sum_i n_{i\uparrow} n_{i\downarrow}, \quad (23)$$

$$\mathcal{H}^{cf} = \sum_{m,i,\mathbf{k},\sigma,\sigma'} \frac{e^{i\mathbf{k} \cdot \mathbf{R}_i}}{\sqrt{N}} f_{i\sigma}^\dagger (V_{m\mathbf{k}}^0 \delta + \mathbf{V}_{m\mathbf{k}} \cdot \boldsymbol{\sigma})_{\sigma\sigma'} c_{m\mathbf{k}\sigma'} + \text{H.c.} \quad (24)$$

Here, $c_{m\mathbf{k}\sigma}^\dagger$ ($c_{m\mathbf{k}\sigma}$) is a creation (annihilation) operator of an itinerant electron with band m , wave vector \mathbf{k} , and spin σ , $f_{i\sigma}^\dagger$ ($f_{i\sigma}$) is a creation (annihilation) operator of a localized f electron at position vector \mathbf{R}_i with spin σ , and $n_{i\sigma} = f_{i\sigma}^\dagger f_{i\sigma}$. \mathcal{H}^c represents the Hamiltonian of the itinerant electron with the energy dispersion $\varepsilon_{m\mathbf{k}}$ and the chemical potential μ . \mathcal{H}^f represents the Hamiltonian of the localized f electron, where E_f is the atomic energy and U is the Coulomb interaction. \mathcal{H}_{cf} stands for the Hamiltonian consisting of the hybridization between the itinerant electrons and localized electrons; $V_{m\mathbf{k}}^0 \delta_{\sigma\sigma'}$ represents the spin-independent hybridization, and $\mathbf{V}_{m\mathbf{k}} \cdot \boldsymbol{\sigma}_{\sigma\sigma'} = \sum_{\alpha=x,y,z} V_{m\mathbf{k}}^\alpha \sigma_{\sigma\sigma'}^\alpha$ represents the spin-dependent hybridization, where $\delta_{\sigma\sigma'}$ is the Kronecker delta, $\boldsymbol{\sigma}_{\sigma\sigma'} = (\sigma^x, \sigma^y, \sigma^z)_{\sigma\sigma'}$ is a vector of the Pauli matrices, and N is the number of unit cells. The contribution of spin-dependent hybridization arises from the mixture of up- and down-spin basis functions of the itinerant and/or localized electrons due to the SOC, where the spin index σ in the spin-orbital-coupled basis is regarded as the pseudospin.

B. Anisotropic Kondo lattice model

We derive a low-energy effective model when E_f ($E_f + U$) is much smaller (larger) than the Fermi energy. In this situation, the f electron state at each site is occupied by a single electron ($\sum_{\sigma} n_{i\sigma} = 1$) and the f electron is approximately regarded as the localized spin. When the hybridizations are treated as the perturbation, the low-energy effective model is derived by the Schrieffer-Wolff transformation as $e^{\mathcal{S}} \mathcal{H}^{\text{PAM}} e^{-\mathcal{S}}$ with the generator \mathcal{S} ; \mathcal{S} satisfies $\mathcal{H}^{cf} + [\mathcal{S}, \mathcal{H}^0] = 0$, where $\mathcal{H}^0 = \mathcal{H}^c + \mathcal{H}^f$ and $[\mathcal{S}, \mathcal{H}^0]$ represents the commutation relation. Then, \mathcal{S} is given by

$$\mathcal{S} = \frac{1}{\sqrt{N}} \sum_{m,i,k,\sigma,\sigma'} (A_{mk} + B_{mk} n_{i\bar{\sigma}}) \times \{e^{ik \cdot R_i} f_{i\sigma}^{\dagger} (V_{mk}^0 \delta_{\sigma\sigma'} + \mathbf{V}_{mk} \cdot \boldsymbol{\sigma}_{\sigma\sigma'}) c_{mk\sigma'} - \text{H.c.}\}, \quad (25)$$

where $\bar{\sigma} = -\sigma$ and

$$A_{mk} = \frac{1}{E_f - \varepsilon_{mk}}, \quad (26)$$

$$B_{mk} = \frac{1}{\varepsilon_{mk} - E_f} - \frac{1}{\varepsilon_{mk} - E_f - U}. \quad (27)$$

Then, the low-energy effective model up to the second order of the hybridizations, $\mathcal{H}^{\text{PAM}(2)}$, is approximately given by

$$\mathcal{H}^{\text{PAM}(2)} = \mathcal{H}^0 + \frac{1}{2} [\mathcal{S}, \mathcal{H}^{cf}] \quad (28)$$

$$= \mathcal{H}^c + \sum_{m,m'} \sum_{\sigma,\sigma'} (\mathcal{H}'_{m\sigma,m'\sigma'} \delta_{\sigma\sigma'} + \mathcal{H}^{\text{ex}}_{m\sigma,m'\sigma'} + \mathcal{H}^{\text{SOC}}_{m\sigma,m'\sigma'}), \quad (29)$$

where the subscript $m\sigma; m'\sigma'$ represents a matrix element between itinerant electrons with (m, σ) and (m', σ') . In the derivation, we drop the constant terms such as \mathcal{H}^f . The details of $\mathcal{H}^{\text{PAM}(2)}$ are given in Appendix C.

To focus on the origin of the anisotropic interactions, we further neglect the contributions from the spin-independent term \mathcal{H}' and from the different bands in \mathcal{H}^{ex} and \mathcal{H}^{SOC} . In the end, $\mathcal{H}^{\text{PAM}(2)}$ reduces to an anisotropic Kondo lattice model as

$$\mathcal{H}^{\text{KLM}} = \mathcal{H}^c + \sum_m \sum_{\sigma,\sigma'} (\mathcal{H}^{\text{ex}}_{m\sigma\sigma'} + \mathcal{H}^{\text{SOC}}_{m\sigma\sigma'}), \quad (30)$$

where the subscript $m\sigma\sigma'$ represents a matrix element between itinerant electrons with (m, σ) and (m, σ') .

The Kondo lattice model includes two spin-dependent terms. One is the exchange interaction between itinerant electron spins and localized spins, $\mathcal{H}^{\text{ex}}_{m\sigma\sigma'}$, which is given by

$$\mathcal{H}^{\text{ex}}_{m\sigma\sigma'} = \frac{1}{\sqrt{N}} \sum_{\mathbf{k}, \mathbf{q}, \alpha, \beta} J^{\alpha\beta}_{m\mathbf{k}+\mathbf{q}\mathbf{k}} c_{m\mathbf{k}+\mathbf{q}\sigma}^{\dagger} \sigma_{\sigma\sigma'}^{\alpha} c_{m\mathbf{k}\sigma'} S_{\mathbf{q}}^{\beta}. \quad (31)$$

Here, $S_{\mathbf{q}}$ is the Fourier transform of the localized spin $S_i = \sum_{\sigma,\sigma'} f_{i\sigma}^{\dagger} \boldsymbol{\sigma}_{\sigma\sigma'} f_{i\sigma'}/2$. The exchange interaction is decomposed into isotropic, symmetric anisotropic, and antisymmetric anisotropic exchange interactions in spin space [61,101,126] as

$$J^{\alpha\beta}_{m\mathbf{k}\mathbf{k}'} = J^{\text{ISO}}_{m\mathbf{k}\mathbf{k}'} \delta_{\alpha\beta} + [J^{\text{S}}_{m\mathbf{k}\mathbf{k}'}]^{\alpha\beta} + [J^{\text{AS}}_{m\mathbf{k}\mathbf{k}'}]^{\alpha\beta}, \quad (32)$$

where

$$J^{\text{ISO}}_{m\mathbf{k}\mathbf{k}'} = C_{m\mathbf{k}\mathbf{k}'}^{(1)} (V_{m\mathbf{k}'}^0 V_{m\mathbf{k}}^{0*} - \mathbf{V}_{m\mathbf{k}'} \cdot \mathbf{V}_{m\mathbf{k}}^*), \quad (33)$$

$$[J^{\text{S}}_{m\mathbf{k}\mathbf{k}'}]^{\alpha\beta} = C_{m\mathbf{k}\mathbf{k}'}^{(1)} (V_{m\mathbf{k}'}^{\alpha} V_{m\mathbf{k}}^{\beta*} + V_{m\mathbf{k}}^{\alpha*} V_{m\mathbf{k}'}^{\beta}), \quad (34)$$

$$[J^{\text{AS}}_{m\mathbf{k}\mathbf{k}'}]^{\alpha\beta} = i C_{m\mathbf{k}\mathbf{k}'}^{(1)} \sum_{\gamma} \epsilon_{\alpha\beta\gamma} (V_{m\mathbf{k}'}^{\gamma} V_{m\mathbf{k}}^{0*} - V_{m\mathbf{k}}^{\gamma*} V_{m\mathbf{k}'}^0), \quad (35)$$

with $C_{m\mathbf{k}\mathbf{k}'}^{(1)} = (B_{m\mathbf{k}} + B_{m\mathbf{k}'})/2$ and the Levi-Civita symbol $\epsilon_{\alpha\beta\gamma}$. The symmetric and antisymmetric exchange interactions satisfy $[J^{\text{S}}_{m\mathbf{k}\mathbf{k}'}]^{\alpha\beta} = [J^{\text{S}}_{m\mathbf{k}\mathbf{k}'}]^{\beta\alpha}$ and $[J^{\text{AS}}_{m\mathbf{k}\mathbf{k}'}]^{\alpha\beta} = -[J^{\text{AS}}_{m\mathbf{k}\mathbf{k}'}]^{\beta\alpha}$, respectively. The anisotropic exchange interactions vanish in the absence of the spin-dependent hybridizations. In addition, it is noted that these anisotropic interactions also vanish when \mathcal{H}^{cf} includes a single component of $(V_{m\mathbf{k}}^0, \mathbf{V}_{m\mathbf{k}})$.

The other spin-dependent term in Eq. (30) is the effective SOC for itinerant electrons, $\mathcal{H}^{\text{SOC}}_{m\sigma\sigma'}$, which is given by

$$\mathcal{H}^{\text{SOC}}_{m\sigma\sigma'} = \sum_{\mathbf{k}} \mathbf{g}_{m\mathbf{k}} \cdot c_{m\mathbf{k}\sigma}^{\dagger} \boldsymbol{\sigma}_{\sigma\sigma'} c_{m\mathbf{k}\sigma'}, \quad (36)$$

where

$$\mathbf{g}_{m\mathbf{k}} = C_{m\mathbf{k}}^{(2)} \left(V_{m\mathbf{k}}^{\alpha} V_{m\mathbf{k}}^{0*} + V_{m\mathbf{k}}^{\alpha*} V_{m\mathbf{k}}^0 - i \sum_{\beta,\gamma} \epsilon_{\alpha\beta\gamma} V_{m\mathbf{k}}^{\beta} V_{m\mathbf{k}}^{\gamma*} \right), \quad (37)$$

with $C_{m\mathbf{k}}^{(2)} = -(A_{m\mathbf{k}} + B_{m\mathbf{k}}/2)$. The effective SOC is induced by the spin-dependent hybridizations; $\mathbf{g}_{m\mathbf{k}}$ vanishes for $\mathbf{V}_{m\mathbf{k}} = \mathbf{0}$. The expression of $\mathbf{g}_{m\mathbf{k}}$ reduces to the antisymmetric spin-orbit interaction in the single-band system, which appears in noncentrosymmetric crystal systems.

C. Effective spin model

An effective spin model of the anisotropic Kondo lattice model in Eq. (9) is obtained by expanding the grand potential to second order with respect to the exchange coupling [73,74,77]. When taking $\mathbf{g}_{m\mathbf{k}} = \mathbf{0}$ for simplicity, the lowest second-order contribution of the exchange energy to the grand potential is given by

$$\begin{aligned} \Omega^{(2)} &= -\frac{T}{2} \int_0^{1/T} d\tau_1 \int_0^{1/T} d\tau_2 \langle \mathcal{T}_{\tau} \mathcal{H}_{\tau_1}^{\text{ex}} \mathcal{H}_{\tau_2}^{\text{ex}} \rangle_{\text{con}} \\ &= -\sum_{\mathbf{q}} \sum_{\alpha,\beta} X_{\mathbf{q}}^{\alpha\beta} S_{\mathbf{q}}^{\alpha} S_{-\mathbf{q}}^{\beta}, \end{aligned} \quad (38)$$

where T is the temperature, τ is the imaginary time, \mathcal{T}_{τ} is the time-ordered product, $\mathcal{H}_{\tau}^{\text{ex}} = e^{\tau \mathcal{H}^c} \mathcal{H}^{\text{ex}} e^{-\tau \mathcal{H}^c}$, and $\langle \dots \rangle_{\text{con}}$ represents the contributions from the connected Feynman diagrams. $X_{\mathbf{q}}^{\alpha\beta}$ in the second line corresponds to the interaction matrix in Sec. II, which is given by

$$\begin{aligned} X_{\mathbf{q}}^{\alpha\beta} &= \frac{T}{N} \sum_{m,\mathbf{k},\gamma,\omega_n} G_{m\mathbf{k}+\mathbf{q}}(i\omega_n) G_{m\mathbf{k}}(i\omega_n) J_{m\mathbf{k}+\mathbf{q}\mathbf{k}}^{\gamma\alpha} J_{m\mathbf{k}\mathbf{k}+\mathbf{q}}^{\gamma\beta} \\ &= \frac{1}{N} \sum_{m,\mathbf{k},\gamma} \frac{f(\varepsilon_{m\mathbf{k}}) - f(\varepsilon_{m\mathbf{k}+\mathbf{q}})}{\varepsilon_{m\mathbf{k}+\mathbf{q}} - \varepsilon_{m\mathbf{k}}} J_{m\mathbf{k}+\mathbf{q}\mathbf{k}}^{\gamma\alpha} J_{m\mathbf{k}\mathbf{k}+\mathbf{q}}^{\gamma\beta}, \end{aligned} \quad (39)$$

where $G_{m\mathbf{k}}(i\omega_n) = 1/(i\omega_n - \varepsilon_{m\mathbf{k}} + \mu)$ is the noninteracting Green's function with the Matsubara frequency ω_n , and $f(\varepsilon_{m\mathbf{k}})$ is the Fermi distribution function. It is noted that the Green's function does not depend on the spin, since we neglect

the effective SOC ($\mathbf{g}_{mk} = \mathbf{0}$), and then we omit its spin dependence for notational simplicity. \mathbf{D}_q , \mathbf{E}_q , and \mathbf{F}_q in Eq. (3) are related to $X_q^{\alpha\beta}$ in Eq. (39) as

$$D_q^\alpha = \frac{1}{2} \sum_{\beta,\gamma} \epsilon_{\alpha\beta\gamma} \text{Im}[X_q^{\beta\gamma}], \quad (40)$$

$$E_q^\alpha = \frac{1}{2} \sum_{\beta,\gamma} |\epsilon_{\alpha\beta\gamma}| \text{Re}[X_q^{\beta\gamma}], \quad (41)$$

$$F_q^\alpha = X_q^{\alpha\alpha}. \quad (42)$$

In this way, the momentum-resolved anisotropic interactions introduced in Eq. (3) are obtained based on the itinerant electron model. As shown in Eq. (39), the coupling matrix depends on the temperature and electronic states. It is noted that the anisotropic interactions are also obtained from the Kondo lattice model with $\mathbf{g}_{mk} \neq \mathbf{0}$ instead of $J_{mkk'}^S$ and $J_{mkk'}^{AS}$ [49,127,128].

The effective spin model in Eq. (38) is justified when the energy scale of the exchange interaction is smaller than that of the bandwidth. In the itinerant electron model, the dominant q components in the interactions giving the largest eigenvalue of X_q are related to the nesting vectors of the Fermi surface, as inferred from Eq. (39). As X_q is calculated when ε_{mk} , μ , V_{mk}^0 , and V_{mk} are given, one can quantitatively evaluate the contributions of the anisotropic interactions. For example, one can directly evaluate the anisotropic interactions in materials within the framework of the first-principles calculations.

Similar momentum-resolved spin models can be derived from other itinerant electron models. For example, the classical Kondo lattice model in the strong exchange coupling regime (double exchange model [129,130]) is mapped onto the effective spin model with the short-range spin interactions [131–134]. When taking into account the Rashba or Dresselhaus-type SOC, the short-range spin interactions become anisotropic [88,135–139]. Furthermore, the effective spin model with the short-range spin interactions can be constructed based on the Hubbard model with the SOC [136,140,141]. In these cases, the momentum-resolved effective spin model in Eq. (10) is obtained once the dominant interaction in q space (including $q = \mathbf{0}$ component) is extracted.

IV. ORIGIN OF THE ANISOTROPIC EXCHANGE INTERACTIONS: CASE OF LOCALIZED SPIN MODELS

In the previous section, we show that the momentum-resolved anisotropic exchange interaction is obtained as the effective long-range (short-range) interaction for itinerant electron models. Meanwhile, the above momentum-resolved anisotropic exchange interaction is also related to the short-range interaction in the localized spin model. For example, a ground-state magnetic phase diagram has been constructed by considering the dominant q interactions in frustrated magnets [80,142] and DM-based magnets [143]. In the localized spin model, the anisotropic exchange interaction originates from the relativistic SOC, which largely depends on the point-group symmetry in crystals [90,91,144–153]. In such a situation, the microscopic origin of the interaction matrix X_q in Eq. (10) is attributed to the Fourier transform of real-space anisotropic

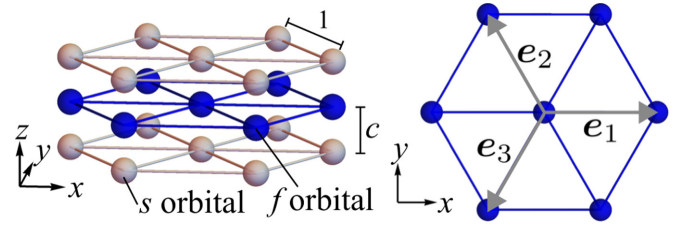


FIG. 5. Left panel: $P6/mmm$ crystal lattice consisting of three layers. The blue (gray) spheres represent magnetic (nonmagnetic) ions with the f (s) orbital and form the triangular lattice on the xy plane. The three layers are stacked along the z direction at equal intervals of c . Right panel: the triangular lattice viewed from the z direction; \mathbf{e}_1 , \mathbf{e}_2 , and \mathbf{e}_3 are the unit vectors.

exchange interactions. Furthermore, the effective spin model can include the effect of the dipolar interactions by performing the Fourier transformation, which is renormalized into \mathbf{E}_q and \mathbf{F}_q [53,69].

V. APPLICATION TO A SPECIFIC HEXAGONAL SYSTEM

We apply the above general expression to a specific hexagonal crystal system under the space group $P6/mmm$ at low temperatures. Starting from the PAM in Sec. VA and mapping it onto the effective spin model in Sec. VB, we show the multiple- Q instability in the ground state by performing the simulated annealing in Sec. VC.

A. Anisotropic periodic Anderson model

As an example, we consider the specific $P6/mmm$ crystal lattice consisting of three triangular-lattice layers separated by a distance c , as shown in the left panel of Fig. 5; the localized f orbitals denoted by the blue spheres lie on the middle layer, and the itinerant s orbitals denoted by the gray spheres lie on the upper and lower layers. We set the lattice constant of the triangular lattice as the length unit.

The system is described by the multiband anisotropic PAM in Eq. (21) under the periodic boundary condition in the x and y directions. The energy dispersion of the itinerant electron in \mathcal{H}^c in the upper and lower layers is given by

$$\varepsilon_{mk} = -2 \sum_{i=1,2,3} (t_1 \cos \mathbf{k} \cdot \mathbf{e}_i + t_3 \cos 2\mathbf{k} \cdot \mathbf{e}_i), \quad (43)$$

where $\mathbf{k} = (k_x, k_y)$ is the two-dimensional wave vector; $\mathbf{e}_1 = (1, 0)$, $\mathbf{e}_2 = (-1/2, \sqrt{3}/2)$, and $\mathbf{e}_3 = (-1/2, -\sqrt{3}/2)$ are the unit vectors of the triangular lattice (the right panel of Fig. 5); and $m = +(-)$ represents the upper (lower) nonmagnetic layer. Here, we consider the hoppings between the nearest- and third-neighbor sites, t_1 and t_3 , within the same layer.

Meanwhile, we suppose that the f orbital with the Kramers twofold degeneracy is anisotropic in spin space by incorporating the effect of the SOC and the crystalline electric field (CEF) under the $P6/mmm$ symmetry in the following way. By assuming that the magnitude of SOC is greater than that of CEF, the 14 degenerate f electron states are split into two levels with the total angular momentum $j = 7/2$ and $5/2$ by the SOC, and then they are split into a total of seven Kramers

pairs by the CEF. We choose one out of seven Kramers pairs, which is expressed as

$$\begin{aligned}
 f_{i\uparrow}^\dagger |0\rangle &= \alpha_{\text{CEF}} \left| i, 3, \frac{1}{2} \right\rangle + \sqrt{1 - \alpha_{\text{CEF}}^2} \left(\sqrt{\frac{6}{7}} \left| i, -2, -\frac{1}{2} \right\rangle \right. \\
 &\quad \left. + \sqrt{\frac{1}{7}} \left| i, -3, \frac{1}{2} \right\rangle \right), \\
 f_{i\downarrow}^\dagger |0\rangle &= -\alpha_{\text{CEF}} \left| i, -3, -\frac{1}{2} \right\rangle \\
 &\quad - \sqrt{1 - \alpha_{\text{CEF}}^2} \left(\sqrt{\frac{6}{7}} \left| i, 2, \frac{1}{2} \right\rangle + \sqrt{\frac{1}{7}} \left| i, 3, -\frac{1}{2} \right\rangle \right),
 \end{aligned} \quad (44)$$

where $|i, l_z, s_z\rangle$ is characterized by the site i and the magnetic quantum number of the f orbital ($l_z = -3, -2, \dots, 3$) and spin ($s_z = \pm 1/2$), and α_{CEF} ($|\alpha_{\text{CEF}}| \leq 1$) is a constant depending on the CEF parameters. It is noted that the subscripts \uparrow and \downarrow on the left-hand side represent the pseudospin to satisfy $\theta f_{i\uparrow}^\dagger |0\rangle = f_{i\downarrow}^\dagger |0\rangle$ and $\theta f_{i\downarrow}^\dagger |0\rangle = -f_{i\uparrow}^\dagger |0\rangle$ for the time-reversal operation θ . $|i, \pm 3, s_z\rangle$ and $|i, \pm 2, s_z\rangle$ on the right-hand side are related to the real expressions of the f orbitals $|3a\rangle \propto \sqrt{10}x(x^2 - 3y^2)/4$, $|3b\rangle \propto \sqrt{10}y(3x^2 - y^2)/4$, $|\beta z\rangle \propto \sqrt{15}z(x^2 - y^2)/2$, and $|xyz\rangle \propto \sqrt{15}xyz$ as

$$|i, \pm 3, s_z\rangle = \mp \frac{1}{\sqrt{2}} |i, 3a, s_z\rangle - \frac{i}{\sqrt{2}} |i, 3b, s_z\rangle, \quad (46)$$

$$|i, \pm 2, s_z\rangle = \frac{1}{\sqrt{2}} |i, \beta z, s_z\rangle \pm \frac{i}{\sqrt{2}} |i, xyz, s_z\rangle. \quad (47)$$

Then, the hybridizations V_{mk}^0 and V_{mk}^α ($\alpha = x, y, z$) in \mathcal{H}^{cf} are given by

$$V_{mk}^0 = \sum_d T_{md}^0 e^{ik \cdot d}, \quad (48)$$

$$V_{mk}^\alpha = \sum_d T_{md}^\alpha e^{ik \cdot d}, \quad (49)$$

where \mathbf{d} represents the vector connecting the s orbital at $\mathbf{R}_i + \mathbf{d}$ and the f orbital at \mathbf{R}_i , and

$$T_{md}^0 = \frac{-\sqrt{7}\alpha_{\text{CEF}} + \sqrt{1 - \alpha_{\text{CEF}}^2}}{\sqrt{14}} t_d^{3a}, \quad (50)$$

$$T_{md}^x = i\sqrt{1 - \alpha_{\text{CEF}}^2} \sqrt{\frac{3}{7}} t_d^{xyz}, \quad (51)$$

$$T_{md}^y = i\sqrt{1 - \alpha_{\text{CEF}}^2} \sqrt{\frac{3}{7}} t_d^{\beta z}, \quad (52)$$

$$T_{md}^z = i \frac{\sqrt{7}\alpha_{\text{CEF}} + \sqrt{1 - \alpha_{\text{CEF}}^2}}{\sqrt{14}} t_d^{3b}, \quad (53)$$

with $t_d^{3a} = \sqrt{10}l(l^2 - 3m^2)(\text{sf}\sigma)/4$, $t_d^{3b} = \sqrt{10}m(3l^2 - m^2)(\text{sf}\sigma)/4$, $t_d^{\beta z} = \sqrt{15}n(l^2 - m^2)(\text{sf}\sigma)/2$, and $t_d^{xyz} = \sqrt{15}lmn(\text{sf}\sigma)$. (l, m, n) = $\mathbf{d}/|\mathbf{d}|$ and $(\text{sf}\sigma)$ is the Slater-Koster parameter [154]. Hereafter, we set $(\text{sf}\sigma) = 1$, $\mathbf{d} = \pm \mathbf{e}_1 + m(0, 0, c)$, $\pm \mathbf{e}_2 + m(0, 0, c)$, and $\pm \mathbf{e}_3 + m(0, 0, c)$. Then, V_{mk}^z vanishes for any α_{CEF} and c due to the symmetry of $|3b\rangle$. In addition, for $\alpha_{\text{CEF}} = \pm 1$ or $c = 0$, $V_{mk}^x = V_{mk}^y = 0$,

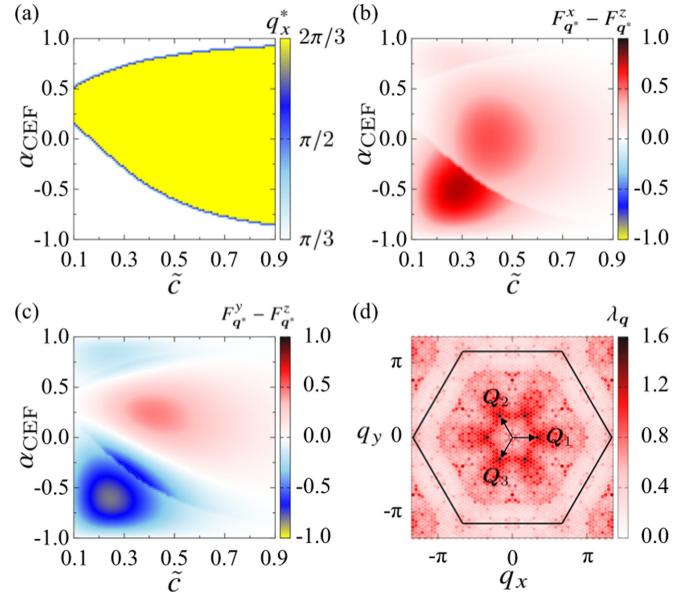


FIG. 6. α_{CEF} and $\tilde{c} = c/\sqrt{3}$ dependences of (a) q^* giving the largest eigenvalue of X_q , (b) $F_q^x - F_q^z$, and (c) $F_q^y - F_q^z$. (d) Eigenvalues λ_q in momentum space at $\alpha_{\text{CEF}} = -0.8$ and $c = 0.4$, where the hexagon with a solid line shows the first Brillouin zone. The maxima appear at $\mathbf{Q}_1 = \mathbf{e}_1\pi/3$, $\mathbf{Q}_2 = \mathbf{e}_2\pi/3$, and $\mathbf{Q}_3 = \mathbf{e}_3\pi/3$. The other parameters are set as $t_1 = 1$, $t_3 = -0.85$, $\mu = 1.3$, $C_{mkk'}^{(1)} = 1$, $T = 0.02$, and $N = 48^2$.

as t_d^{xyz} and $t_d^{\beta z}$ are proportional to n . In this situation, the anisotropic interaction in Eqs. (40)–(42) appears for $\alpha_{\text{CEF}} \neq \pm 1$ and $c \neq 0$. It is noted that the nearest-neighbor hybridizations by $\mathbf{d} = (0, 0, \pm c)$ vanish for any α_{CEF} and c due to the symmetry in the present system.

B. Effective spin model

Following the procedure in Sec. III, we derive the effective spin model for the present PAM, which enables us to search for the multiple- Q instability. From the symmetry argument, there are three independent components (F_q) in X_q for the high-symmetric lines, e.g., $\mathbf{q} = (q_x, 0)$ and $\mathbf{q} = (0, q_y)$, while there are four independent components (F_q and E_q^z) for a general \mathbf{q} , as shown in Tables VI and X. In each \mathbf{q} , the interaction matrix X_q is calculated when the model parameters ($t_1, t_3, \mu, U, E_f, V_{mk}, T$) are given. It is noted that V_{mk} is determined by α_{CEF} and the distance c , and U and E_f are used for $C_{mkk'}^{(1)}$. Here, we evaluate X_q by setting $t_1 = 1$, $t_3 = -0.85$, and $\mu = 1.3$. For the parameters, we neglect the wave-vector dependence of $C_{mkk'}^{(1)}$ in Eqs. (33)–(35) by supposing the situation in which U and $|E_f|$ are larger than the bandwidth. Besides, we set $C_{mkk'}^{(1)} = 1$ for simplicity.

We first calculate the optimal ordering vector $\mathbf{q}^* = (q_x^*, q_y^*)$ that gives the maximum eigenvalue of X_q while changing α_{CEF} and $\tilde{c} = c/\sqrt{3}$ at a low temperature $T = 0.02$ for the system size $N = 48^2$. As shown in Fig. 6(a), the maximum eigenvalue of X_q is obtained for $\mathbf{q}^* = (\pi/3, 0)$ drawn by the white region, while it is obtained for $\mathbf{q}^* = (q_x^*, q_y^*)$ with $q_x^* \neq \pi/3$ and $q_y^* \neq 0$ drawn by the color region. We also plot the anisotropic exchange interactions, $F_q^x - F_q^z$ and $F_q^y - F_q^z$, in Figs. 6(b) and 6(c), respectively. One finds that the anisotropic

TABLE VIII. λ_q , F_q^x , F_q^y , F_q^z , and E_q^z at \mathbf{Q}_1 , $2\mathbf{Q}_1$, $3\mathbf{Q}_1$, $2\mathbf{Q}_1 - \mathbf{Q}_3$, and $\mathbf{Q}_1 - \mathbf{Q}_3$ at $\alpha_{\text{CEF}} = -0.8$ and $c = 0.4$, where $\mathbf{Q}_1 = \mathbf{e}_1\pi/3$, $\mathbf{Q}_2 = \mathbf{e}_2\pi/3$, and $\mathbf{Q}_3 = \mathbf{e}_3\pi/3$. The other parameters are the same as those in Fig. 6.

q	λ_q	F_q^x	F_q^y	F_q^z	E_q^z
\mathbf{Q}_1	1.53	1.53	0.76	1.16	0.00
$2\mathbf{Q}_1$	0.82	0.82	0.24	0.79	0.00
$3\mathbf{Q}_1$	0.80	0.80	0.45	0.65	0.00
$2\mathbf{Q}_1 - \mathbf{Q}_3$	0.64	0.55	0.30	0.64	-0.09
$\mathbf{Q}_1 - \mathbf{Q}_3$	0.55	0.46	0.28	0.52	0.16

interaction to satisfy $F_{q^*}^x > F_{q^*}^y$, $F_{q^*}^z$ is realized in almost the region except for $\alpha_{\text{CEF}} = \pm 1$, where only the isotropic spin interaction appears, i.e., $F_{q^*}^x = F_{q^*}^y = F_{q^*}^z$. In other words, the magnitude of anisotropic interactions largely depends on α_{CEF} and c . In particular, the reversal of the magnitude relation between $F_{q^*}^y$ and $F_{q^*}^z$ in Fig. 6(c) indicates the instability toward the different spiral or multiple- Q states. For example, the tendency toward the out-of-plane (in-plane) cycloidal spin is expected for $\alpha_{\text{CEF}} = -0.5$ and $\tilde{c} = 0.3$ ($\alpha_{\text{CEF}} = 0.3$ and $\tilde{c} = 0.5$).

In the following, we fix the parameters as $\alpha_{\text{CEF}} = -0.8$ and $\tilde{c} = 0.4$, which gives the optimal ordering vectors as $\pm\mathbf{Q}_1 = \pm\mathbf{e}_1\pi/3$, $\pm\mathbf{Q}_2 = \pm\mathbf{e}_2\pi/3$, and $\pm\mathbf{Q}_3 = \pm\mathbf{e}_3\pi/3$. We plot the q dependence of the largest eigenvalue of X_q at each q denoted as λ_q in Fig. 6(d). We summarize the numerical values of λ_q , F_q^x , F_q^y , F_q^z , and E_q^z at \mathbf{Q}_1 in Table VIII. In addition, we show them at wave vectors given by linear combinations of \mathbf{Q}_1 , \mathbf{Q}_2 , and \mathbf{Q}_3 for later convenience.

C. Multiple- Q instability

1. Simulated annealing

We investigate the low-temperature magnetic phases in the presence of the effective anisotropic interactions X_q obtained in Sec. VB. Here, we add the Zeeman term, $\mathcal{H}^Z = -H \sum_i S_i^z$, to the effective anisotropic spin model in Eq. (9) in order to investigate the effects of the magnetic field H . It is noted that the introduction of the magnetic field along the z direction does not lead to the additional anisotropic bilinear interactions. The spin configuration is obtained by using the simulated annealing combined with the standard Metropolis local updates. To focus on the multiple- Q instability in the ground state, we ignore the temperature dependence of X_q for simplicity. We gradually reduce the temperature with a rate $T_{n+1} = \alpha T_n$, where T_n is the temperature at the n th step. We set the initial temperature $T_0 = 1$ and the coefficient $\alpha \approx 0.993$ 116. A final temperature $T_f = 0.001$ is reached after a total of 10^5 Monte Carlo steps, where we perform 10^2 Monte Carlo steps at each temperature T_n . At the final temperature, we perform 10^4 Monte Carlo steps for thermalization and measurements, respectively. To determine the phase boundary, we set the spin configuration obtained near the phase boundary as the initial spin configuration and perform the simulated annealing starting at a low temperature ($T_0 = 0.05, 0.01$). In the simulation, we again set $\lambda_{\mathbf{Q}_1}$ as the energy unit. Moreover, we treat the

spin as the classical one with fixing the spin length at each site ($|\mathbf{S}_i| = 1$) for simplicity.

We identify magnetic phases by measuring a magnetic moment, a spin scalar chirality, and the skyrmion number. The magnetic moment with wave vector q is defined as

$$m_q^\alpha = \sqrt{\left\langle \frac{1}{N^2} \sum_{j,k} S_j^\alpha S_k^\alpha e^{iq \cdot (\mathbf{R}_j - \mathbf{R}_k)} \right\rangle}, \quad (54)$$

where $\alpha = x, y, z$ and $\langle \dots \rangle$ is the average over the Monte Carlo samples. The in-plane and out-of-plane magnetic moments are given by $m_q^\perp = \sqrt{(m_q^x)^2 + (m_q^y)^2}$ and m_q^z , respectively. $m_{q=0}$ corresponds to the uniform magnetization \mathbf{M} . The spin scalar chirality of the triangle is defined as $\chi_r = [\mathbf{S}_j \cdot (\mathbf{S}_k \times \mathbf{S}_l)]$, where the position vector \mathbf{r} represents the triangle center and the triangle consists of (j, k, l) sites labeled in counterclockwise order. The uniform spin scalar chirality is given by $\chi_{\text{sc}} = \langle \sum_r \chi_r / N \rangle$. The spin scalar chirality with wave vector q is given by

$$\chi_q = \sqrt{\left\langle \frac{1}{N^2} \sum_\mu \sum_{r,r' \in \mu} \chi_r \chi_{r'} e^{iq \cdot (\mathbf{r} - \mathbf{r}')} \right\rangle}, \quad (55)$$

where $\mu = (u, d)$ represents upward and downward triangles, respectively. A skyrmion density Ω_r [155] at the triangle \mathbf{r} is defined as

$$\tan\left(\frac{\Omega_r}{2}\right) = \left[\frac{\mathbf{S}_j \cdot (\mathbf{S}_k \times \mathbf{S}_l)}{1 + \mathbf{S}_j \cdot \mathbf{S}_k + \mathbf{S}_k \cdot \mathbf{S}_l + \mathbf{S}_l \cdot \mathbf{S}_j} \right]. \quad (56)$$

Then, the skyrmion number is given by

$$N_{\text{sk}} = \frac{1}{4\pi N_m} \left\langle \sum_r \Omega_r \right\rangle, \quad (57)$$

where N_m is the number of the magnetic unit cell.

In the following, we discuss three situations with different sets of wave vectors, $\{\mathbf{Q}\}$. First, we analyze the ground state of the effective spin model by taking into account all the q contributions in the interactions in Sec. VC2. As mentioned in Sec. IIB1, part of the interactions are important to describe the magnetic instability at low temperatures. Therefore, we discuss the minimum effective spin model to reproduce the results in Sec. VC2. In Sec. VC3, we find that it is not enough to reproduce the results in Sec. VC2 when considering only the contributions from \mathbf{Q}_1 - \mathbf{Q}_3 . In Sec. VC4, we show that the additional contribution from $3\mathbf{Q}_1$ - $3\mathbf{Q}_3$ well reproduces the results in Sec. VC2.

2. Case of the interactions at all the wave vectors

In the effective spin model with the interactions at all the wave vectors q except for $q = 0$, we investigate the ground state of the effective spin model while changing the magnetic field H . We show H dependences of the in-plane magnetic moment at \mathbf{Q}_1 - \mathbf{Q}_3 , $(m_{\mathbf{Q}_1}^\perp)^2$, in Fig. 7(a), the out-of-plane magnetic moment at \mathbf{Q}_1 - \mathbf{Q}_3 , $(m_{\mathbf{Q}_1}^z)^2$, in Fig. 7(b), the spin scalar chirality at \mathbf{Q}_1 - \mathbf{Q}_3 , $(\chi_{\mathbf{Q}_1})^2$, in Fig. 7(c), the uniform magnetization M^z and the uniform spin scalar chirality $|\chi_{\text{sc}}|$ in Fig. 7(d), and the skyrmion number N_{sk} in Fig. 7(e), where we

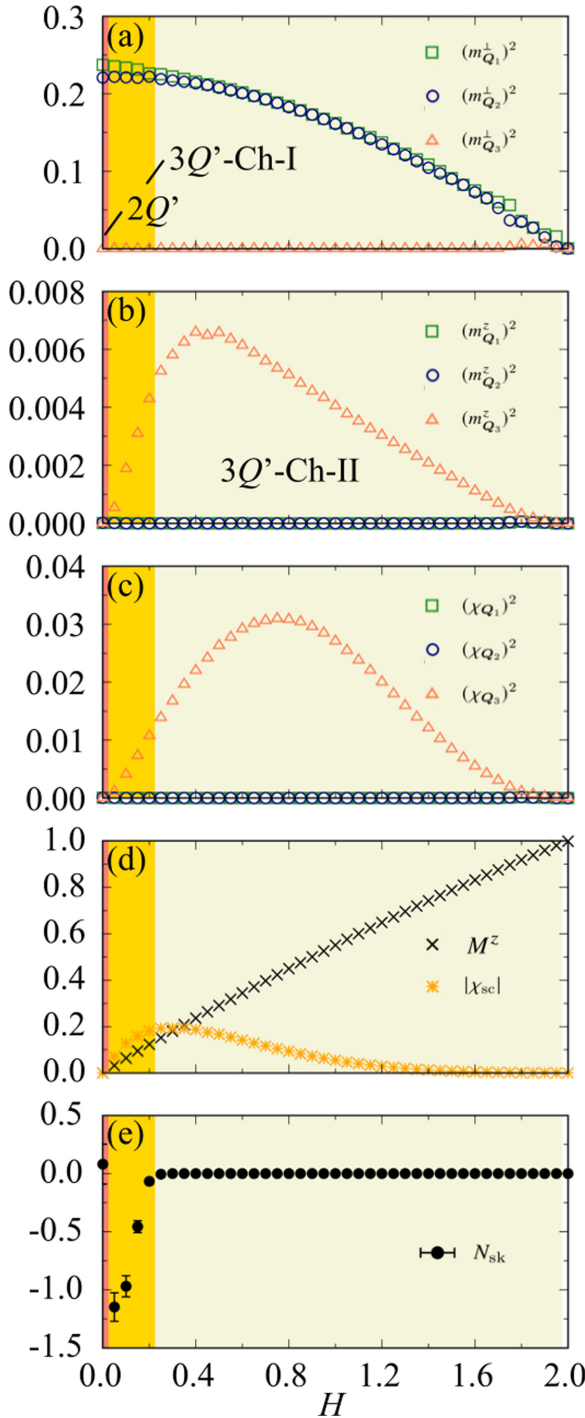


FIG. 7. H dependences of (a) $(m_{Q_1}^\perp)^2$, (b) $(m_{Q_2}^\perp)^2$, (c) $(\chi_{Q_1})^2$, (d) M^z and $|\chi_{sc}|$, and (e) N_{sk} in the model with the interactions at all the wave vectors. We sort $m_{Q_1}^\perp$, $m_{Q_2}^\perp$, and χ_{Q_1} to satisfy $m_{Q_1}^\perp \geq m_{Q_2}^\perp \geq m_{Q_3}^\perp$.

sort $m_{Q_1}^\perp$, $m_{Q_2}^\perp$, and χ_{Q_1} to satisfy $m_{Q_1}^\perp \geq m_{Q_2}^\perp \geq m_{Q_3}^\perp$ for better readability. In addition to the fully polarized state at $H = 2$, we find three types of the multiple- Q states; all the states are characterized by m_{Q_η} , since X_q has the largest eigenvalues at Q_η , as detailed below. These multiple- Q states are stabilized by magnetic anisotropy rather than thermal fluctuations.

Figure 8 shows the spin and chirality configurations in real space and the magnetic moments in momentum space for each multiple- Q state. The skyrmion density configurations in real space for each multiple- Q state are shown in Fig. 9.

At $H = 0$, the ground state becomes a double- Q ($2Q'$) state. In this state, the spin configuration is characterized by the double- Q in-plane components $m_{Q_1}^\perp$ and $m_{Q_2}^\perp$ with different intensities and no out-of-plane components at Q_1 - Q_3 (Q' represents different intensities of the Q_1 and Q_2 components), as shown in Figs. 7(a) and 7(b). The real-space spin configuration is shown in the first column of Fig. 8(a). The in-plane spins form a periodic structure consisting of the vortex (circle) and antivortex (square), while the z spins show no periodic structure. Such a tendency is found in the presence (absence) of sharp peaks in m_q^\perp (m_q^z), as shown in the third (fourth) column of Fig. 8(a). In the scalar chirality sector, this state exhibits $\chi_{Q_\eta} = 0$ and $\chi_{sc} = 0$, as shown in Figs. 7(c) and 7(d), respectively. In the real-space picture, the local scalar chirality is randomly distributed, as shown in the second column of Fig. 8(a). Accordingly, there is no skyrmion number ($N_{sk} = 0$) in Fig. 7(e).

By applying a magnetic field, the $2Q'$ state changes into a triple- Q chiral I ($3Q'$ -Ch-I) state, whose spin structure is characterized by the double- Q in-plane components $m_{Q_1}^\perp > m_{Q_2}^\perp$ and the single- Q z component $m_{Q_3}^z$, as shown in Figs. 7(a) and 7(b). The in-plane spin configuration of the $3Q'$ -Ch-I state is similar to that of the $2Q'$ state, as shown in the first and third columns of Fig. 8(b). Meanwhile, the first and fourth columns of Fig. 8(b) show a structure of z spin components due to the single- Q peak of $m_{Q_\eta}^z$, where the z spins have positive (small positive or negative) values at antivortices (vortices). The undetermined sign of the z spins at vortices is due to the small value of $m_{Q_\eta}^z$, which results in the fluctuations of N_{sk} characterized by noninteger values, as shown in Fig. 7(e). The $3Q'$ -Ch-I state shows a nonzero uniform scalar chirality [Fig. 7(d)] as well as the chirality density wave along the Q_3 direction [Fig. 7(c)]. The nonzero uniform scalar chirality is attributed to the inequivalence between the z spin component at antivortices and vortices, as found in the real-space spin and chirality configurations in Fig. 8(b); there is a large negative chirality at antivortices with large z spins and a small negative/positive chirality at vortices with small z spins.

While increasing H , the peak structures of $m_{Q_\eta}^z$ and M^z are developed, and then there are no fluctuations in N_{sk} for $H \gtrsim 0.225$. We call this state a triple- Q chiral II ($3Q'$ -Ch-II) state. As the difference of $m_{Q_1}^\perp$, $m_{Q_2}^\perp$, χ_{Q_η} , and χ_{sc} between the $3Q'$ -Ch-I phase and the $3Q'$ -Ch-II phase seems to be slight in Figs. 7(a)–7(d), the similar spin and chirality configurations in real and momentum spaces appear in Figs. 8(b) and 8(c). By closely looking into their spin configurations, one finds that all spins have positive z components in the $3Q'$ -Ch-II phase in Fig. 8(c), which is presumably due to the development of $m_{Q_\eta}^z$ and M^z . As a result, the positive chirality contribution appears at vortices, which leads to the suppression of the total scalar chirality, as shown in Fig. 7(d). While further increasing H , the chirality contributions from the vortices and antivortices are canceled out, and then this state turns into the fully polarized state at $H = 2$.

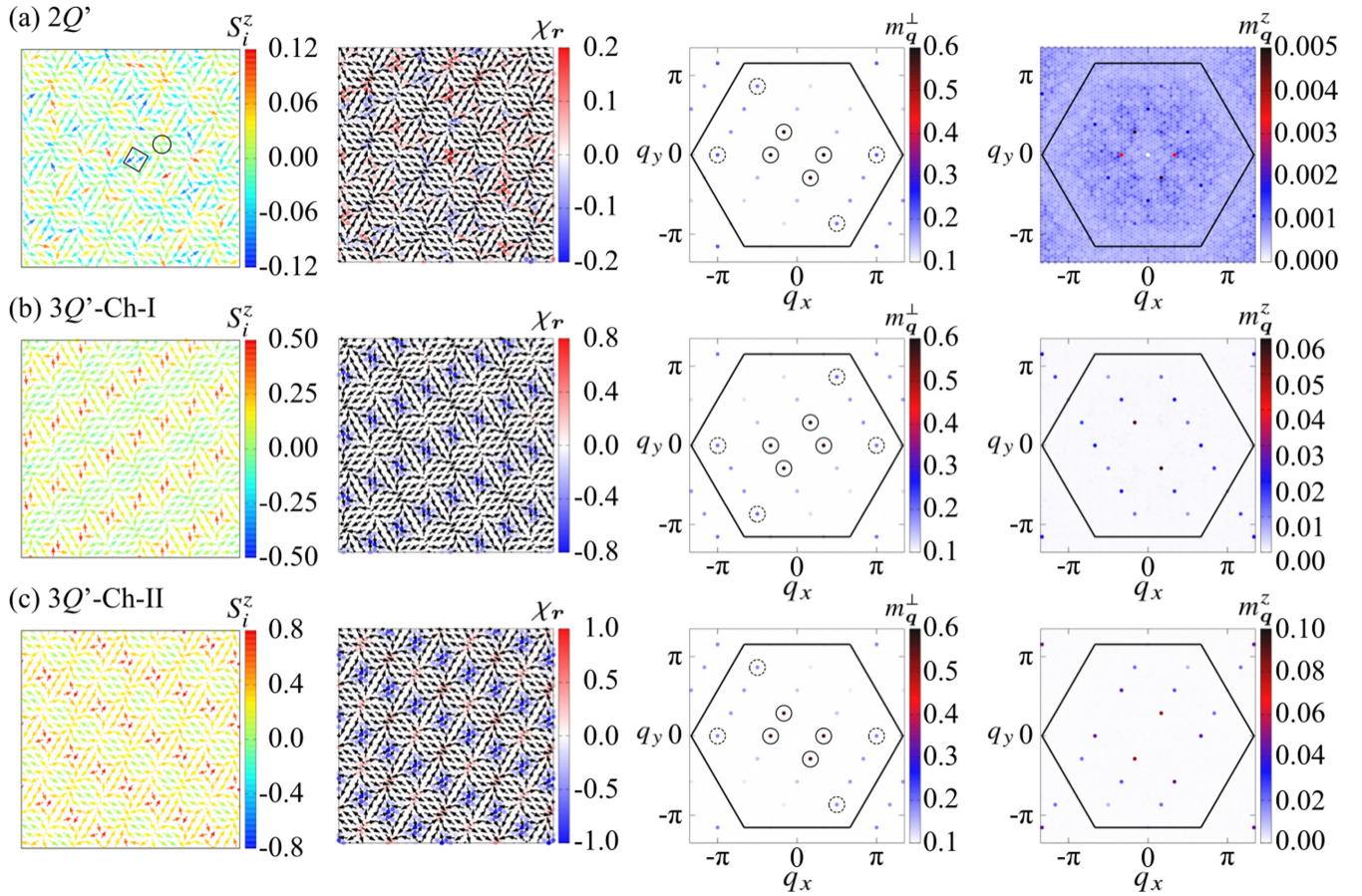


FIG. 8. First column: The spin configurations averaged over 500 Monte Carlo steps of (a) the $2Q'$ state at $H = 0$, (b) the $3Q'$ -Ch-I state at $H = 0.15$, and (c) the $3Q'$ -Ch-II state at $H = 0.5$. The arrows and contours show the xy and z components of the spin, respectively. The circle (square) highlights the vortex (antivortex) structure in the xy spins. Second column: The scalar chirality configurations of the first column. Third and fourth columns: The in-plane and out-of-plane magnetic moments in momentum space. The solid and dashed circles in the third column highlight the Q_η and $3Q_\eta$ components, respectively. The hexagons with a solid line show the first Brillouin zone. The $q = 0$ component is removed for better visibility.

We further discuss the H dependence of N_{sk} in Fig. 7(e), especially for the small H region, where N_{sk} takes a noninteger value. We plot the real-space skyrmion density configurations in Fig. 9. All the states have the large skyrmion density near the (anti)vortex cores. At $H = 0$, the skyrmion number becomes zero within the errorbars, where both vortices and antivortices take a random value, as shown in Fig. 9(a). For $H > 0$, N_{sk} takes a noninteger value in the $3Q'$ -Ch-I state. In this state, the antivortices take a negative value, while the vortices take a positive or negative value at random, as shown in Figs. 9(b) and 9(c). This randomness is the reason why N_{sk} becomes the noninteger values. Such randomness is suppressed while increasing H , as shown in Figs. 9(b) and 9(c). In the end, the randomness vanishes in the $3Q'$ -Ch-II state, since the vortices always take a positive value, as shown in Fig. 9(d). This result indicates that the energy scale of F_q^z is too small to lead to the sharp peak of $m_{Q_\eta}^z$, which makes the skyrmion density at the vortices ambiguous. The ambiguity of skyrmion density is also suppressed while decreasing T . Indeed, we confirm that the $3Q'$ -Ch-I state turns into the state with $N_{\text{sk}} = -2$ at $0 < H < 0.1$ and that with $N_{\text{sk}} = 0$ at $H \geq 0.1$ by using a more efficient

simulation method, a heat-bath method at zero temperature limit.

3. Case of the interactions at Q_η

To identify the origin of the multiple- Q states, we consider the minimum model to reproduce the results in Fig. 7 by dropping off the less important q component of the interactions. In the previous section, we find that the model shows the instability toward the multiple- Q states with the scalar chirality, where there are no contributions from the interactions at almost all q channels except for Q_η and their higher harmonics, as discussed in Sec. II B 1. In this section, we only consider the contributions of the interactions at $\{Q\} = \{\pm Q_1, \pm Q_2, \pm Q_3\}$, since they give the maximum eigenvalue of X_q .

As a result, we find that the model with the interactions at $\{Q\} = \{\pm Q_1, \pm Q_2, \pm Q_3\}$ is oversimplified in the present situation. The H dependences in Fig. 10 show that the magnetic phases in the present model are different from those in Sec. VC 2; we obtain the $2Q'$ -CS, $3Q'$ -SkX, $3Q$ -SkX, and $3Q$ -Ch states that are not stabilized in the model in Sec. VC 2. In particular, the appearance of $3Q'$ -SkX and $3Q$ -

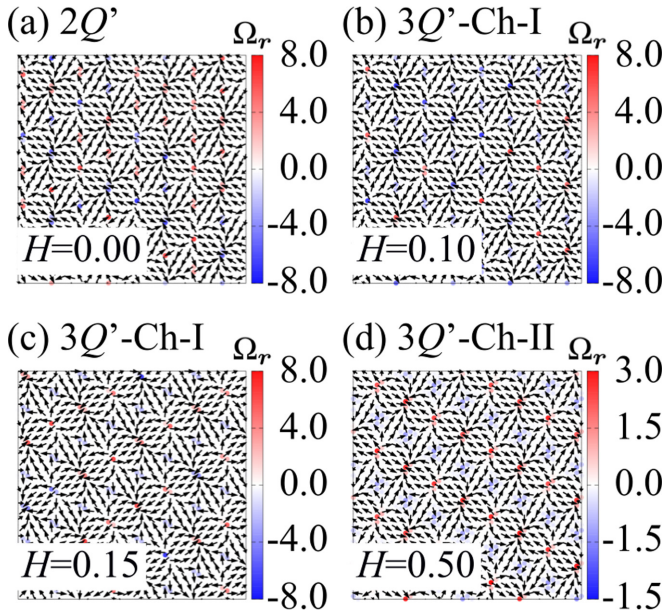


FIG. 9. Skyrmion density configurations of (a) the $2Q'$ state at $H = 0$, (b) the $3Q'$ -Ch-I state at $H = 0.1$, (c) the $3Q'$ -Ch-I state at $H = 0.15$, and (d) the $3Q'$ -Ch-II state at $H = 0.5$. The skyrmion density is calculated by using the spin configuration averaged over 500 Monte Carlo steps.

SkX with $N_{\text{sk}} = -1$ is a characteristic of the oversimplified model, whose real-space spin and chirality configurations are shown in Fig. 11. In the $3Q'$ -SkX state, the in-plane spin configuration is similar to that in the $3Q'$ -Ch-I state, while there is a difference in the z spin configurations; the $3Q'$ -SkX state in Fig. 11(a) [the $3Q'$ -Ch-I state in Fig. 8(b)] has the (no) alternating arrangement of vortices with the positive and negative z spins in the Q_3 direction. Meanwhile, The $3Q$ -SkX state in Fig. 11(b) shows an entirely different structure, which is expressed as the superposition of the three cycloidal elliptical waves with the same intensity. The $3Q$ -SkX state is similar to the SkX in Fig. 4(b), since it is stabilized by the interplay among large $F_{Q_1}^x$, the isotropic interaction, and the magnetic field, as discussed in Sec. II C 2. We show the real-space spin and chirality configurations, the q -space magnetic moments, and the skyrmion density configurations for the obtained states in Appendix D for reference.

4. Case of the interactions at Q_η and $3Q_\eta$

Next, we focus on the contribution from higher harmonics for the following reasons. By comparing the q -resolved magnetic moments shown in Figs. 8 and 15, we find that the discrepancy between the results in Figs. 7 and 10 appears in the magnetic moments at higher-harmonic wave vectors. Indeed, the values of λ_q and F_q at $2Q_1$, $3Q_1$, and $2Q_1 - Q_3$ are large enough to compete with those at Q_1 , as shown in Table VIII. On the basis of the above discussion, we additionally take into account the interactions at the higher-harmonic wave vectors with those at Q_ν .

By performing the numerical simulations for several models with different $\{Q\}$, we find that the introduction of the interactions at $\pm 3Q_1, \pm 3Q_2, \pm 3Q_3$ is enough to

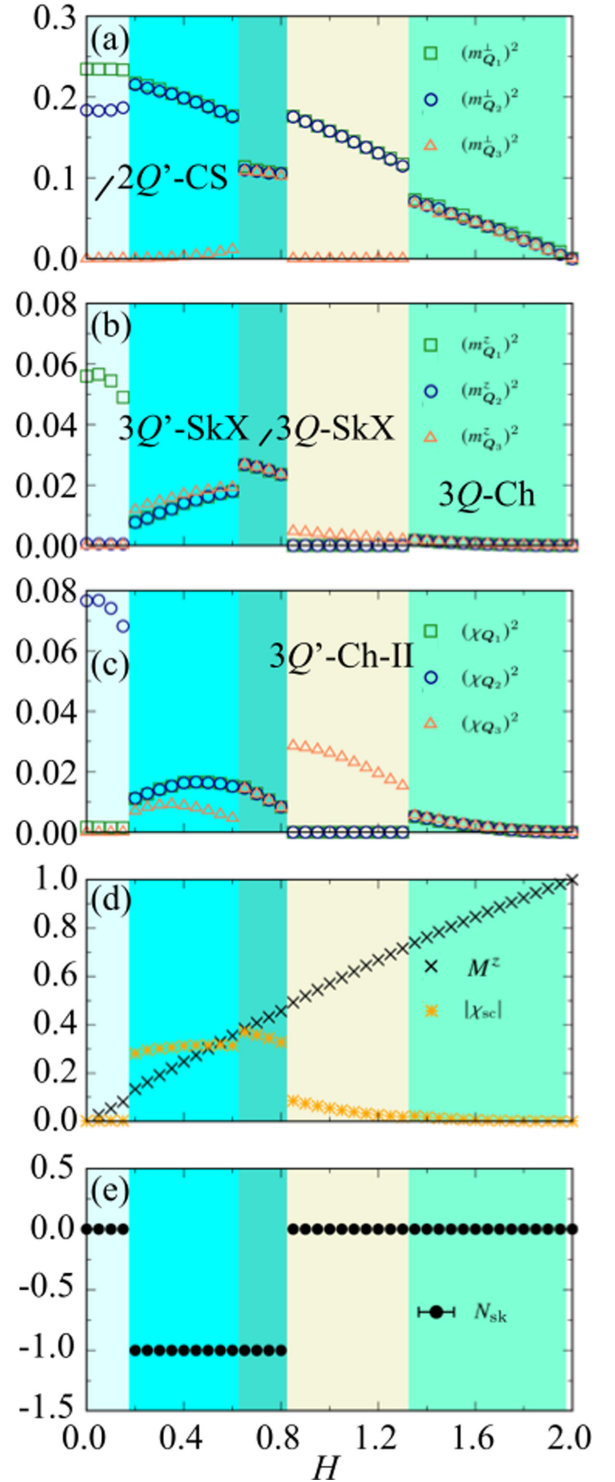


FIG. 10. H dependences of (a) $(m_{Q_1}^\perp)^2$, (b) $(m_{Q_2}^\perp)^2$, (c) $(\chi_{Q_\eta})^2$, (d) M^z and $|\chi_{\text{sc}}|$, and (e) N_{sk} in the model with the Q_η channels. We sort $m_{Q_\eta}^\perp, m_{Q_\eta}^z$, and χ_{Q_η} to satisfy $m_{Q_1}^\perp \geq m_{Q_2}^\perp \geq m_{Q_3}^\perp$.

reproduce the results in Fig. 7. We show the results for the model with $\{Q\} = \{\pm Q_1, \pm Q_2, \pm Q_3, \pm 3Q_1, \pm 3Q_2, \pm 3Q_3\}$ in Fig. 12. Compared to the results in Fig. 7, the H dependences of spin- and chirality-related quantities are reproduced except for the high-field region, $H \gtrsim 1.625$. It is noted that there

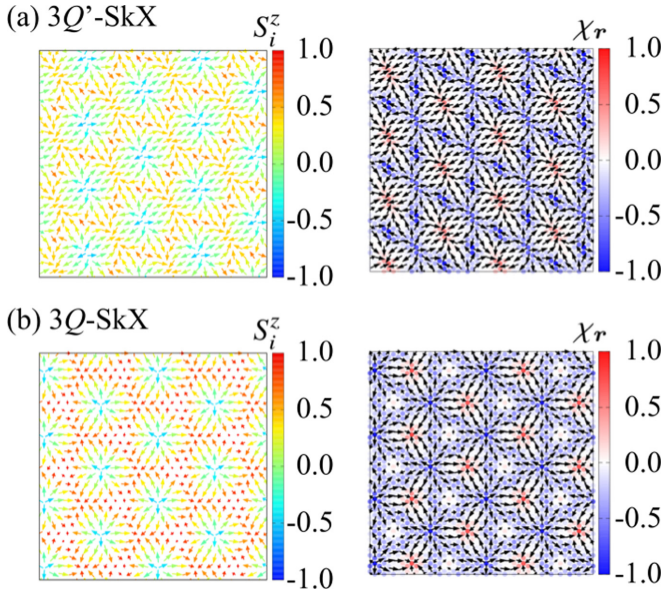


FIG. 11. Left panel: Snapshots of the spin configurations of (a) the $3Q'$ -SkX state at $H = 0.3$ and (b) the $3Q$ -SkX state at $H = 0.75$. The arrows and contours show the xy and z components of the spin, respectively. Right panel: The scalar chirality configurations corresponding to the spin configurations shown in the left panel.

is still an inconsistency in the high-field region; the $3Q$ -Ch state appears for $H \gtrsim 1.625$ corresponding to the $3Q$ -Ch state in the model with the interactions only at $\pm Q_1, \pm Q_2$, and $\pm Q_3$ in Sec. VC3, although the intensities of Q_1, Q_2 , and Q_3 components in the magnetic moments are slightly different in the present $3Q$ -Ch state. This result indicates that the interactions at other higher harmonics like $2Q_1 - Q_2$, which contributes to the energy in the $3Q'$ -Ch-II state [Fig. 8(c)], might be important in the high-field region.

The reason why the contribution from the interactions at $3Q_\eta$ is important is understood from the spiral modulation in the presence of anisotropic interactions. From the relation of $F_{Q_1}^x > F_{Q_1}^z (> F_{Q_1}^y)$, the spiral plane along the Q_1 direction is elliptically modulated so as to have more x -spin components. In a similar way, the multiple- Q states in Sec. VC2 consist of a superposition of the elliptical waves along the Q_1 - Q_3 directions. Such a deformation from the circular spiral plane to the elliptical spiral plane leads to the relatively large intensity at $3Q_\eta$, as shown by the dashed circles in the third column in Fig. 8. Thus, the interactions at $3Q_\eta$ play an important role in the present situation. Meanwhile, it is noted that the contribution at the $2Q_\eta$ channel is not important in spite of the larger value of λ_{2Q_η} than λ_{3Q_η} , since the $2Q_\eta$ modulation does not appear in the elliptical modulation under F_{Q_η} .

Furthermore, we investigate how a large contribution from the $3Q_\eta$ channel requires the stabilization of the $3Q'$ -Ch-II state by multiplying the variable $0 \leq r \leq 1$ by X_{3Q_η} . Figure 13 shows the r dependence of the uniform spin scalar chirality at $H = 0.7$. The result at $r = 0$ corresponds to that in Fig. 10, while the result at $r = 1$ corresponds to that in Fig. 12. The $3Q'$ -SkX state in the intermediate r has similar spin and chirality textures to those in Fig. 11(a). The result shows that the $3Q'$ -Ch-II state appears at $r \simeq 0.31$, which indicates

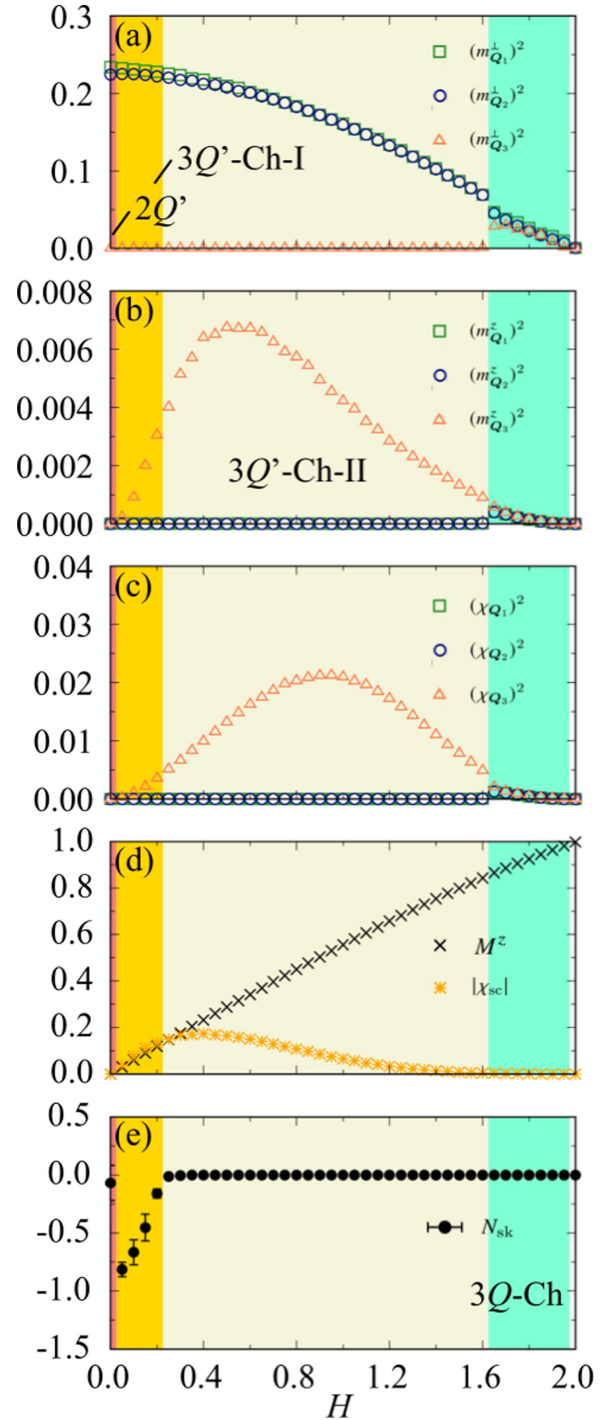


FIG. 12. H dependences of (a) $(m_{Q_1}^\perp)^2$, (b) $(m_{Q_2}^\perp)^2$, (c) $(\chi_{Q_\eta})^2$, (d) M^z and $|\chi_{sc}|$, and (e) N_{sk} in the model with the Q_η and $3Q_\eta$ channels. We sort $m_{Q_1}^\perp, m_{Q_2}^\perp$, and χ_{Q_η} to satisfy $m_{Q_1}^\perp \geq m_{Q_2}^\perp \geq m_{Q_3}^\perp$.

that relatively small $\lambda_{3Q_1} \gtrsim 0.31\lambda_{Q_1}$ leads to the stabilization (destabilization) of the $3Q'$ -Ch-II ($3Q'$ -SkX) state.

Finally, we find that the relationship of $F_{3Q_1}^x > F_{3Q_1}^y, F_{3Q_1}^z$ is also important. Indeed, when we perform the simulations by setting $F_{3Q_1}^y > F_{3Q_1}^x, F_{3Q_1}^z$ and $F_{3Q_1}^z > F_{3Q_1}^x, F_{3Q_1}^y$, while at the same time changing $3Q_2$ and $3Q_3$ channels to satisfy

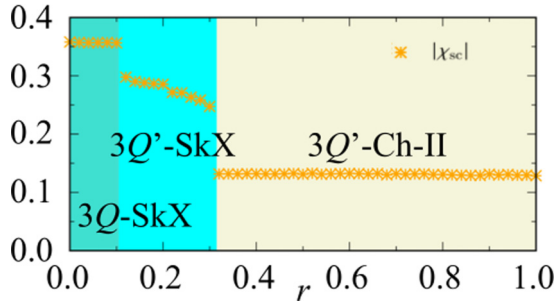


FIG. 13. r dependence of $|\chi_{sc}|$ in the model with $X_{Q\eta}$ and $rX_{3Q\eta}$ at $H = 0.7$.

the threefold rotational symmetry, we cannot reproduce the results in Fig. 7.

VI. SUMMARY AND PERSPECTIVE

To summarize, we formulated a systematic method of constructing the effective spin model with the momentum-resolved anisotropic exchange interactions based on two approaches in order to systematically understand multiple- Q instabilities. First, by performing magnetic representation analysis, we found the six symmetry rules to obtain nonzero momentum-resolved anisotropic exchange interactions in the primitive-lattice system. According to the rules, one can systematically construct the effective spin model in any primitive lattices. As a demonstration, we showed the effective spin models in the tetragonal, hexagonal, and trigonal crystal systems. We also found the symmetry rules in the multisublattice system and showed the effective spin model in the honeycomb and kagome structures. Second, by performing perturbation analysis, we found that the spin-dependent hybridizations between itinerant electron and localized electron states are important microscopic model parameters for nonzero long-range anisotropic exchange interactions in metals. The results beyond the symmetry argument provide a way to quantitatively evaluate the contributions of the anisotropic interactions in magnetic metals within the framework of first-principles calculations. Finally, we showed how to use the above general results by applying them to a hexagonal crystal and how the anisotropic interactions affect multiple- Q states by performing simulated annealing for the effective model. We found that a plethora of multiple- Q states with a spin scalar chirality are stabilized by the symmetric anisotropic exchange interactions at wave vectors that give the maximum of the magnetic susceptibility as well as those at their higher harmonics.

Our results will stimulate further exploration of materials hosting SkX. Based on the symmetry argument, one can construct the effective spin model and analyze possible SkXs stabilized by the anisotropic interactions once the crystal symmetry and the ordering vector are provided from the neutron and x-ray experiments. Therefore, the symmetry argument provides a reference for the exploration of further SkXs in both centrosymmetric and noncentrosymmetric magnets since our results show a complete relationship between the anisotropic exchange interaction and crystal symmetry in any crystal systems. In particular, the symmetry rules about the symmetric anisotropic interaction make it possible to search

centrosymmetric materials hosting SkXs, which have been less studied so far compared to noncentrosymmetric materials based on Moriya's rule.

In addition, our results will open up the possibility of exotic multiple- Q states beyond the SkXs. As various sets of anisotropic exchange interactions emerge depending on the crystal symmetry, there are several ways to stabilize different types of multiple- Q states. Indeed, we showed that the competition between interactions at different wave vectors leads to the emergence of unconventional multiple- Q state. These competitions might become a source of exotic multiple- Q states [92,93]. We also showed a variety of anisotropic exchange interactions in the multisublattice system, which become an origin of the sublattice-dependent SkX, such as the antiferromagnetic SkX. In addition, it is an intriguing problem to examine the role of thermal fluctuations in the momentum-space effective spin model since a recent theoretical study has revealed rich multiple- Q states in the magnetic-field-temperature phase diagram [114].

ACKNOWLEDGMENTS

The authors thank M. Yatsushiro and T. Matsumoto for the fruitful discussions. R.Y. thanks Y. Kato and Y. Motome for helpful comments on numerical methods. This research was supported by JSPS KAKENHI Grants No. JP19K03752, No. JP19H01834, No. JP21H01037, No. JP22H04468, and by JST PRESTO (JPMJPR20L8). R.Y. was supported by Forefront Physics and Mathematics Program to Drive Transformation (FoPM). R.Y. would like to acknowledge the support from the Mochizuki Fund of Yukawa Memorial Foundation. Parts of the numerical calculations were performed in the supercomputing systems in ISSP, the University of Tokyo.

APPENDIX A: MAGNETIC REPRESENTATION ANALYSIS

1. Primitive-lattice case

We show details of the magnetic representation analysis in Secs. II A 1 and II B 1. The \mathbf{q} -resolved anisotropic spin interaction in Eq. (2) is determined so as to satisfy the crystal symmetry as well as the time-reversal symmetry. In the following, we discuss the interaction matrix $X_{\mathbf{q}}$ in the gray symmorphic space group $\mathbf{M} = \mathbf{H} + \theta\mathbf{H}$ including the time-reversal operation θ , space group operations $\in \mathbf{H}$, and their product.

The time-reversal symmetry connecting $\pm\mathbf{q}$ imposes

$$\begin{aligned} X_{\mathbf{q}}^{\alpha\beta} &= \theta X_{-\mathbf{q}}^{\alpha\beta} \theta^{-1} \\ &= (X_{-\mathbf{q}}^{\alpha\beta})^*, \end{aligned} \quad (\text{A1})$$

where the property of the antilinearity of θ is used in the second line. From this symmetry constraint and the definition of $X_{\mathbf{q}}$ in Eq. (3), one obtains $\mathbf{D}_{\mathbf{q}} = -\mathbf{D}_{-\mathbf{q}}$, $\mathbf{E}_{\mathbf{q}} = \mathbf{E}_{-\mathbf{q}}$, and $\mathbf{F}_{\mathbf{q}} = \mathbf{F}_{-\mathbf{q}}$, which means that $\mathbf{D}_{\mathbf{q}}$ is antisymmetric in momentum space but $\mathbf{E}_{\mathbf{q}}$ and $\mathbf{F}_{\mathbf{q}}$ are symmetric.

We adopt point-group operations in momentum space as follows. Let us assume a crystal with a lattice vector \mathbf{R}_n and a point-group operation P of the crystal. Then, $P\mathbf{R}_n$ leaves the system invariant. Meanwhile, the crystal in momentum space is characterized by a reciprocal-lattice vector \mathbf{G}_m , where

PG_m leaves the system invariant. Thus, the same point-group operation P is present in both real and momentum spaces.

Since the anisotropic spin interaction, $S_q^T X_q S_{-q}$, is regarded as the interaction between two spins at reciprocal wave vector $\pm \mathbf{q}$, nonzero components in X_q are determined by the point-group operation leaving the “bond” connecting \mathbf{q} and $-\mathbf{q}$. There are two types of such operations, P^I and P^{II} , which are given by the following:

(I) Operation P^I satisfying $P^I \mathbf{q} = \mathbf{q}$.

(II) Operation P^{II} satisfying $P^{II} \mathbf{q} = -\mathbf{q}$.

In terms of the magnetic space group, these point-group operations form the magnetic little cogroup [113]. In other words, the anisotropic spin interaction in Eq. (2) must satisfy the magnetic little cogroup symmetry rather than the point-group symmetry, which is the reason why the anisotropic interaction depends on not only the crystal symmetry but also the wave vector \mathbf{q} (see Tables V–VII).

The symmetry constraints from point-group symmetry are obtained by dividing the symmetry operations into spin and momentum space (magnetic representation [98]). First, we rewrite the anisotropic spin interaction at $\pm \mathbf{q}$ as

$$S_q^T X_q S_{-q} + S_{-q}^T X_{-q} S_q = \tilde{S}^T \begin{pmatrix} 0 & X_q \\ X_q^* & 0 \end{pmatrix} \tilde{S}, \quad (\text{A2})$$

with

$$\tilde{S} = (S_q^{x_s}, S_q^{y_s}, S_q^{z_s}, S_{-q}^{x_s}, S_{-q}^{y_s}, S_{-q}^{z_s})^T. \quad (\text{A3})$$

Here, S_q^α is the classical spin (axial vector) at wave vector \mathbf{q} in the Cartesian coordinates $\alpha = (x_s, y_s, z_s)$, and X_q represents the 3×3 interaction matrix.

By using the magnetic representation $\Gamma(P)$ for the operation P , the symmetry constraint is obtained from

$$\begin{pmatrix} 0 & X_q \\ X_q^* & 0 \end{pmatrix} = \Gamma(P) \begin{pmatrix} 0 & X_q \\ X_q^* & 0 \end{pmatrix} \Gamma^{-1}(P). \quad (\text{A4})$$

$\Gamma(P)$ is given by

$$\Gamma(P) = \Gamma_{\text{perm}}(P) \otimes \Gamma_{\text{ax}}(P), \quad (\text{A5})$$

where 2×2 matrix $\Gamma_{\text{perm}}(P)$ is the permutation representation for \mathbf{q} and $-\mathbf{q}$, and 3×3 matrix $\Gamma_{\text{ax}}(P)$ is the axial vector representation for the three spin components. The permutation representation Γ_{perm}^I for any type I operations is defined as $P^I(\mathbf{q}, -\mathbf{q}) = (\mathbf{q}, -\mathbf{q}) \Gamma_{\text{perm}}^I = (\mathbf{q}, -\mathbf{q})$, while $\Gamma_{\text{perm}}^{II}$ for any type II operations is defined as $P^{II}(\mathbf{q}, -\mathbf{q}) = (\mathbf{q}, -\mathbf{q}) \Gamma_{\text{perm}}^{II} = (-\mathbf{q}, \mathbf{q})$. Then, Γ_{perm} is explicitly given by

$$\Gamma_{\text{perm}}^I = \begin{pmatrix} 1 & 0 \\ 0 & 1 \end{pmatrix}, \quad \Gamma_{\text{perm}}^{II} = \begin{pmatrix} 0 & 1 \\ 1 & 0 \end{pmatrix}. \quad (\text{A6})$$

Meanwhile, The axial vector representation is defined as $\Gamma_{\text{ax}}(P)_{\alpha\beta} = \langle \alpha | P | \beta \rangle$ ($\alpha, \beta = x_s, y_s, z_s$), where $|\alpha\rangle$ is the basis in classical spin space (axial vector space).

Then, the rules (a)–(f) in Sec. II A 1 are obtained from the following magnetic representations by setting $|x_s\rangle \parallel \mathbf{q}$:

(A) The representation of the space inversion center corresponding to Fig. 1(a) is given by

$$\Gamma_{\text{perm}}^{II} \otimes \begin{pmatrix} 1 & 0 & 0 \\ 0 & 1 & 0 \\ 0 & 0 & 1 \end{pmatrix}. \quad (\text{A7})$$

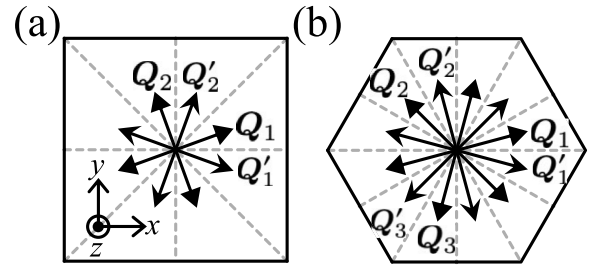


FIG. 14. A set of low symmetric wave vectors along the low symmetric lines inside the first Brillouin zone in (a) tetragonal crystal systems and (b) hexagonal and trigonal crystal systems. The dashed lines represent the high symmetric lines. In (a), Q_1 and Q_2 (Q'_1 and Q'_2) are connected by the fourfold rotation around the z axis, while in (b), Q_1 , Q_2 , and Q_3 (Q'_1 , Q'_2 , and Q'_3) are connected by the threefold rotation. Q_1 and Q'_1 are connected by the twofold rotation around the x axis, the mirror reflection on the xz plane, the time-reversal operation after the twofold rotation around the y axis, or the time-reversal operation after the mirror reflection on the yz plane. The wave vectors in $\{Q\}$ lie on the xy plane.

(B) The representation of the mirror plane perpendicular to \mathbf{q} corresponding to Fig. 1(b) is given by

$$\Gamma_{\text{perm}}^{II} \otimes \begin{pmatrix} 1 & 0 & 0 \\ 0 & -1 & 0 \\ 0 & 0 & -1 \end{pmatrix}. \quad (\text{A8})$$

(C) The representation of the twofold axis perpendicular to \mathbf{q} corresponding to Fig. 1(c) is given by

$$\Gamma_{\text{perm}}^{II} \otimes \begin{pmatrix} -1 & 0 & 0 \\ 0 & -1 & 0 \\ 0 & 0 & 1 \end{pmatrix}, \quad (\text{A9})$$

where the direction of $|z_s\rangle$ is parallel to the axis.

(D) The representation of the mirror plane including \mathbf{q} corresponding to Fig. 1(d) is given by

$$\Gamma_{\text{perm}}^I \otimes \begin{pmatrix} -1 & 0 & 0 \\ 0 & -1 & 0 \\ 0 & 0 & 1 \end{pmatrix}, \quad (\text{A10})$$

where the direction of $|z_s\rangle$ is perpendicular to the mirror plane.

(E) The representation of the twofold axis including \mathbf{q} corresponding to Fig. 1(e) is given by

$$\Gamma_{\text{perm}}^I \otimes \begin{pmatrix} 1 & 0 & 0 \\ 0 & -1 & 0 \\ 0 & 0 & -1 \end{pmatrix}. \quad (\text{A11})$$

(F) The representation of the n -fold ($n = 3, 4, 6$) axis including \mathbf{q} corresponding to Fig. 1(f) is given by

$$\Gamma_{\text{perm}}^I \otimes \begin{pmatrix} 1 & 0 & 0 \\ 0 & \cos \phi & -\sin \phi \\ 0 & \sin \phi & \cos \phi \end{pmatrix}, \quad (\text{A12})$$

with $\phi = 2\pi/n$.

Since the operation P in the rules (a)–(c) [(d)–(f)] is the type II (I), the rules (a)–(c) [(d)–(f)] are obtained from $X_q = \Gamma_{\text{ax}}(P) X_q^* \Gamma_{\text{ax}}^{-1}(P)$ [$X_q = \Gamma_{\text{ax}}(P) X_q \Gamma_{\text{ax}}^{-1}(P)$]. Thus, the rules (a)–(c) [(d) and (e)] are imposed by the point-group operation

TABLE IX. Interaction matrices $X_{\mathbf{Q}_1}$ and $X_{\mathbf{Q}'_1}$ and the number of independent components N_c in the tetragonal crystal systems for the low symmetric wave vectors \mathbf{Q}_1 and \mathbf{Q}'_1 shown in Fig. 14(a). The spin coordinates x_s , y_s , and z_s are taken along the x , y , and z directions in Fig. 14(a), respectively.

Space group \mathbf{H}	\mathbf{Q}_1		\mathbf{Q}'_1	
	$X_{\mathbf{Q}_1}$	N_c	$X_{\mathbf{Q}'_1}$	N_c
$P4/mmm$	$\begin{pmatrix} F_{\mathbf{Q}_1}^x & E_{\mathbf{Q}_1}^z & 0 \\ E_{\mathbf{Q}_1}^z & F_{\mathbf{Q}_1}^y & 0 \\ 0 & 0 & F_{\mathbf{Q}_1}^z \end{pmatrix}$	4	$\begin{pmatrix} F_{\mathbf{Q}'_1}^x & -E_{\mathbf{Q}'_1}^z & 0 \\ -E_{\mathbf{Q}'_1}^z & F_{\mathbf{Q}'_1}^y & 0 \\ 0 & 0 & F_{\mathbf{Q}'_1}^z \end{pmatrix}$	0
$P422$	$\begin{pmatrix} F_{\mathbf{Q}_1}^x & E_{\mathbf{Q}_1}^z & -iD_{\mathbf{Q}_1}^y \\ E_{\mathbf{Q}_1}^z & F_{\mathbf{Q}_1}^y & iD_{\mathbf{Q}_1}^x \\ iD_{\mathbf{Q}_1}^y & -iD_{\mathbf{Q}_1}^x & F_{\mathbf{Q}_1}^z \end{pmatrix}$	6	$\begin{pmatrix} F_{\mathbf{Q}'_1}^x & -E_{\mathbf{Q}'_1}^z & iD_{\mathbf{Q}'_1}^y \\ -E_{\mathbf{Q}'_1}^z & F_{\mathbf{Q}'_1}^y & iD_{\mathbf{Q}'_1}^x \\ -iD_{\mathbf{Q}'_1}^y & -iD_{\mathbf{Q}'_1}^x & F_{\mathbf{Q}'_1}^z \end{pmatrix}$	0
$P\bar{4}2m$	$\begin{pmatrix} F_{\mathbf{Q}_1}^x & E_{\mathbf{Q}_1}^z & -iD_{\mathbf{Q}_1}^y \\ E_{\mathbf{Q}_1}^z & F_{\mathbf{Q}_1}^y & iD_{\mathbf{Q}_1}^x \\ iD_{\mathbf{Q}_1}^y & -iD_{\mathbf{Q}_1}^x & F_{\mathbf{Q}_1}^z \end{pmatrix}$	6	$\begin{pmatrix} F_{\mathbf{Q}'_1}^x & -E_{\mathbf{Q}'_1}^z & iD_{\mathbf{Q}'_1}^y \\ -E_{\mathbf{Q}'_1}^z & F_{\mathbf{Q}'_1}^y & iD_{\mathbf{Q}'_1}^x \\ -iD_{\mathbf{Q}'_1}^y & -iD_{\mathbf{Q}'_1}^x & F_{\mathbf{Q}'_1}^z \end{pmatrix}$	0
$P\bar{4}m2$	$\begin{pmatrix} F_{\mathbf{Q}_1}^x & E_{\mathbf{Q}_1}^z & -iD_{\mathbf{Q}_1}^y \\ E_{\mathbf{Q}_1}^z & F_{\mathbf{Q}_1}^y & iD_{\mathbf{Q}_1}^x \\ iD_{\mathbf{Q}_1}^y & -iD_{\mathbf{Q}_1}^x & F_{\mathbf{Q}_1}^z \end{pmatrix}$	6	$\begin{pmatrix} F_{\mathbf{Q}'_1}^x & -E_{\mathbf{Q}'_1}^z & -iD_{\mathbf{Q}'_1}^y \\ -E_{\mathbf{Q}'_1}^z & F_{\mathbf{Q}'_1}^y & -iD_{\mathbf{Q}'_1}^x \\ iD_{\mathbf{Q}'_1}^y & iD_{\mathbf{Q}'_1}^x & F_{\mathbf{Q}'_1}^z \end{pmatrix}$	0
$P4mm$	$\begin{pmatrix} F_{\mathbf{Q}_1}^x & E_{\mathbf{Q}_1}^z & -iD_{\mathbf{Q}_1}^y \\ E_{\mathbf{Q}_1}^z & F_{\mathbf{Q}_1}^y & iD_{\mathbf{Q}_1}^x \\ iD_{\mathbf{Q}_1}^y & -iD_{\mathbf{Q}_1}^x & F_{\mathbf{Q}_1}^z \end{pmatrix}$	6	$\begin{pmatrix} F_{\mathbf{Q}'_1}^x & -E_{\mathbf{Q}'_1}^z & -iD_{\mathbf{Q}'_1}^y \\ -E_{\mathbf{Q}'_1}^z & F_{\mathbf{Q}'_1}^y & -iD_{\mathbf{Q}'_1}^x \\ iD_{\mathbf{Q}'_1}^y & iD_{\mathbf{Q}'_1}^x & F_{\mathbf{Q}'_1}^z \end{pmatrix}$	0
$P4/m$	$\begin{pmatrix} F_{\mathbf{Q}_1}^x & E_{\mathbf{Q}_1}^z & 0 \\ E_{\mathbf{Q}_1}^z & F_{\mathbf{Q}_1}^y & 0 \\ 0 & 0 & F_{\mathbf{Q}_1}^z \end{pmatrix}$	4	$\begin{pmatrix} F_{\mathbf{Q}'_1}^x & E_{\mathbf{Q}'_1}^z & 0 \\ E_{\mathbf{Q}'_1}^z & F_{\mathbf{Q}'_1}^y & 0 \\ 0 & 0 & F_{\mathbf{Q}'_1}^z \end{pmatrix}$	4
$P4$	$\begin{pmatrix} F_{\mathbf{Q}_1}^x & E_{\mathbf{Q}_1}^z & -iD_{\mathbf{Q}_1}^y \\ E_{\mathbf{Q}_1}^z & F_{\mathbf{Q}_1}^y & iD_{\mathbf{Q}_1}^x \\ iD_{\mathbf{Q}_1}^y & -iD_{\mathbf{Q}_1}^x & F_{\mathbf{Q}_1}^z \end{pmatrix}$	6	$\begin{pmatrix} F_{\mathbf{Q}'_1}^x & E_{\mathbf{Q}'_1}^z & -iD_{\mathbf{Q}'_1}^y \\ E_{\mathbf{Q}'_1}^z & F_{\mathbf{Q}'_1}^y & iD_{\mathbf{Q}'_1}^x \\ iD_{\mathbf{Q}'_1}^y & -iD_{\mathbf{Q}'_1}^x & F_{\mathbf{Q}'_1}^z \end{pmatrix}$	6
$P\bar{4}$	$\begin{pmatrix} F_{\mathbf{Q}_1}^x & E_{\mathbf{Q}_1}^z & -iD_{\mathbf{Q}_1}^y \\ E_{\mathbf{Q}_1}^z & F_{\mathbf{Q}_1}^y & iD_{\mathbf{Q}_1}^x \\ iD_{\mathbf{Q}_1}^y & -iD_{\mathbf{Q}_1}^x & F_{\mathbf{Q}_1}^z \end{pmatrix}$	6	$\begin{pmatrix} F_{\mathbf{Q}'_1}^x & E_{\mathbf{Q}'_1}^z & -iD_{\mathbf{Q}'_1}^y \\ E_{\mathbf{Q}'_1}^z & F_{\mathbf{Q}'_1}^y & iD_{\mathbf{Q}'_1}^x \\ iD_{\mathbf{Q}'_1}^y & -iD_{\mathbf{Q}'_1}^x & F_{\mathbf{Q}'_1}^z \end{pmatrix}$	6

(not) combined with the time-reversal operation, which results in the different (same) nonzero components of \mathbf{E}_q and \mathbf{D}_q . In the magnetic representations (A)–(E), the axial vector representations do not have the off-diagonal components, which results in no constraint on \mathbf{F}_q .

In Sec. II B 1, we use the axial vector representation by setting $|x_s\rangle \parallel |x\rangle$, $|y_s\rangle \parallel |y\rangle$, and $|z_s\rangle \parallel |z\rangle$, where $(|x\rangle, |y\rangle, |z\rangle)$ is the basis set of the crystal lattice shown in Fig. 2(a). Then, the axial vector representation has the off-diagonal components depending on the symmetry of the space group and the wave vector, which results in different constraints on the interactions. Equation (11) is obtained by using the permutation representation for $(\pm\mathbf{Q}_1, \pm\mathbf{Q}_2)$ or $(\pm\mathbf{Q}_1, \pm\mathbf{Q}_2, \pm\mathbf{Q}_3)$ space.

2. Multisublattice case

Similar to the primitive-lattice case, we rewrite the interaction in Eq. (7) in an extended space. For example, we show here the two-sublattice case, where the interaction is given by

$$\tilde{\mathbf{S}}^T \begin{pmatrix} 0 & \mathcal{X}_{AA;q} & 0 & \mathcal{X}_{AB;q} \\ \mathcal{X}_{AA;q}^* & 0 & \mathcal{X}_{AB;q}^* & 0 \\ 0 & \mathcal{X}_{AB;q}^* & 0 & \mathcal{X}_{BB;q} \\ \mathcal{X}_{AB;q} & 0 & \mathcal{X}_{BB;q}^* & 0 \end{pmatrix} \tilde{\mathbf{S}}, \quad (\text{A13})$$

with

$$\tilde{\mathbf{S}} = (S_{Aq}, S_{A-q}, S_{Bq}, S_{B-q})^T. \quad (\text{A14})$$

The symmetry constraint is obtained by using the magnetic representation $\Gamma(P)$ for the operation P , which is given by

$$\Gamma(P) = \Gamma_{\text{sub}}(P) \otimes \Gamma_{\text{perm}}(P) \otimes \Gamma_{\text{ax}}(P). \quad (\text{A15})$$

Here, 2×2 matrix $\Gamma_{\text{sub}}(P)$ is the permutation representation for the sublattices A and B, 2×2 matrix $\Gamma_{\text{perm}}(P)$ is the permutation representation for \mathbf{q} and $-\mathbf{q}$, and 3×3 matrix $\Gamma_{\text{ax}}(P)$ is the axial vector representation for the three spin components. $\Gamma_{\text{perm}}(P)$ and $\Gamma_{\text{ax}}(P)$ are given in the previous section. As mentioned in Sec. II A 2, the symmetry constraint is imposed by the point-group symmetry (i) fixing or (ii) interchanging the sublattices A and B. In terms of the magnetic representation, the case (i) and (ii) point-group symmetry is represented by using

$$\Gamma_{\text{sub}}^I = \begin{pmatrix} 1 & 0 \\ 0 & 1 \end{pmatrix}, \Gamma_{\text{sub}}^{II} = \begin{pmatrix} 0 & 1 \\ 1 & 0 \end{pmatrix}, \quad (\text{A16})$$

respectively.

In the n -sublattice ($n \geq 3$) case, the symmetry constraints are obtained as well as the two-sublattice case. Then, the interaction matrix is written in extended space with

$$\tilde{S} = (S_{Aq}, S_{A-q}, S_{Bq}, S_{B-q}, \dots, S_{nq}, S_{n-q})^T. \quad (\text{A17})$$

The magnetic representation is common to Eq. (A15), where only Γ_{sub} depends on the number of sublattices. For example, in the three-sublattice case, the symmetry constraint is imposed by the point-group symmetry that (i) fixes the sublattices A, B, and C; (ii) interchanges the sublattices A and B but fixes the sublattice C; and (iii) cyclically interchanges the sublattices A, B, and C. The corresponding representations are given by

$$\Gamma_{\text{sub}}^{(\text{i})} = \begin{pmatrix} 1 & 0 & 0 \\ 0 & 1 & 0 \\ 0 & 0 & 1 \end{pmatrix}, \quad \Gamma_{\text{sub}}^{(\text{ii})} = \begin{pmatrix} 0 & 1 & 0 \\ 1 & 0 & 0 \\ 0 & 0 & 1 \end{pmatrix},$$

$$\Gamma_{\text{sub}}^{(\text{iii})} = \begin{pmatrix} 0 & 1 & 0 \\ 0 & 0 & 1 \\ 1 & 0 & 0 \end{pmatrix}. \quad (\text{A18})$$

TABLE X. Interaction matrices X_{Q_1} and $X_{Q'_1}$ and the number of independent components N_c in the hexagonal crystal systems for the low symmetric wave vectors Q_1 and Q'_1 shown in Fig. 14(b). The spin coordinates x_s, y_s , and z_s are taken along the x, y , and z directions in Fig. 14(a), respectively.

Space group H	Q_1	N_c	Q'_1	N_c
	X_{Q_1}		$X_{Q'_1}$	
$P6/mmm$	$\begin{pmatrix} F_{Q_1}^x & E_{Q_1}^z & 0 \\ E_{Q_1}^z & F_{Q_1}^y & 0 \\ 0 & 0 & F_{Q_1}^z \end{pmatrix}$	4	$\begin{pmatrix} F_{Q_1}^x & -E_{Q_1}^z & 0 \\ -E_{Q_1}^z & F_{Q_1}^y & 0 \\ 0 & 0 & F_{Q_1}^z \end{pmatrix}$	0
$P622$	$\begin{pmatrix} F_{Q_1}^x & E_{Q_1}^z & -iD_{Q_1}^y \\ E_{Q_1}^z & F_{Q_1}^y & iD_{Q_1}^x \\ iD_{Q_1}^y & -iD_{Q_1}^x & F_{Q_1}^z \end{pmatrix}$	6	$\begin{pmatrix} F_{Q_1}^x & -E_{Q_1}^z & iD_{Q_1}^y \\ -E_{Q_1}^z & F_{Q_1}^y & iD_{Q_1}^x \\ -iD_{Q_1}^y & -iD_{Q_1}^x & F_{Q_1}^z \end{pmatrix}$	0
$P\bar{6}m2$	$\begin{pmatrix} F_{Q_1}^x & E_{Q_1}^z + iD_{Q_1}^z & 0 \\ E_{Q_1}^z & -iD_{Q_1}^z & F_{Q_1}^y \\ 0 & 0 & F_{Q_1}^z \end{pmatrix}$	5	$\begin{pmatrix} F_{Q_1}^x & -E_{Q_1}^z + iD_{Q_1}^z & 0 \\ -E_{Q_1}^z & -iD_{Q_1}^z & F_{Q_1}^y \\ 0 & 0 & F_{Q_1}^z \end{pmatrix}$	0
$P\bar{6}2m$	$\begin{pmatrix} F_{Q_1}^x & E_{Q_1}^z + iD_{Q_1}^z & 0 \\ E_{Q_1}^z & -iD_{Q_1}^z & F_{Q_1}^y \\ 0 & 0 & F_{Q_1}^z \end{pmatrix}$	5	$\begin{pmatrix} F_{Q_1}^x & -E_{Q_1}^z - iD_{Q_1}^z & 0 \\ -E_{Q_1}^z & -iD_{Q_1}^z & F_{Q_1}^y \\ 0 & 0 & F_{Q_1}^z \end{pmatrix}$	0
$P6mm$	$\begin{pmatrix} F_{Q_1}^x & E_{Q_1}^z & -iD_{Q_1}^y \\ E_{Q_1}^z & F_{Q_1}^y & iD_{Q_1}^x \\ iD_{Q_1}^y & -iD_{Q_1}^x & F_{Q_1}^z \end{pmatrix}$	6	$\begin{pmatrix} F_{Q_1}^x & -E_{Q_1}^z & -iD_{Q_1}^y \\ -E_{Q_1}^z & F_{Q_1}^y & -iD_{Q_1}^x \\ iD_{Q_1}^y & iD_{Q_1}^x & F_{Q_1}^z \end{pmatrix}$	0
$P6/m$	$\begin{pmatrix} F_{Q_1}^x & E_{Q_1}^z & 0 \\ E_{Q_1}^z & F_{Q_1}^y & 0 \\ 0 & 0 & F_{Q_1}^z \end{pmatrix}$	4	$\begin{pmatrix} F_{Q_1}^x & E_{Q_1}^z & 0 \\ E_{Q_1}^z & F_{Q_1}^y & 0 \\ 0 & 0 & F_{Q_1}^z \end{pmatrix}$	4
$P\bar{6}$	$\begin{pmatrix} F_{Q_1}^x & E_{Q_1}^z + iD_{Q_1}^z & 0 \\ E_{Q_1}^z & -iD_{Q_1}^z & F_{Q_1}^y \\ 0 & 0 & F_{Q_1}^z \end{pmatrix}$	5	$\begin{pmatrix} F_{Q_1}^x & E_{Q_1}^z + iD_{Q_1}^z & 0 \\ E_{Q_1}^z & -iD_{Q_1}^z & F_{Q_1}^y \\ 0 & 0 & F_{Q_1}^z \end{pmatrix}$	5
$P6$	$\begin{pmatrix} F_{Q_1}^x & E_{Q_1}^z & -iD_{Q_1}^y \\ E_{Q_1}^z & F_{Q_1}^y & iD_{Q_1}^x \\ iD_{Q_1}^y & -iD_{Q_1}^x & F_{Q_1}^z \end{pmatrix}$	6	$\begin{pmatrix} F_{Q_1}^x & E_{Q_1}^z & -iD_{Q_1}^y \\ E_{Q_1}^z & F_{Q_1}^y & iD_{Q_1}^x \\ iD_{Q_1}^y & -iD_{Q_1}^x & F_{Q_1}^z \end{pmatrix}$	6

It is noted that the point-group symmetry belonging to the same class as the point-group symmetry (i)–(iii) also imposes the symmetry constraint.

APPENDIX B: EFFECTIVE SPIN MODEL WITH THE INTERACTIONS AT LOW SYMMETRIC WAVE VECTORS IN TETRAGONAL, HEXAGONAL, AND TRIGONAL CRYSTAL SYSTEMS

We present here the model in Eq. (10) with the low symmetric wave vectors in tetragonal, hexagonal, and trigonal crystal systems. Figure 14(a) [14(b)] shows the schematic pictures of the low symmetric wave vectors for the tetragonal (hexagonal and trigonal) crystal systems. In the $P4/mmm$, $P422$, $P42m$, $P4m2$, and $P4mm$ ($P4/m$, $P4$, and $P\bar{4}$) crystals, there are four (two) equivalent wave vectors Q_1 , Q_2 , Q'_1 , and Q'_2 (Q_1 and Q_2) connected by the crystal symmetry; the effective spin model in Eq. (10) is described as having the interactions at $\{Q\} = \{\pm Q_1, \pm Q_2, \pm Q'_1, \pm Q'_2\}$ ($\{Q\} = \{\pm Q_1, \pm Q_2\}$ or $\{\pm Q'_1, \pm Q'_2\}$). Meanwhile, in the $P6/mmm$, $P622$, $P\bar{6}m2$, $P\bar{6}2m$, $P6mm$, $P\bar{3}m1$, $P\bar{3}1m$, $P321$, $P312$, and $P3m1$ ($P6/m$, $P\bar{6}$, $P6$, $P\bar{3}$, and $P3$) crystals, there are six (three) equivalent wave vectors Q_1 , Q_2 , Q_3 , Q'_1 , Q'_2 , and Q'_3 (Q_1 , Q_2 , and Q_3) connected by the crystal

TABLE XI. Interaction matrices $X_{\mathbf{Q}_1}$ and $X_{\mathbf{Q}'_1}$ and the number of independent components N_c in the trigonal crystal systems for the low symmetric wave vectors \mathbf{Q}_1 and \mathbf{Q}'_1 shown in Fig. 14(b). The spin coordinates x_s , y_s , and z_s are taken along the x , y , and z directions in Fig. 14(a), respectively.

Space group \mathbf{H}	\mathcal{Q}_1		N_c	\mathcal{Q}'_1		N_c
	$X_{\mathcal{Q}_1}$			$X_{\mathcal{Q}'_1}$		
$P\bar{3}m1$	$\begin{pmatrix} F_{\mathcal{Q}_1}^x & E_{\mathcal{Q}_1}^z & E_{\mathcal{Q}_1}^y \\ E_{\mathcal{Q}_1}^z & F_{\mathcal{Q}_1}^y & E_{\mathcal{Q}_1}^x \\ E_{\mathcal{Q}_1}^y & E_{\mathcal{Q}_1}^x & F_{\mathcal{Q}_1}^z \end{pmatrix}$		6	$\begin{pmatrix} F_{\mathcal{Q}'_1}^x & -E_{\mathcal{Q}'_1}^z & -E_{\mathcal{Q}'_1}^y \\ -E_{\mathcal{Q}'_1}^z & F_{\mathcal{Q}'_1}^y & E_{\mathcal{Q}'_1}^x \\ -E_{\mathcal{Q}'_1}^y & E_{\mathcal{Q}'_1}^x & F_{\mathcal{Q}'_1}^z \end{pmatrix}$		0
$P\bar{3}1m$	$\begin{pmatrix} F_{\mathcal{Q}_1}^x & E_{\mathcal{Q}_1}^z & E_{\mathcal{Q}_1}^y \\ E_{\mathcal{Q}_1}^z & F_{\mathcal{Q}_1}^y & E_{\mathcal{Q}_1}^x \\ E_{\mathcal{Q}_1}^y & E_{\mathcal{Q}_1}^x & F_{\mathcal{Q}_1}^z \end{pmatrix}$		6	$\begin{pmatrix} F_{\mathcal{Q}'_1}^x & -E_{\mathcal{Q}'_1}^z & E_{\mathcal{Q}'_1}^y \\ -E_{\mathcal{Q}'_1}^z & F_{\mathcal{Q}'_1}^y & -E_{\mathcal{Q}'_1}^x \\ E_{\mathcal{Q}'_1}^y & -E_{\mathcal{Q}'_1}^x & F_{\mathcal{Q}'_1}^z \end{pmatrix}$		0
$P321$	$\begin{pmatrix} F_{\mathcal{Q}_1}^x & E_{\mathcal{Q}_1}^z + iD_{\mathcal{Q}_1}^z & E_{\mathcal{Q}_1}^y - iD_{\mathcal{Q}_1}^y \\ E_{\mathcal{Q}_1}^z - iD_{\mathcal{Q}_1}^z & F_{\mathcal{Q}_1}^y & E_{\mathcal{Q}_1}^x + iD_{\mathcal{Q}_1}^x \\ E_{\mathcal{Q}_1}^y + iD_{\mathcal{Q}_1}^y & E_{\mathcal{Q}_1}^x - iD_{\mathcal{Q}_1}^x & F_{\mathcal{Q}_1}^z \end{pmatrix}$		9	$\begin{pmatrix} F_{\mathcal{Q}'_1}^x & -E_{\mathcal{Q}'_1}^z - iD_{\mathcal{Q}'_1}^z & -E_{\mathcal{Q}'_1}^y + iD_{\mathcal{Q}'_1}^y \\ -E_{\mathcal{Q}'_1}^z + iD_{\mathcal{Q}'_1}^z & F_{\mathcal{Q}'_1}^y & E_{\mathcal{Q}'_1}^x + iD_{\mathcal{Q}'_1}^x \\ -E_{\mathcal{Q}'_1}^y - iD_{\mathcal{Q}'_1}^y & E_{\mathcal{Q}'_1}^x - iD_{\mathcal{Q}'_1}^x & F_{\mathcal{Q}'_1}^z \end{pmatrix}$		0
$P312$	$\begin{pmatrix} F_{\mathcal{Q}_1}^x & E_{\mathcal{Q}_1}^z + iD_{\mathcal{Q}_1}^z & E_{\mathcal{Q}_1}^y - iD_{\mathcal{Q}_1}^y \\ E_{\mathcal{Q}_1}^z - iD_{\mathcal{Q}_1}^z & F_{\mathcal{Q}_1}^y & E_{\mathcal{Q}_1}^x + iD_{\mathcal{Q}_1}^x \\ E_{\mathcal{Q}_1}^y + iD_{\mathcal{Q}_1}^y & E_{\mathcal{Q}_1}^x - iD_{\mathcal{Q}_1}^x & F_{\mathcal{Q}_1}^z \end{pmatrix}$		9	$\begin{pmatrix} F_{\mathcal{Q}'_1}^x & -E_{\mathcal{Q}'_1}^z + iD_{\mathcal{Q}'_1}^z & E_{\mathcal{Q}'_1}^y + iD_{\mathcal{Q}'_1}^y \\ -E_{\mathcal{Q}'_1}^z - iD_{\mathcal{Q}'_1}^z & F_{\mathcal{Q}'_1}^y & -E_{\mathcal{Q}'_1}^x + iD_{\mathcal{Q}'_1}^x \\ E_{\mathcal{Q}'_1}^y - iD_{\mathcal{Q}'_1}^y & -E_{\mathcal{Q}'_1}^x - iD_{\mathcal{Q}'_1}^x & F_{\mathcal{Q}'_1}^z \end{pmatrix}$		0
$P3m1$	$\begin{pmatrix} F_{\mathcal{Q}_1}^x & E_{\mathcal{Q}_1}^z + iD_{\mathcal{Q}_1}^z & E_{\mathcal{Q}_1}^y - iD_{\mathcal{Q}_1}^y \\ E_{\mathcal{Q}_1}^z - iD_{\mathcal{Q}_1}^z & F_{\mathcal{Q}_1}^y & E_{\mathcal{Q}_1}^x + iD_{\mathcal{Q}_1}^x \\ E_{\mathcal{Q}_1}^y + iD_{\mathcal{Q}_1}^y & E_{\mathcal{Q}_1}^x - iD_{\mathcal{Q}_1}^x & F_{\mathcal{Q}_1}^z \end{pmatrix}$		9	$\begin{pmatrix} F_{\mathcal{Q}'_1}^x & -E_{\mathcal{Q}'_1}^z + iD_{\mathcal{Q}'_1}^z & -E_{\mathcal{Q}'_1}^y - iD_{\mathcal{Q}'_1}^y \\ -E_{\mathcal{Q}'_1}^z - iD_{\mathcal{Q}'_1}^z & F_{\mathcal{Q}'_1}^y & E_{\mathcal{Q}'_1}^x - iD_{\mathcal{Q}'_1}^x \\ -E_{\mathcal{Q}'_1}^y + iD_{\mathcal{Q}'_1}^y & E_{\mathcal{Q}'_1}^x + iD_{\mathcal{Q}'_1}^x & F_{\mathcal{Q}'_1}^z \end{pmatrix}$		0
$P31m$	$\begin{pmatrix} F_{\mathcal{Q}_1}^x & E_{\mathcal{Q}_1}^z + iD_{\mathcal{Q}_1}^z & E_{\mathcal{Q}_1}^y - iD_{\mathcal{Q}_1}^y \\ E_{\mathcal{Q}_1}^z - iD_{\mathcal{Q}_1}^z & F_{\mathcal{Q}_1}^y & E_{\mathcal{Q}_1}^x + iD_{\mathcal{Q}_1}^x \\ E_{\mathcal{Q}_1}^y + iD_{\mathcal{Q}_1}^y & E_{\mathcal{Q}_1}^x - iD_{\mathcal{Q}_1}^x & F_{\mathcal{Q}_1}^z \end{pmatrix}$		9	$\begin{pmatrix} F_{\mathcal{Q}'_1}^x & -E_{\mathcal{Q}'_1}^z - iD_{\mathcal{Q}'_1}^z & E_{\mathcal{Q}'_1}^y - iD_{\mathcal{Q}'_1}^y \\ -E_{\mathcal{Q}'_1}^z + iD_{\mathcal{Q}'_1}^z & F_{\mathcal{Q}'_1}^y & -E_{\mathcal{Q}'_1}^x - iD_{\mathcal{Q}'_1}^x \\ E_{\mathcal{Q}'_1}^y + iD_{\mathcal{Q}'_1}^y & -E_{\mathcal{Q}'_1}^x + iD_{\mathcal{Q}'_1}^x & F_{\mathcal{Q}'_1}^z \end{pmatrix}$		0
$P\bar{3}$	$\begin{pmatrix} F_{\mathcal{Q}_1}^x & E_{\mathcal{Q}_1}^z & E_{\mathcal{Q}_1}^y \\ E_{\mathcal{Q}_1}^z & F_{\mathcal{Q}_1}^y & E_{\mathcal{Q}_1}^x \\ E_{\mathcal{Q}_1}^y & E_{\mathcal{Q}_1}^x & F_{\mathcal{Q}_1}^z \end{pmatrix}$		6	$\begin{pmatrix} F_{\mathcal{Q}'_1}^x & E_{\mathcal{Q}'_1}^z & E_{\mathcal{Q}'_1}^y \\ E_{\mathcal{Q}'_1}^z & F_{\mathcal{Q}'_1}^y & E_{\mathcal{Q}'_1}^x \\ E_{\mathcal{Q}'_1}^y & E_{\mathcal{Q}'_1}^x & F_{\mathcal{Q}'_1}^z \end{pmatrix}$		6
$P3$	$\begin{pmatrix} F_{\mathcal{Q}_1}^x & E_{\mathcal{Q}_1}^z + iD_{\mathcal{Q}_1}^z & E_{\mathcal{Q}_1}^y - iD_{\mathcal{Q}_1}^y \\ E_{\mathcal{Q}_1}^z - iD_{\mathcal{Q}_1}^z & F_{\mathcal{Q}_1}^y & E_{\mathcal{Q}_1}^x + iD_{\mathcal{Q}_1}^x \\ E_{\mathcal{Q}_1}^y + iD_{\mathcal{Q}_1}^y & E_{\mathcal{Q}_1}^x - iD_{\mathcal{Q}_1}^x & F_{\mathcal{Q}_1}^z \end{pmatrix}$		9	$\begin{pmatrix} F_{\mathcal{Q}'_1}^x & E_{\mathcal{Q}'_1}^z + iD_{\mathcal{Q}'_1}^z & E_{\mathcal{Q}'_1}^y - iD_{\mathcal{Q}'_1}^y \\ E_{\mathcal{Q}'_1}^z - iD_{\mathcal{Q}'_1}^z & F_{\mathcal{Q}'_1}^y & E_{\mathcal{Q}'_1}^x + iD_{\mathcal{Q}'_1}^x \\ E_{\mathcal{Q}'_1}^y + iD_{\mathcal{Q}'_1}^y & E_{\mathcal{Q}'_1}^x - iD_{\mathcal{Q}'_1}^x & F_{\mathcal{Q}'_1}^z \end{pmatrix}$		9

symmetry. In this case, the dominant exchange interactions in the effective spin model in Eq. (10) are described by ones at $\{\mathbf{Q}\} = \{\pm\mathbf{Q}_1, \pm\mathbf{Q}_2, \pm\mathbf{Q}_3, \pm\mathbf{Q}'_1, \pm\mathbf{Q}'_2, \pm\mathbf{Q}'_3\}$ ($\{\mathbf{Q}\} = \{\pm\mathbf{Q}_1, \pm\mathbf{Q}_2, \pm\mathbf{Q}_3\}$ or $\{\pm\mathbf{Q}'_1, \pm\mathbf{Q}'_2, \pm\mathbf{Q}'_3\}$).

Tables IX–XI show the results of $X_{\mathbf{Q}_1}$ and $X_{\mathbf{Q}'_1}$ in the tetragonal, hexagonal, and trigonal crystal systems, respectively. In addition, the number of independent components (N_c) of the interaction matrix is shown. In all cases, $X_{\mathbf{Q}_1}$ has at least four independent components ($N_c \geq 4$). In the $P4/mmm$, $P422$, $P\bar{4}2m$, $P\bar{4}m2$, $P4mm$, $P6/mmm$, $P622$, $P\bar{6}m2$, $P\bar{6}2m$, $P6mm$, $P\bar{3}m1$, $P\bar{3}1m$, $P321$, $P312$, and $P3m1$ crystals, N_c of $X_{\mathbf{Q}'_1}$ is zero since the components of $X_{\mathbf{Q}'_1}$ are related to those of $X_{\mathbf{Q}_1}$. For example, nonzero components of $X_{\mathbf{Q}'_1}$ are obtained from those of $X_{\mathbf{Q}_1}$ by using the twofold rotation about the x axis, the mirror reflection on the xz plane, the time-reversal operation after the twofold rotation about the y axis, or the time-reversal operation after the mirror reflection on the yz plane depending on the space group. The other relevant interactions at the symmetry-related wave vectors in $\{\mathbf{Q}\}$ are obtained by using Eq. (11) in a similar way.

APPENDIX C: EFFECTIVE HAMILTONIAN OF THE ANISOTROPIC PERIODIC ANDERSON MODEL

We show the details of the low-energy effective model in Eq. (28) of the multiband anisotropic periodic Anderson model. The spin-dependent term, $\mathcal{H}'_{m\sigma;m'\sigma}$, is given by

$$\mathcal{H}'_{m\sigma;m'\sigma} = \sum_{\mathbf{k}, \mathbf{q}, \alpha} \tilde{\varepsilon}_{m\mathbf{k}+\mathbf{q}m'\mathbf{k}}^\alpha S_{\mathbf{q}}^\dagger c_{m\mathbf{k}+\mathbf{q}\sigma}^\dagger c_{m'\mathbf{k}\sigma} + \sum_{\mathbf{k}} \tilde{\varepsilon}_{mm'\mathbf{k}} c_{m\mathbf{k}\sigma}^\dagger c_{m'\mathbf{k}\sigma}, \quad (\text{C1})$$

where

$$\tilde{\varepsilon}_{m\mathbf{k}m'\mathbf{k}'}^\alpha = C_{m\mathbf{k}m'\mathbf{k}'}^{(1)} \left[V_{m'\mathbf{k}'}^\alpha V_{m\mathbf{k}}^{0*} + V_{m\mathbf{k}}^{\alpha*} V_{m'\mathbf{k}'}^0 \right. \\ \left. - i \sum_{\beta, \gamma} \epsilon_{\alpha\beta\gamma} V_{m'\mathbf{k}'}^\beta V_{m\mathbf{k}}^{\gamma*} \right], \quad (\text{C2})$$

$$\tilde{\varepsilon}_{mm'\mathbf{k}} = C_{mm'\mathbf{k}}^{(2)} (V_{m'\mathbf{k}}^0 V_{m\mathbf{k}}^{0*} + \mathbf{V}_{m'\mathbf{k}} \cdot \mathbf{V}_{m\mathbf{k}}^*), \quad (\text{C3})$$

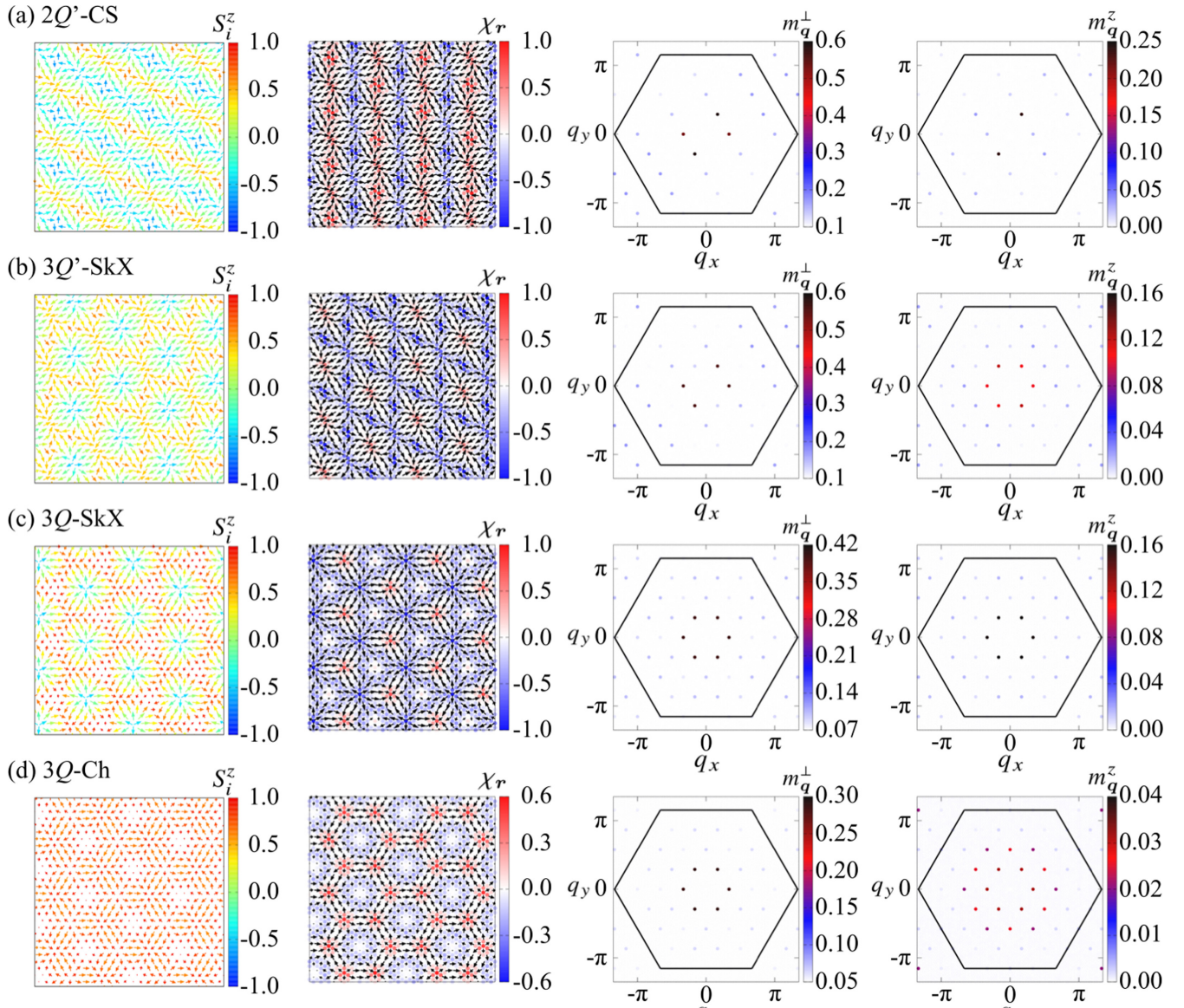


FIG. 15. First column: Snapshots of the spin configurations of (a) the $2Q'$ -CS state at $H = 0$, (b) the $3Q'$ -SkX state at $H = 0.3$, the (c) $3Q$ -SkX state at $H = 0.75$, and (d) the $3Q$ -Ch state at $H = 1.5$. The arrows and contours show the xy and z components of the spin, respectively. Second column: The scalar chirality configurations of the spin configurations shown in the first column. Third and fourth columns: The in-plane and out-of-plane magnetic moments in momentum space, respectively. The hexagons with a solid line show the first Brillouin zone. The $\mathbf{q} = \mathbf{0}$ component is removed for better visibility. The first and second columns in (b) and (c) are the same as Figs. 11(a) and 11(b), respectively.

with

$$C_{mkm'k'}^{(1)} = \frac{1}{2}(B_{mk} + B_{m'k'}), \quad (C4)$$

$$C_{mm'k}^{(2)} = -\frac{1}{2}\left(A_{mk} + \frac{B_{mk}}{2} + A_{m'k} + \frac{B_{m'k}}{2}\right). \quad (C5)$$

The first term with $m \neq m'$ ($m = m'$) in Eq. (C1) hybridizes different bands (the same band) at different wave vectors, while the second term with $m \neq m'$ ($m = m'$) hybridizes different bands (the same band) at the same wave vectors. However, these terms keep the degeneracy in terms of the itinerant electron spin σ , so they cannot be the origin of the anisotropic exchange interactions.

The spin-dependent terms, $\mathcal{H}_{m\sigma;m'\sigma'}^{\text{ex}}$ and $\mathcal{H}_{m\sigma;m'\sigma'}^{\text{SOC}}$, include the hybridization of the different bands, which are neglected in the main text, although they also become the origin of the anisotropic exchange interactions. When considering the hybridization, the expression of the anisotropic exchange interactions in Sec. III C becomes more complex. In the following, we show the details of the spin-dependent terms. The exchange interaction, $\mathcal{H}_{m\sigma;m'\sigma'}^{\text{ex}}$, is given by

$$\mathcal{H}_{m\sigma;m'\sigma'}^{\text{ex}} = \frac{1}{\sqrt{N}} \sum_{\mathbf{k}, \mathbf{q}, \alpha, \beta} J_{m\mathbf{k}+\mathbf{q}m'k}^{\alpha\beta} c_{m\mathbf{k}+\mathbf{q}\sigma}^{\dagger} \sigma_{\sigma\sigma'}^{\alpha} c_{m'k\sigma'} S_{\mathbf{q}}^{\beta}, \quad (C6)$$

where

$$J_{mkm'k'}^{\alpha\beta} = J_{mkm'k'}^{\text{ISO}} \delta_{\alpha\beta} + [J_{mkm'k'}^{\text{S}}]^{\alpha\beta} + [J_{mkm'k'}^{\text{AS}}]^{\alpha\beta} \quad (\text{C7})$$

with

$$J_{mkm'k'}^{\text{ISO}} = C_{mkm'k'}^{(1)} (V_{m'k'}^0 V_{mk}^{0*} - V_{m'k'} \cdot V_{mk}^*), \quad (\text{C8})$$

$$[J_{mkm'k'}^{\text{S}}]^{\alpha\beta} = C_{mkm'k'}^{(1)} (V_{m'k'}^\alpha V_{mk}^{\beta*} + V_{mk}^{\alpha*} V_{m'k'}^\beta), \quad (\text{C9})$$

$$[J_{mkm'k'}^{\text{AS}}]^{\alpha\beta} = C_{mkm'k'}^{(1)} i \sum_{\gamma} \epsilon_{\alpha\beta\gamma} (V_{m'k'}^\gamma V_{mk}^{0*} - V_{mk}^{\gamma*} V_{m'k'}^0). \quad (\text{C10})$$

The effective SOC, $\mathcal{H}_{m\sigma;m'\sigma'}^{\text{SOC}}$, is given by

$$\mathcal{H}_{m\sigma;m'\sigma'}^{\text{SOC}} = \sum_{\mathbf{k}} \mathbf{g}_{m\mathbf{k}} \cdot \mathbf{c}_{m\mathbf{k}\sigma}^\dagger \boldsymbol{\sigma}_{\sigma\sigma'} \mathbf{c}_{m'\mathbf{k}\sigma'}, \quad (\text{C11})$$

where

$$\mathbf{g}_{m\mathbf{k}}^\alpha = C_{m\mathbf{k}}^{(2)} \left[V_{m'k'}^\alpha V_{mk}^{0*} + V_{mk}^{\alpha*} V_{m'k'}^0 - i \sum_{\beta,\gamma} \epsilon_{\alpha\beta\gamma} V_{m'k'}^\beta V_{mk}^{\gamma*} \right]. \quad (\text{C12})$$

APPENDIX D: MAGNETIC PHASES IN THE CASE OF THE INTERACTIONS AT \mathbf{Q}_η

We show the details of the multiple- \mathbf{Q} states in the model with the interactions at $\{\mathbf{Q}\} = \{\pm\mathbf{Q}_1, \pm\mathbf{Q}_2, \pm\mathbf{Q}_3\}$ in Sec. V C 3. As shown in Fig. 10, we find the $2\mathbf{Q}'$ -CS state, $3\mathbf{Q}'$ -SkX, $3\mathbf{Q}$ -SkX, and the $3\mathbf{Q}$ -Ch state in addition to the $3\mathbf{Q}'$ -Ch-II state and the fully polarized state. Here, CS represents a chiral stripe characterized by a single peak of χ_q

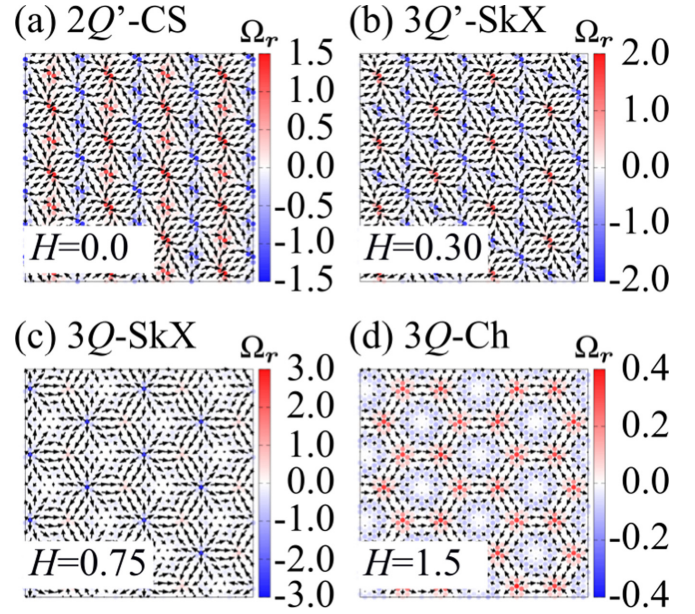


FIG. 16. Skyrmion density configurations of (a) the $2\mathbf{Q}'$ state at $H = 0$, (b) the $3\mathbf{Q}'$ -Ch-I state at $H = 0.1$, (c) the $3\mathbf{Q}'$ -Ch-I state at $H = 0.15$, and (d) the $3\mathbf{Q}'$ -Ch-II state at $H = 0.5$.

[75,156,157], and $3\mathbf{Q}$ stands for the same intensity of \mathbf{Q}_1 , \mathbf{Q}_2 , and \mathbf{Q}_3 components in the magnetic moments. Figure 15 shows the real-space spin and chirality configurations and the \mathbf{q} -space magnetic moments for the $2\mathbf{Q}'$ -CS state, the $3\mathbf{Q}'$ -SkX, the $3\mathbf{Q}$ -SkX, and the $3\mathbf{Q}$ -Ch state. Their skyrmion density configurations are shown in Fig. 16.

- [1] N. Nagaosa and Y. Tokura, Topological properties and dynamics of magnetic skyrmions, *Nat. Nanotechnol.* **8**, 899 (2013).
- [2] A. Fert, V. Cros, and J. Sampaio, Skyrmions on the track, *Nat. Nanotechnol.* **8**, 152 (2013).
- [3] X. Zhang, Y. Zhou, K. M. Song, T.-E. Park, J. Xia, M. Ezawa, X. Liu, W. Zhao, G. Zhao, and S. Woo, Skyrmion-electronics: writing, deleting, reading and processing magnetic skyrmions toward spintronic applications, *J. Phys.: Condens. Matter* **32**, 143001 (2020).
- [4] C. Psaroudaki and C. Panagopoulos, Skyrmion Qubits: A New Class of Quantum Logic Elements Based on Nanoscale Magnetization, *Phys. Rev. Lett.* **127**, 067201 (2021).
- [5] B. Göbel, I. Mertig, and O. A. Tretiakov, Beyond skyrmions: Review and perspectives of alternative magnetic quasiparticles, *Phys. Rep.* **895**, 1 (2021).
- [6] T. H. R. Skyrme, A unified field theory of mesons and baryons, *Nucl. Phys.* **31**, 556 (1962).
- [7] A. N. Bogdanov and D. A. Yablonskii, Thermodynamically stable “vortices” in magnetically ordered crystals: The mixed state of magnets, *Sov. Phys. JETP* **68**, 101 (1989).
- [8] A. Bogdanov and A. Hubert, Thermodynamically stable magnetic vortex states in magnetic crystals, *J. Magn. Magn. Mater.* **138**, 255 (1994).
- [9] U. K. Röbller, A. N. Bogdanov, and C. Pfleiderer, Spontaneous skyrmion ground states in magnetic metals, *Nature (London)* **442**, 797 (2006).
- [10] S. Mülbauer, B. Binz, F. Jonietz, C. Pfleiderer, A. Rosch, A. Neubauer, R. Georgii, and P. Böni, Skyrmion lattice in a chiral magnet, *Science* **323**, 915 (2009).
- [11] Y. Tokura and N. Kanazawa, Magnetic skyrmion materials, *Chem. Rev.* **121**, 2857 (2021).
- [12] Y. Tokunaga, X. Yu, J. White, H. M. Rønnow, D. Morikawa, Y. Taguchi, and Y. Tokura, A new class of chiral materials hosting magnetic skyrmions beyond room temperature, *Nat. Commun.* **6**, 7638 (2015).
- [13] I. Kézsmárki, S. Bordács, P. Milde, E. Neuber, L. M. Eng, J. S. White, H. M. Rønnow, C. D. Dewhurst, M. Mochizuki, K. Yanai, H. Nakamura, D. Ehlers, V. Tsurkan, and A. Loidl, Néel-type skyrmion lattice with confined orientation in the polar magnetic semiconductor GaV_4S_8 , *Nat. Mater.* **14**, 1116 (2015).
- [14] T. Kurumaji, T. Nakajima, M. Hirschberger, A. Kikkawa, Y. Yamasaki, H. Sagayama, H. Nakao, Y. Taguchi, T.-h. Arima, and Y. Tokura, Skyrmion lattice with a giant topological Hall effect in a frustrated triangular-lattice magnet, *Science* **365**, 914 (2019).
- [15] M. Hirschberger, T. Nakajima, S. Gao, L. Peng, A. Kikkawa, T. Kurumaji, M. Kriener, Y. Yamasaki, H. Sagayama, H. Nakao, K. Ohishi, K. Kakurai, Y. Taguchi, X. Yu, T.-h. Arima, and Y. Tokura, Skyrmion phase and competing magnetic orders on a breathing kagomé lattice, *Nat. Commun.* **10**, 5831 (2019).

- [16] A. K. Nayak, V. Kumar, T. Ma, P. Werner, E. Pippel, R. Sahoo, F. Damay, U. K. Rößler, C. Felser, and S. S. P. Parkin, Magnetic antiskyrmions above room temperature in tetragonal Heusler materials, *Nature (London)* **548**, 561 (2017).
- [17] T. Kurumaji, T. Nakajima, V. Ukleev, A. Feoktystov, T.-h. Arima, K. Kakurai, and Y. Tokura, Néel-Type Skyrmion Lattice in the Tetragonal Polar Magnet VOSe_2O_5 , *Phys. Rev. Lett.* **119**, 237201 (2017).
- [18] N. D. Khanh, T. Nakajima, X. Yu, S. Gao, K. Shibata, M. Hirschberger, Y. Yamasaki, H. Sagayama, H. Nakao, L. Peng, K. Nakajima, R. Takagi, T.-h. Arima, Y. Tokura, and S. Seki, Nanometric square skyrmion lattice in a centrosymmetric tetragonal magnet, *Nat. Nanotechnol.* **15**, 444 (2020).
- [19] K. Karube, L. Peng, J. Masell, X. Yu, F. Kagawa, Y. Tokura, and Y. Taguchi, Room-temperature antiskyrmions and sawtooth surface textures in a non-centrosymmetric magnet with S_4 symmetry, *Nat. Mater.* **20**, 335 (2021).
- [20] A. Neubauer, C. Pfleiderer, B. Binz, A. Rosch, R. Ritz, P. G. Niklowitz, and P. Böni, Topological Hall effect in the A phase of MnSi , *Phys. Rev. Lett.* **102**, 186602 (2009).
- [21] K. Hamamoto, M. Ezawa, and N. Nagaosa, Quantized topological Hall effect in skyrmion crystal, *Phys. Rev. B* **92**, 115417 (2015).
- [22] B. Göbel, A. Mook, J. Henk, and I. Mertig, Unconventional topological Hall effect in skyrmion crystals caused by the topology of the lattice, *Phys. Rev. B* **95**, 094413 (2017).
- [23] S. R. Saha, H. Sugawara, T. D. Matsuda, H. Sato, R. Mallik, and E. V. Sampathkumaran, Magnetic anisotropy, first-order-like metamagnetic transitions, and large negative magnetoresistance in single-crystal Gd_2PdSi_3 , *Phys. Rev. B* **60**, 12162 (1999).
- [24] M. Hirschberger, L. Spitz, T. Nomoto, T. Kurumaji, S. Gao, J. Masell, T. Nakajima, A. Kikkawa, Y. Yamasaki, H. Sagayama, H. Nakao, Y. Taguchi, R. Arita, T.-h. Arima, and Y. Tokura, Topological Nernst Effect of the Two-Dimensional Skyrmion Lattice, *Phys. Rev. Lett.* **125**, 076602 (2020).
- [25] Y. Shiomi, N. Kanazawa, K. Shibata, Y. Onose, and Y. Tokura, Topological Nernst effect in a three-dimensional skyrmion-lattice phase, *Phys. Rev. B* **88**, 064409 (2013).
- [26] N. Kanazawa, J. S. White, H. M. Rønnow, C. D. Dewhurst, D. Morikawa, K. Shibata, T. Arima, F. Kagawa, A. Tsukazaki, Y. Kozuka, M. Ichikawa, M. Kawasaki, and Y. Tokura, Topological spin-hedgehog crystals of a chiral magnet as engineered with magnetic anisotropy, *Phys. Rev. B* **96**, 220414(R) (2017).
- [27] Y. Fujishiro, N. Kanazawa, T. Nakajima, X. Z. Yu, K. Ohishi, Y. Kawamura, K. Kakurai, T. Arima, H. Mitamura, A. Miyake, K. Akiba, M. Tokunaga, A. Matsuo, K. Kindo, T. Koretsune, R. Arita, and Y. Tokura, Topological transitions among skyrmion- and hedgehog-lattice states in cubic chiral magnets, *Nat. Commun.* **10**, 1059 (2019).
- [28] S. Ishiwata, T. Nakajima, J.-H. Kim, D. S. Inosov, N. Kanazawa, J. S. White, J. L. Gavilano, R. Georgii, K. M. Seemann, G. Brandl, P. Manuel, D. D. Khalyavin, S. Seki, Y. Tokunaga, M. Kinoshita, Y. W. Long, Y. Kaneko, Y. Taguchi, T. Arima, B. Keimer *et al.*, Emergent topological spin structures in the centrosymmetric cubic perovskite SrFeO_3 , *Phys. Rev. B* **101**, 134406 (2020).
- [29] X. Z. Yu, Y. Tokunaga, Y. Kaneko, W. Zhang, K. Kimoto, Y. Matsui, Y. Taguchi, and Y. Tokura, Biskyrmion states and their current-driven motion in a layered manganite, *Nat. Commun.* **5**, 3198 (2014).
- [30] W. Wang, Y. Zhang, G. Xu, L. Peng, B. Ding, Y. Wang, Z. Hou, X. Zhang, X. Li, E. Liu, S. Wang, J. Cai, F. Wang, J. Li, F. Hu, G. Wu, B. Shen, and X.-X. Zhang, A centrosymmetric hexagonal magnet with superstable biskyrmion magnetic nanodomains in a wide temperature range of 100–340 K, *Adv. Mater.* **28**, 6887 (2016).
- [31] S. Zhang, F. Kronast, G. van der Laan, and T. Hesjedal, Real-space observation of skyrmionium in a ferromagnet-magnetic topological insulator heterostructure, *Nano Lett.* **18**, 1057 (2018).
- [32] S. Woo, K. M. Song, X. Zhang, Y. Zhou, M. Ezawa, X. Liu, S. Finizio, J. Raabe, N. J. Lee, S.-I. Kim, S.-Y. Park, Y. Kim, J.-Y. Kim, D. Lee, O. Lee, J. W. Choi, B.-C. Min, H. C. Koo, and J. Chang, Current-driven dynamics and inhibition of the skyrmion Hall effect of ferrimagnetic skyrmions in GdFeCo films, *Nat. Commun.* **9**, 959 (2018).
- [33] T. Dohi, S. DuttaGupta, S. Fukami, and H. Ohno, Formation and current-induced motion of synthetic antiferromagnetic skyrmion bubbles, *Nat. Commun.* **10**, 5153 (2019).
- [34] P. Bak and B. Lebech, Triple- q Modulated Magnetic Structure and Critical Behavior of Neodymium, *Phys. Rev. Lett.* **40**, 800 (1978).
- [35] S. M. Shapiro, E. Gurewitz, R. D. Parks, and L. C. Kupferberg, Multiple- q Magnetic Structure in CeAl_2 , *Phys. Rev. Lett.* **43**, 1748 (1979).
- [36] P. Bak and M. H. Jensen, Theory of helical magnetic structures and phase transitions in MnSi and FeGe , *J. Phys. C* **13**, L881 (1980).
- [37] E. M. Forgan, E. P. Gibbons, K. A. McEwen, and D. Fort, Observation of a Quadruple- q Magnetic Structure in Neodymium, *Phys. Rev. Lett.* **62**, 470 (1989).
- [38] C. D. Batista, S.-Z. Lin, S. Hayami, and Y. Kamiya, Frustration and chiral orderings in correlated electron systems, *Rep. Prog. Phys.* **79**, 084504 (2016).
- [39] S. Hayami and Y. Motome, Topological spin crystals by itinerant frustration, *J. Phys.: Condens. Matter* **33**, 443001 (2021).
- [40] B. Binz and A. Vishwanath, Theory of helical spin crystals: Phases, textures, and properties, *Phys. Rev. B* **74**, 214408 (2006).
- [41] J.-H. Park and J. H. Han, Zero-temperature phases for chiral magnets in three dimensions, *Phys. Rev. B* **83**, 184406 (2011).
- [42] S. Okumura, S. Hayami, Y. Kato, and Y. Motome, Magnetic hedgehog lattices in noncentrosymmetric metals, *Phys. Rev. B* **101**, 144416 (2020).
- [43] S. Grytsiuk, J.-P. Hanke, M. Hoffmann, J. Bouaziz, O. Gomonay, G. Bihlmayer, S. Lounis, Y. Mokrousov, and S. Blügel, Topological–chiral magnetic interactions driven by emergent orbital magnetism, *Nat. Commun.* **11**, 511 (2020).
- [44] K. Shimizu, S. Okumura, Y. Kato, and Y. Motome, Phase transitions between helices, vortices, and hedgehogs driven by spatial anisotropy in chiral magnets, *Phys. Rev. B* **103**, 054427 (2021).
- [45] K. Aoyama and H. Kawamura, Hedgehog-lattice spin texture in classical heisenberg antiferromagnets on the breathing pyrochlore lattice, *Phys. Rev. B* **103**, 014406 (2021).
- [46] Y. Kato, S. Hayami, and Y. Motome, Spin excitation spectra in helimagnetic states: Proper-screw, cycloid, vortex-crystal, and hedgehog lattices, *Phys. Rev. B* **104**, 224405 (2021).

- [47] S.-Z. Lin, A. Saxena, and C. D. Batista, Skyrmion fractionalization and merons in chiral magnets with easy-plane anisotropy, *Phys. Rev. B* **91**, 224407 (2015).
- [48] X. Z. Yu, W. Koshibae, Y. Tokunaga, K. Shibata, Y. Taguchi, N. Nagaosa, and Y. Tokura, Transformation between meron and skyrmion topological spin textures in a chiral magnet, *Nature (London)* **564**, 95 (2018).
- [49] S. Hayami and Y. Motome, Néel- and Bloch-Type Magnetic Vortices in Rashba Metals, *Phys. Rev. Lett.* **121**, 137202 (2018).
- [50] S. Bera and S. S. Mandal, Theory of the skyrmion, meron, antiskyrmion, and antimeron in chiral magnets, *Phys. Rev. Res.* **1**, 033109 (2019).
- [51] S. Hayami and Y. Motome, Square skyrmion crystal in centrosymmetric itinerant magnets, *Phys. Rev. B* **103**, 024439 (2021).
- [52] Z. Wang, Y. Su, S.-Z. Lin, and C. D. Batista, Meron, skyrmion, and vortex crystals in centrosymmetric tetragonal magnets, *Phys. Rev. B* **103**, 104408 (2021).
- [53] O. I. Utesov, Thermodynamically stable skyrmion lattice in a tetragonal frustrated antiferromagnet with dipolar interaction, *Phys. Rev. B* **103**, 064414 (2021).
- [54] S. Hayami and Y. Motome, Noncoplanar multiple- Q spin textures by itinerant frustration: Effects of single-ion anisotropy and bond-dependent anisotropy, *Phys. Rev. B* **103**, 054422 (2021).
- [55] S. Hayami and R. Yambe, Meron-antimeron crystals in non-centrosymmetric itinerant magnets on a triangular lattice, *Phys. Rev. B* **104**, 094425 (2021).
- [56] T. Momoi, K. Kubo, and K. Niki, Possible Chiral Phase Transition in Two-Dimensional Solid ^3He , *Phys. Rev. Lett.* **79**, 2081 (1997).
- [57] Y. Kamiya and C. D. Batista, Magnetic Vortex Crystals in Frustrated Mott Insulator, *Phys. Rev. X* **4**, 011023 (2014).
- [58] G. Marmorini and T. Momoi, Magnon condensation with finite degeneracy on the triangular lattice, *Phys. Rev. B* **89**, 134425 (2014).
- [59] Z. Wang, Y. Kamiya, A. H. Nevidomskyy, and C. D. Batista, Three-Dimensional Crystallization of Vortex Strings in Frustrated Quantum Magnets, *Phys. Rev. Lett.* **115**, 107201 (2015).
- [60] S. Hayami, S.-Z. Lin, Y. Kamiya, and C. D. Batista, Vortices, skyrmions, and chirality waves in frustrated mott insulators with a quenched periodic array of impurities, *Phys. Rev. B* **94**, 174420 (2016).
- [61] R. Yambe and S. Hayami, Skyrmion crystals in centrosymmetric itinerant magnets without horizontal mirror plane, *Sci. Rep.* **11**, 11184 (2021).
- [62] S. Hayami, T. Okubo, and Y. Motome, Phase shift in skyrmion crystals, *Nat. Commun.* **12**, 6927 (2021).
- [63] B. Göbel, A. Mook, J. Henk, and I. Mertig, Antiferromagnetic skyrmion crystals: Generation, topological Hall, and topological spin Hall effect, *Phys. Rev. B* **96**, 060406(R) (2017).
- [64] H. D. Rosales, D. C. Cabra, and P. Pujol, Three-sublattice skyrmion crystal in the antiferromagnetic triangular lattice, *Phys. Rev. B* **92**, 214439 (2015).
- [65] M. E. Villalba, F. A. Gómez Albarracín, H. D. Rosales, and D. C. Cabra, Field-induced pseudo-skyrmion phase in the antiferromagnetic Kagome lattice, *Phys. Rev. B* **100**, 245106 (2019).
- [66] T. Shimokawa, T. Okubo, and H. Kawamura, Multiple- q states of the $J_1 - J_2$ classical honeycomb-lattice Heisenberg antiferromagnet under a magnetic field, *Phys. Rev. B* **100**, 224404 (2019).
- [67] R. Yambe and S. Hayami, Ferrochiral, antiferrochiral, and ferri-chiral skyrmion crystals in an itinerant honeycomb magnet, *arXiv:2208.05115* (2022).
- [68] T. Garel and S. Doniach, Phase transitions with spontaneous modulation-the dipolar Ising ferromagnet, *Phys. Rev. B* **26**, 325 (1982).
- [69] O. I. Utesov, Mean-field description of skyrmion lattice in hexagonal frustrated antiferromagnets, *Phys. Rev. B* **105**, 054435 (2022).
- [70] T. Okubo, S. Chung, and H. Kawamura, Multiple- q States and the Skyrmion Lattice of the Triangular-Lattice Heisenberg Antiferromagnet under Magnetic Fields, *Phys. Rev. Lett.* **108**, 017206 (2012).
- [71] K. Mitsumoto and H. Kawamura, Replica symmetry breaking in the RKKY skyrmion-crystal system, *Phys. Rev. B* **104**, 184432 (2021).
- [72] K. Mitsumoto and H. Kawamura, Skyrmion crystal in the RKKY system on the two-dimensional triangular lattice, *Phys. Rev. B* **105**, 094427 (2022).
- [73] Y. Akagi, M. Udagawa, and Y. Motome, Hidden Multiple-Spin Interactions as an Origin of Spin Scalar Chiral Order in Frustrated Kondo Lattice Models, *Phys. Rev. Lett.* **108**, 096401 (2012).
- [74] S. Hayami and Y. Motome, Multiple- Q instability by $(d-2)$ -dimensional connections of Fermi surfaces, *Phys. Rev. B* **90**, 060402(R) (2014).
- [75] R. Ozawa, S. Hayami, K. Barros, G.-W. Chern, Y. Motome, and C. D. Batista, Vortex crystals with chiral stripes in itinerant magnets, *J. Phys. Soc. Jpn.* **85**, 103703 (2016).
- [76] R. Ozawa, S. Hayami, and Y. Motome, Zero-Field Skyrmions with a High Topological Number in Itinerant Magnets, *Phys. Rev. Lett.* **118**, 147205 (2017).
- [77] S. Hayami, R. Ozawa, and Y. Motome, Effective bilinear-biquadratic model for noncoplanar ordering in itinerant magnets, *Phys. Rev. B* **95**, 224424 (2017).
- [78] A. B. Butenko, A. A. Leonov, U. K. Rößler, and A. N. Bogdanov, Stabilization of skyrmion textures by uniaxial distortions in noncentrosymmetric cubic helimagnets, *Phys. Rev. B* **82**, 052403 (2010).
- [79] M. N. Wilson, A. B. Butenko, A. N. Bogdanov, and T. L. Monchesky, Chiral skyrmions in cubic helimagnet films: The role of uniaxial anisotropy, *Phys. Rev. B* **89**, 094411 (2014).
- [80] A. O. Leonov and M. Mostovoy, Multiply periodic states and isolated skyrmions in an anisotropic frustrated magnet, *Nat. Commun.* **6**, 8275 (2015).
- [81] S.-Z. Lin and S. Hayami, Ginzburg-Landau theory for skyrmions in inversion-symmetric magnets with competing interactions, *Phys. Rev. B* **93**, 064430 (2016).
- [82] S. Hayami, S.-Z. Lin, and C. D. Batista, Bubble and skyrmion crystals in frustrated magnets with easy-axis anisotropy, *Phys. Rev. B* **93**, 184413 (2016).
- [83] A. O. Leonov, T. L. Monchesky, N. Romming, A. Kubetzka, A. N. Bogdanov, and R. Wiesendanger, The properties of isolated chiral skyrmions in thin magnetic films, *New J. Phys.* **18**, 065003 (2016).

- [84] A. O. Leonov and I. Kézsmárki, Asymmetric isolated skyrmions in polar magnets with easy-plane anisotropy, *Phys. Rev. B* **96**, 014423 (2017).
- [85] S. Hayami and Y. Motome, Effect of magnetic anisotropy on skyrmions with a high topological number in itinerant magnets, *Phys. Rev. B* **99**, 094420 (2019).
- [86] S. Brinker, M. dos Santos Dias, and S. Lounis, The chiral biquadratic pair interaction, *New J. Phys.* **21**, 083015 (2019).
- [87] Z. Wang, Y. Su, S.-Z. Lin, and C. D. Batista, Skyrmion Crystal from RKKY Interaction Mediated by 2D Electron Gas, *Phys. Rev. Lett.* **124**, 207201 (2020).
- [88] D. S. Kathyat, A. Mukherjee, and S. Kumar, Microscopic magnetic Hamiltonian for exotic spin textures in metals, *Phys. Rev. B* **102**, 075106 (2020).
- [89] D. Amoroso, P. Barone, and S. Picozzi, Spontaneous skyrmionic lattice from anisotropic symmetric exchange in a Ni-halide monolayer, *Nat. Commun.* **11**, 5784 (2020).
- [90] I. Dzyaloshinsky, A thermodynamic theory of “weak” ferromagnetism of antiferromagnetics, *J. Phys. Chem. Solids* **4**, 241 (1958).
- [91] T. Moriya, Anisotropic superexchange interaction and weak ferromagnetism, *Phys. Rev.* **120**, 91 (1960).
- [92] S. Hayami and R. Yambe, Degeneracy lifting of Néel, Bloch, and anti-skyrmion crystals in centrosymmetric tetragonal systems, *J. Phys. Soc. Jpn.* **89**, 103702 (2020).
- [93] S. Hayami, Multiple skyrmion crystal phases by itinerant frustration in centrosymmetric tetragonal magnets, *J. Phys. Soc. Jpn.* **91**, 023705 (2022).
- [94] S. Hayami, Multiple- Q magnetism by anisotropic bilinear-biquadratic interactions in momentum space, *J. Magn. Magn. Mater.* **513**, 167181 (2020).
- [95] R. Takagi, J. White, S. Hayami, R. Arita, D. Honecker, H. Rønnow, Y. Tokura, and S. Seki, Multiple- q noncollinear magnetism in an itinerant hexagonal magnet, *Sci. Adv.* **4**, eaau3402 (2018).
- [96] M. Hirschberger, S. Hayami, and Y. Tokura, Nanometric skyrmion lattice from anisotropic exchange interactions in a centrosymmetric host, *New J. Phys.* **23**, 023039 (2021).
- [97] D. Amoroso, P. Barone, and S. Picozzi, Interplay between single-ion and two-ion anisotropies in frustrated 2D semiconductors and tuning of magnetic structures topology, *Nanomaterials* **11**, 1873 (2021).
- [98] E. F. Bertaut, Representation analysis of magnetic structures, *Acta Cryst. A* **24**, 217 (1968).
- [99] J. R. Schrieffer and P. A. Wolff, Relation between the Anderson and Kondo Hamiltonians, *Phys. Rev.* **149**, 491 (1966).
- [100] P. W. Anderson, Localized magnetic states in metals, *Phys. Rev.* **124**, 41 (1961).
- [101] K. Xia, W. Zhang, M. Lu, and H. Zhai, Noncollinear interlayer exchange coupling caused by interface spin-orbit interaction, *Phys. Rev. B* **55**, 12561 (1997).
- [102] Y. Yasui, C. J. Butler, N. D. Khanh, S. Hayami, T. Nomoto, T. Hanaguri, Y. Motome, R. Arita, T. h. Arima, Y. Tokura, and S. Seki, Imaging the coupling between itinerant electrons and localised moments in the centrosymmetric skyrmion magnet GdRu_2Si_2 , *Nat. Commun.* **11**, 5925 (2020).
- [103] N. D. Khanh, T. Nakajima, S. Hayami, S. Gao, Y. Yamasaki, H. Sagayama, H. Nakao, R. Takagi, Y. Motome, Y. Tokura, T. Arima, and S. Seki, Zoology of multiple- Q spin textures in a centrosymmetric tetragonal magnet with itinerant electrons, *Adv. Sci.* **9**, 2105452 (2022).
- [104] M. Kakihana, D. Aoki, A. Nakamura, F. Honda, M. Nakashima, Y. Amako, S. Nakamura, T. Sakakibara, M. Hedo, T. Nakama, and Y. Onuki, Giant Hall resistivity and magnetoresistance in cubic chiral antiferromagnet EuPtSi , *J. Phys. Soc. Jpn.* **87**, 023701 (2018).
- [105] K. Kaneko, M. D. Frontzek, M. Matsuda, A. Nakao, K. Munakata, T. Ohhara, M. Kakihana, Y. Haga, M. Hedo, T. Nakama, and Y. Onuki, Unique helical magnetic order and field-induced phase in trillium lattice antiferromagnet EuPtSi , *J. Phys. Soc. Jpn.* **88**, 013702 (2019).
- [106] M. Kakihana, D. Aoki, A. Nakamura, F. Honda, M. Nakashima, Y. Amako, T. Takeuchi, H. Harima, M. Hedo, T. Nakama, and Y. Onuki, Unique magnetic phases in the skyrmion lattice and Fermi surface properties in cubic chiral antiferromagnet EuPtSi , *J. Phys. Soc. Jpn.* **88**, 094705 (2019).
- [107] C. Tabata, T. Matsumura, H. Nakao, S. Michimura, M. Kakihana, T. Inami, K. Kaneko, M. Hedo, T. Nakama, and Y. Onuki, Magnetic field induced triple- q magnetic order in trillium lattice antiferromagnet EuPtSi studied by resonant x-ray scattering, *J. Phys. Soc. Jpn.* **88**, 093704 (2019).
- [108] S. Hayami and R. Yambe, Field-direction sensitive skyrmion crystals in cubic chiral systems: Implication to 4f-electron compound EuPtSi , *J. Phys. Soc. Jpn.* **90**, 073705 (2021).
- [109] T. Shang, Y. Xu, D. J. Gawryluk, J. Z. Ma, T. Shiroka, M. Shi, and E. Pomjakushina, Anomalous Hall resistivity and possible topological Hall effect in the EuAl_4 antiferromagnet, *Phys. Rev. B* **103**, L020405 (2021).
- [110] K. Kaneko, T. Kawasaki, A. Nakamura, K. Munakata, A. Nakao, T. Hanashima, R. Kiyonagi, T. Ohhara, M. Hedo, T. Nakama, and Y. Onuki, Charge-density-wave order and multiple magnetic transitions in divalent europium compound EuAl_4 , *J. Phys. Soc. Jpn.* **90**, 064704 (2021).
- [111] R. Takagi, N. Matsuyama, V. Ukleev, L. Yu, J. S. White, S. Francoual, J. R. Mardegan, S. Hayami, H. Saito, K. Kaneko *et al.*, Square and rhombic lattices of magnetic skyrmions in a centrosymmetric binary compound, *Nat. Commun.* **13**, 1472 (2022).
- [112] W. R. Meier, J. R. Torres, R. P. Hermann, J. Zhao, B. Lavina, B. C. Sales, and A. F. May, Thermodynamic insights into the intricate magnetic phase diagram of EuAl_4 , *Phys. Rev. B* **106**, 094421 (2022).
- [113] C. Bradley and A. Cracknell, *The Mathematical Theory of Symmetry in Solids: Representation Theory for Point Groups and Space Groups* (Oxford University Press, Oxford, 2009).
- [114] Y. Kato and Y. Motome, Magnetic field-temperature phase diagrams for multiple- q magnetic ordering: Exact steepest descent approach to long-range interacting spin systems, *Phys. Rev. B* **105**, 174413 (2022).
- [115] S. Gao, O. Zaharko, V. Tsurkan, Y. Su, J. S. White, G. S. Tucker, B. Roessli, F. Bourdarot, R. Sibille, D. Chernyshov, T. Fennell, A. Loidl, and C. Rüegg, Spiral spin-liquid and the emergence of a vortex-like state in MnSc_2S_4 , *Nat. Phys.* **13**, 157 (2017).
- [116] S. Gao, H. D. Rosales, F. A. G. Albarracín, V. Tsurkan, G. Kaur, T. Fennell, P. Steffens, M. Boehm, P. Čermák, A.

- Schneidewind, E. Ressouche, D. C. Cabra, C. Rüegg, and Z. Oksana, Fractional antiferromagnetic skyrmion lattice induced by anisotropic couplings, *Nature (London)* **586**, 37 (2020).
- [117] S. Hayami and R. Yambe, Locking of skyrmion cores on a centrosymmetric discrete lattice: Onsite versus offsite, *Phys. Rev. Res.* **3**, 043158 (2021).
- [118] K. Shimizu, S. Okumura, Y. Kato, and Y. Motome, Phase degree of freedom and topology in multiple- Q spin textures, *Phys. Rev. B* **105**, 224405 (2022).
- [119] S. Hayami and R. Yambe, Helicity locking of a square skyrmion crystal in a centrosymmetric lattice system without vertical mirror symmetry, *Phys. Rev. B* **105**, 104428 (2022).
- [120] S. Hayami and R. Yambe, Skyrmion crystal under D_{3h} point group: Role of out-of-plane Dzyaloshinskii-Moriya interaction, *Phys. Rev. B* **105**, 224423 (2022).
- [121] O. M. Sotnikov, V. V. Mazurenko, J. Colbois, F. Mila, M. I. Katsnelson, and E. A. Stepanov, Probing the topology of the quantum analog of a classical skyrmion, *Phys. Rev. B* **103**, L060404 (2021).
- [122] P. Siegl, E. Y. Vedmedenko, M. Stier, M. Thorwart, and T. Posske, Controlled creation of quantum skyrmions, *Phys. Rev. Res.* **4**, 023111 (2022).
- [123] A. Haller, S. Groenendijk, A. Habibi, A. Michels, and T. L. Schmidt, Quantum skyrmion lattices in Heisenberg ferromagnets, *arXiv:2112.12475* (2021).
- [124] B. Coqblin and J. R. Schrieffer, Exchange interaction in alloys with cerium impurities, *Phys. Rev.* **185**, 847 (1969).
- [125] R. Siemann and B. R. Cooper, Planar Coupling Mechanism Explaining Anomalous Magnetic Structures in Cerium and Actinide Intermetallics, *Phys. Rev. Lett.* **44**, 1015 (1980).
- [126] M. Zarea, S. E. Ulloa, and N. Sandler, Enhancement of the Kondo Effect through Rashba Spin-Orbit Interactions, *Phys. Rev. Lett.* **108**, 046601 (2012).
- [127] T. Shibusawa, H. Matsuura, and M. Ogata, Magnetic chirality induced from Ruderman-Kittel-Kasuya-Yosida interaction at an interface of a ferromagnet/heavy metal heterostructure, *J. Phys. Soc. Jpn.* **85**, 114701 (2016).
- [128] K. N. Okada, Y. Kato, and Y. Motome, Multiple- Q magnetic orders in Rashba-Dresselhaus metals, *Phys. Rev. B* **98**, 224406 (2018).
- [129] C. Zener, Interaction between the d -shells in the transition metals. II. ferromagnetic compounds of manganese with perovskite structure, *Phys. Rev.* **82**, 403 (1951).
- [130] P. W. Anderson and H. Hasegawa, Considerations on double exchange, *Phys. Rev.* **100**, 675 (1955).
- [131] P.-G. De Gennes, Effects of double exchange in magnetic crystals, *Phys. Rev.* **118**, 141 (1960).
- [132] K. Kubo and N. Ohata, A quantum theory of double exchange. I, *J. Phys. Soc. Jpn.* **33**, 21 (1972).
- [133] A. J. Millis, P. B. Littlewood, and B. I. Shraiman, Double Exchange Alone Does Not Explain the Resistivity of $\text{La}_{1-x}\text{Sr}_x\text{MnO}_3$, *Phys. Rev. Lett.* **74**, 5144 (1995).
- [134] H. Ishizuka and Y. Motome, Strong coupling theory for electron-mediated interactions in double-exchange models, *Phys. Rev. B* **92**, 024415 (2015).
- [135] S. Banerjee, O. Erten, and M. Randeria, Ferromagnetic exchange, spin-orbit coupling and spiral magnetism at the $\text{LaAlO}_3/\text{SrTiO}_3$ interface, *Nat. Phys.* **9**, 626 (2013).
- [136] S. Banerjee, J. Rowland, O. Erten, and M. Randeria, Enhanced Stability of Skyrmions in Two-Dimensional Chiral Magnets with Rashba Spin-Orbit Coupling, *Phys. Rev. X* **4**, 031045 (2014).
- [137] D. S. Kathyat, A. Mukherjee, and S. Kumar, Antiskyrmions and Bloch skyrmions in magnetic Dresselhaus metals, *Phys. Rev. B* **104**, 184434 (2021).
- [138] A. Mukherjee, D. S. Kathyat, and S. Kumar, Antiferromagnetic skyrmion crystals in the Rashba Hund's insulator on triangular lattice, *Sci. Rep.* **11**, 9566 (2021).
- [139] A. Mukherjee, D. S. Kathyat, and S. Kumar, Antiferromagnetic skyrmions and skyrmion density wave in a Rashba-coupled Hund insulator, *Phys. Rev. B* **103**, 134424 (2021).
- [140] W. S. Cole, S. Zhang, A. Paramekanti, and N. Trivedi, Bose-Hubbard Models with Synthetic Spin-Orbit Coupling: Mott Insulators, Spin Textures, and Superfluidity, *Phys. Rev. Lett.* **109**, 085302 (2012).
- [141] J. Chen, D.-W. Zhang, and J.-M. Liu, Exotic skyrmion crystals in chiral magnets with compass anisotropy, *Sci. Rep.* **6**, 29126 (2016).
- [142] S. Hayami, In-plane magnetic field-induced skyrmion crystal in frustrated magnets with easy-plane anisotropy, *Phys. Rev. B* **103**, 224418 (2021).
- [143] S. Hayami, Skyrmion crystal and spiral phases in centrosymmetric bilayer magnets with staggered Dzyaloshinskii-Moriya interaction, *Phys. Rev. B* **105**, 014408 (2022).
- [144] T. Kaplan, Single-band Hubbard model with spin-orbit coupling, *Z. Phys. B* **49**, 313 (1983).
- [145] L. Shekhtman, O. Entin-Wohlman, and A. Aharony, Moriya's Anisotropic Superexchange Interaction, Frustration, and Dzyaloshinskii's Weak Ferromagnetism, *Phys. Rev. Lett.* **69**, 836 (1992).
- [146] L. Shekhtman, A. Aharony, and O. Entin-Wohlman, Bond-dependent symmetric and antisymmetric superexchange interactions in La_2CuO_4 , *Phys. Rev. B* **47**, 174 (1993).
- [147] J. G. Rau, E. K.-H. Lee, and H.-Y. Kee, Generic Spin Model for the Honeycomb Iridates beyond the Kitaev Limit, *Phys. Rev. Lett.* **112**, 077204 (2014).
- [148] Y. Li, G. Chen, W. Tong, L. Pi, J. Liu, Z. Yang, X. Wang, and Q. Zhang, Rare-Earth Triangular Lattice Spin Liquid: A Single-Crystal Study of YbMgGaO_4 , *Phys. Rev. Lett.* **115**, 167203 (2015).
- [149] K. Essafi, O. Benton, and L. D. C. Jaubert, Generic nearest-neighbor kagome model: XYZ and Dzyaloshinskii-Moriya couplings with comparison to the pyrochlore-lattice case, *Phys. Rev. B* **96**, 205126 (2017).
- [150] P. A. Maksimov, Z. Zhu, S. R. White, and A. L. Chernyshev, Anisotropic-Exchange Magnets on a Triangular Lattice: Spin Waves, Accidental Degeneracies, and Dual Spin Liquids, *Phys. Rev. X* **9**, 021017 (2019).
- [151] T. Matsumoto and S. Hayami, Nonreciprocal magnons due to symmetric anisotropic exchange interaction in honeycomb antiferromagnets, *Phys. Rev. B* **101**, 224419 (2020).
- [152] T. Matsumoto and S. Hayami, Nonreciprocal magnon excitations by the Dzyaloshinskii-Moriya interaction on the basis of bond magnetic toroidal multipoles, *Phys. Rev. B* **104**, 134420 (2021).
- [153] S. Hayami and T. Matsumoto, Essential model parameters for nonreciprocal magnons in multisublattice systems, *Phys. Rev. B* **105**, 014404 (2022).

- [154] K. Takegahara, Y. Aoki, and A. Yanase, Slater-Koster tables for f electrons, *J. Phys. C* **13**, 583 (1980).
- [155] B. Berg and M. Lüscher, Definition and statistical distributions of a topological number in the lattice O(3) σ -model, *Nucl. Phys. B* **190**, 412 (1981).
- [156] D. Solenov, D. Mozyrsky, and I. Martin, Chirality Waves in Two-Dimensional Magnets, *Phys. Rev. Lett.* **108**, 096403 (2012).
- [157] R. Yambe and S. Hayami, Double- Q chiral stripe in the d - p model with strong spin-charge coupling, *J. Phys. Soc. Jpn.* **89**, 013702 (2020).